COMPREHENSIVE LOSS OPTIMIZATION OF INDUCTION MOTOR DRIVES

BY

SRIKANTHAN SRIDHARAN

DISSERTATION

Submitted in partial fulfillment of the requirements
for the degree of Doctor of Philosophy in Electrical and Computer Engineering
in the Graduate College of the
University of Illinois at Urbana-Champaign, 2015

Urbana, Illinois

Doctoral Committee:

Professor Philip T. Krein, Chair
Professor Andrew G. Alleyne
Associate Professor Kiruba S. Haran
Assistant Professor Robert Pilawa-Podgurski

ABSTRACT

Extensive use of power electronics-controlled induction motor drives over the past few decades has enabled the development of loss minimization control algorithms. With the technological advancements in power semiconductor switching devices such as insulated gate bipolar transistors and gate commutated thyristors, induction motor drives are increasingly used in applications, ranging from automotive traction to more-electric aircraft, which have widely varying speed, torque and power requirements. Advances in control technology have enabled the development of various sophisticated controllers for motor drives aimed at performance enhancement. Substantial energy savings may be obtained when drive controllers are optimized for loss reduction under varying operating conditions. This dissertation addresses loss optimization opportunities in induction motor drives from system perspectives.

First, a constrained loss optimization method is developed. Past work on loss minimization has focused on specific drive components such as the machine stator and rotor windings, inverter and dc-link. Component-level loss minimization, however, will not guarantee minimum total loss in the drive system. So, a system-level loss minimization method is proposed using a comprehensive loss model, to achieve true minimum total loss.

Next, a lossless damping controller is proposed to suppress undesirable resonant oscillations in the machine voltages and currents due to the use of LC filters between the inverter and motor terminals. Passive damping methods employing physical resistors to suppress

these oscillations, contribute to additional losses. Lossless active damping methods with virtual resistors have been explored in the literature. Conventionally, this resistance value is fixed, based on empirical rules, and left unchanged for all operating conditions. Choosing incorrect resistance values for the damping controller can result in degraded system behavior. A small-signal transfer function approach based on operating conditions and dynamic adjustment of the virtual resistance, is developed for the damping controller. The controller is designed to allow a flexible differential damping approach.

Finally, power electronics loss reduction is investigated in a voltage source inverter (VSI)-based induction motor drive. It is known that low drive speeds will result in poor bus utilization and increased power electronics loss for higher link voltages. Losses can be reduced by dynamically varying the dc link voltage according to operating conditions. In addition to reducing losses, varying the link voltage also reduces the switched voltage magnitude across the inverter switches, potentially increasing inverter reliability. In the proposed method, the link voltage is varied using a front-end dc-dc buck converter according to a loss minimization algorithm. The effect of additional loss from the front-end converter on the total loss is also studied. Benefits of the proposed methods are verified by simulations and experiments.

To all the Masters who have shown the Way

ACKNOWLEDGMENTS

Looking back at all the years after I arrived at the University of Illinois, I am only filled with gratitude for the rich experience here, that has enabled my growth in different ways. There are many people who deserve to be acknowledged for their contributions. First, I would like to express my sincere gratitude to my adviser, Prof. Philip Krein for his academic guidance and support over the years. His practical and insightful suggestions have enormously helped to form directions to this research. I am grateful for having had the opportunity to work closely with him. Thanks are also due to Prof. Andrew Alleyne, Prof. Kiruba Haran and Prof. Robert Pilawa for their constructive comments and suggestions that have helped to provide more clarity to some of the specific problems addressed in this research.

There are many people both within and outside the Power and Energy Systems group, who have directly or indirectly contributed in many ways. Though it would be unfair to name just a few, there are some bonds that have grown deeper than just professional acquaintances. Although it might sound exaggerated, I would never trade the camaraderie that I have shared with them. I extend my special appreciation to Sreeram and Ramsai who have always been a bedrock of support whenever I needed. Thanks are also due to Mayank, Sivatheja, Sasidhar, Raghavendra and Kalyan for the wonderful friendship. The weekly meetings of Vedanta Study Circle and the not-so-frequent meetings of SPIC-MACAY group have defined a major part of my social life in Illinois. Thanks to my groupmates Won, Tutku, Matt, Siming, Chris, Trevor and Andy, who have made this

academic journey an enjoyable one. I also extend my thanks to Digvijay, Sajal, Dipanjan and members of Team Pilawa, for all the sharings and learnings. Special thanks to the program assistant, Joyce for all the help extended to me on both my professional and personal fronts, ever since I started at Illinois and to Robin for all the administrative assistance. I also thank Jan Progen of the editorial office for the efforts spent in editing this dissertation.

This research would not have been possible without the generous support of the Grainger Center for Electric Machinery and Electromechanics and the Rolls-Royce Company. Many thanks to all the team members on the multi-physics Rolls-Royce project.

Before coming to Illinois, my foundational seeds were sown in the fun-filled years at IIT Madras, where my interests gradually matured towards power electronics and drives. I can always trace my roots there, even though the branches have spread far and wide. A mere acknowledgment of the education and wisdom received from the faculty and friends there, will be grossly insufficient. Heartfelt thanks to Prof. Mahesh Mishra and Prof. Krishna Vasudevan for the positive influence they had on me. Finally, words of thanks will be inadequate to acknowledge the support of my family, who have always stood by my academic and other pursuits with unrelenting faith and also for unconditionally allowing me to grow into my natural abilities.

TABLE OF CONTENTS

Chapter 1

INTRODUCTION

There is an increasing emphasis on global energy savings and efficiency targets for electric machines, owing to environmental concerns. Demanding performance requirements from automotive systems, more-electric aircraft and ships have necessitated improvements in electric drive design and control strategies. Government regulations have accelerated efforts in the automotive industry, to improve fuel economy and reduce greenhouse gas emissions with the adoption of aggressive standards, without compromising operational safety. For example, Toyota has calculated that its global fleet of hybrid vehicles has resulted in an estimated 41 million fewer tons of carbon-dioxide emissions than its gasoline-powered vehicles [1]. According to the International Energy Agency (IEA), end users currently pay about USD 565 billion per year for power consumed by electric motor driven systems (EMDS). Without any energy enhancement efforts, this is projected to increase to almost USD 900 billion by 2030 [2]. Emerging perspectives on system-oriented studies for loss minimization has furthered research to evaluate various losses, and propose technical and economic solutions.

Loss minimization methods for electric motor drives have been studied over the past three decades [3]. Research opportunities still exist in this area, given the increasing demand requirements from emerging applications and maturing power conversion topologies and architectures. Even a minor improvement in efficiency has been shown to result in significant global energy savings [4]. Many applications ranging from automobile traction to aircraft have widely varying speed and torque requirements. Inverter-fed drives have

motivated loss minimization studies to bring about significant energy savings. Improvements in materials and design have been proposed to improve static efficiency around rated conditions [5, 6]. Under widely varying operation, dynamic efficiency of the drive system is largely governed by control techniques [7]. Evolution of sophisticated vector control methods such as field oriented control (FOC) and direct torque control (DTC) have resulted in considerable performance improvements, compared to conventional scalar control methods such as the volts/hertz control. This chapter highlights motivations for this research and outlines the dissertation organization.

1.1 Automotive Power Systems

An electric vehicle (EV) is powered by an electric motor instead of an internal combustion engine (ICE). Batteries, which store energy to run the motor, must be charged periodically to replenish the depleted energy. A serious disadvantage is limited range, which implies a restricted travel distance per battery charge. Also, cold weather conditions can reduce the range to as low as 50%. A hybrid electric vehicle (HEV), like an EV, consists of an electric drivetrain and an ICE capable of periodically recharging the batteries. The engine is efficient only in a small range of operating speed and load [8]. The emissions are lowest at these operating conditions. Likewise, electric motors are most efficient around a specified rated operating condition. However, engine efficiency drops faster than motor efficiency at non-rated conditions. In the HEV, the engine can be made to operate at its best efficiency when recharging the batteries, and therefore reduce loss and emissions. A typical design target specification list, as derived from the U.S. Department of Energy's Partnership for a New Generation of Vehicles (PNGV) program, is shown in Table 1.1 [8]. Loss minimization goals are particularly relevant for extended travel range.

Table 1.1: Electric Machines and Power Electronics Design Targets [8]

	Units	Target
Electric Machines		
Peak specific power	kW/kg	1.6
Volumetric power density	kW/l	5.0
Specific cost	$/kW	4
Part load efficiency (@ 20% peak torque)	%	96
Power Electronics		
Peak specific power	kVA/kg	5
Volumetric power density	kW/l	12
Specific cost	$/kVA	7
Part load efficiency (@ 20% current)	%	97-98

1.2 Vehicle Drive Cycles

A drive cycle is a curve of vehicle speed versus time. It is typically used to quantitatively assess vehicle performance in terms of fuel consumption, emissions and predict performance of electric drives, engines, transmission systems, batteries, and other components in a drivetrain. Drive cycles are classified into *modal,* such as the New European Driving Cycle (NEDC) or Japanese 10-15 mode, and *transient*, such as the FTP-75 or Artermis cycles [9]. Modal cycles involve extended periods of constant speed and straight acceleration that are used for specialized tasks, whereas transient cycles generally involve rapid speed variations, similar to on-road, city driving conditions. The NEDC and Urban Artemis drive cycles are shown in Figure 1.1 to illustrate this difference. Torque requirements also vary with drive cycle speeds.

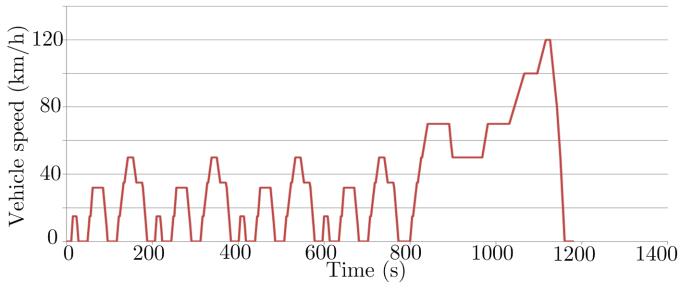

(a)

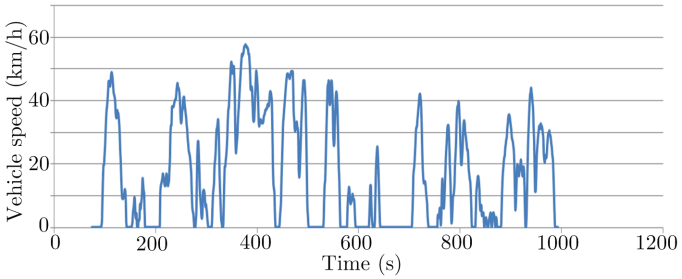

(b)

Figure 1.1: Example drive cycles (a) NEDC cycle (b) Urban Artemis cycle.

A drive cycle is programmed in a dynamometer to study fuel consumption and emissions from ICE-driven vehicles. Batteries are also monitored to calculate drive cycle efficiency. These data are subsequently used for energy calculations. Different countries have different standard driving cycles and benchmarks for testing purposes. As an example, the attributes of U.S., European, and Japanese drive cycles are given in Table 1.2 [10, 11]. The fundamental requirements of an EV motor control are to provide a high starting torque to enable reasonable acceleration, allow high-speed operation by flux-weakening and conserve battery energy [12]. Several EV prototypes operate with vector-controlled drives, both under field oriented control (FOC) and direct torque control (DTC). Their capabilities and limitations have been compared extensively in the literature [13, 14].

Table 1.2: Comparison of U.S., European, and Japanese Drive Cycles

	Time (s)	Avg. speed (m/h)	Max. speed (m/h)	Max. acc. (m/h/s)
Japanese JC08 test cycle	631	14.8	43.5	1.8
New European Driving Cycle (NEDC)	1181	20.9	74.6	2.4
U.S. EPA city cycle	1375	19.5	56.7	3.3
U.S. EPA highway cycle	766	48.2	59.9	3.3

1.3 Multiple-Stage Power Conversion

HEVs and EVs are conventionally equipped with a fixed, high-voltage battery-pack system to supply energy to the electric propulsion system [15]. An auxiliary battery is still used for the fixed 12 V system, which provides power to electric loads in the car, including the head and tail lights, audio systems, heating and cooling fans. This results in a dual-voltage battery system, where benefits can be obtained by transferring energy between the two systems. Dependence on a fixed, high-voltage battery pack results in severe constraints on both topology and architecture designs, and on energy management and control strategies [16, 17]. These limitations can be circumvented by using additional dc-dc converters to decouple the multiple voltage levels in the electrical system. Considering that the primary battery voltage is still at 12 V due to compatibility constraints in conventional vehicle architectures, the battery current demand is quite high, with peak current requirements around 300 A. Additional degrees of freedom obtained by introducing power converters give opportunities for design, control and energy management. An overview of component placement in an HEV is shown in Figure 1.2. A typical architecture of the HEV/EV electric system is shown in Figure 1.3. Since efficiency is also an important consideration, it is essential to address the impact of additional power converter stages on potential energy savings in the drive system. In this research, energy savings

and performance limitations are discussed for a dc-dc buck converter-based, variable link voltage scheme.

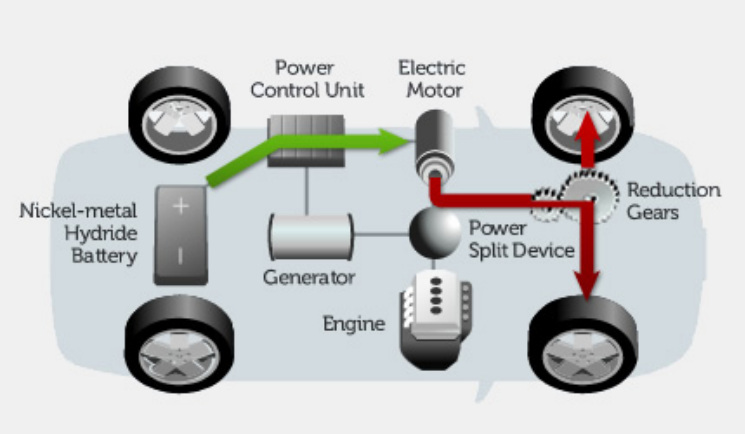

Figure 1.2: Schematic of component location inside a HEV [18].

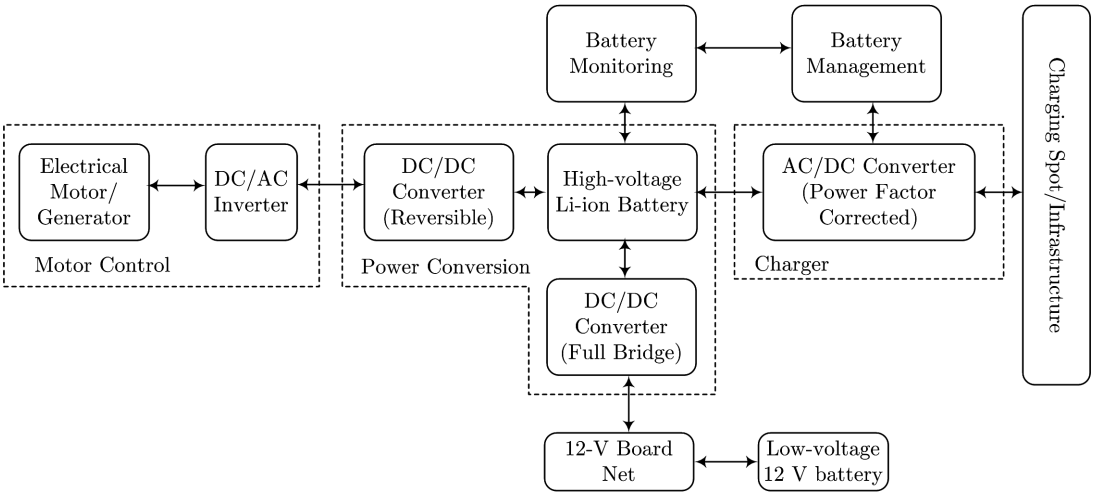

Figure 1.3: Power system architecture of HEV/EV [15].

A traction drive inverter design is based on the performance and efficiency needs of a specific drive cycle. Factors such as operating temperature, peak and continuous power, size, weight and cost determine the design parameters. Most inverters in the automotive applications have their maximum dc link voltages in the 600-1200 V range [19]. Typically the power conversion consists of two stages: The first consists of a boost converter which boosts the battery voltage to a required value. The second consists of the main power

inverter for the traction motor. For example, in the Toyota Prius® hybrid technology, the voltage-boosting converter increases the nominal 201.6 V battery voltage to a maximum of 650 V to feed the electric motors and the generator, as needed. The inverter can be made smaller and lighter. The power control unit (PCU) consists of another dc-dc converter to step down the 201.6 V battery supply voltage to 12 V for use in ancillary systems and other electronic devices [18]. Many architectures are possible with the use of dc-dc converters; some are shown in Figure 1.4 [16].

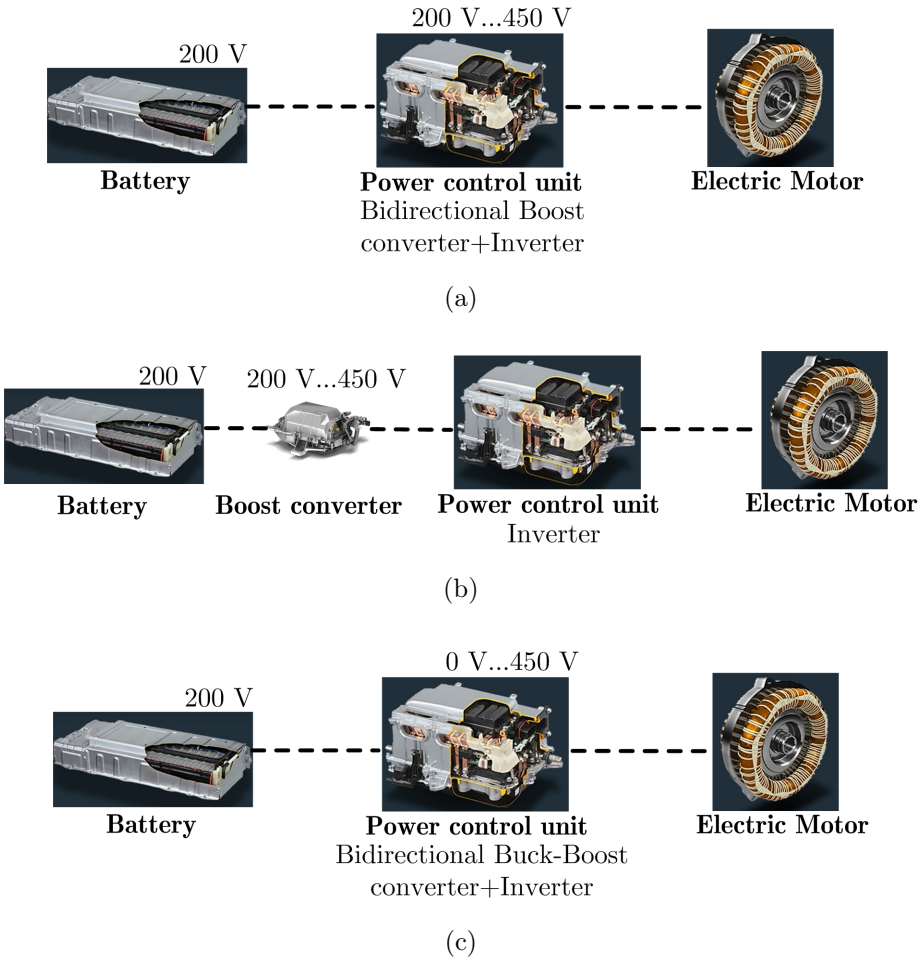

Figure 1.4: Various architectures for variable link voltage for the inverter using (a) Bidirectional boost converter (b) boost converter (c) bidirectional buck-boost converter.

1.4 Organization

This dissertation explores opportunities for loss optimization in induction motor drives over a wide range of operating conditions. A model-based and constrained drive loss optimization is developed to study loss reduction from a system perspective. Based on an optimization framework, possible degrees of freedom in the choice of the control variables, passive component values and dc-link voltage values are explored. Overall efficiency enhancement and performance trade-offs will be demonstrated on a rotor-flux oriented control (RFOC)-based induction motor drive. Considering the above scope, the following research objectives are accordingly proposed.

- Formulate an offline, comprehensive loss minimization approach to obtain near-minimum losses in the drive system including the machine copper and magnetic materials, inverter, filter, and the dc link. The total drive losses obtained from the proposed minimization will be compared with those of existing component-based optimization strategies.

- Develop a transfer-function based method for designing a dynamic active damping controller to suppress undesired resonant oscillations. The effect of damping resistance variation on steady-state and dynamic performance will also be studied.

- Implement a variable dc-link voltage scheme for the VSI using a front-end buck regulator between the fixed-voltage dc bus and the inverter. An algorithm to compute the dc-link voltage command will also be developed using the rotor flux and speed commands. The effect of additional loss from the front-end converter on the total loss will also be investigated for a wide range of operating conditions.

Chapter 2 presents a literature survey of various loss-minimizing strategies and their

classifications. Merits and drawbacks of these methods are discussed. Fundamentals of LC filter resonance in induction motor drives are then introduced. Conventional passive methods used for resonance damping and their limitations are highlighted to provide the motivation for active damping. Another opportunity for system loss reduction uses a variable link voltage scheme for the inverter. Advantages achieved with a front-end converter to provide variable voltage are discussed.

In Chapter 3, loss models of individual drive system components are derived. An objective function is formulated for a constrained, total loss optimization. Optimization results are compared with other component loss minimization methods. Drive operation regions which benefit the most from system loss optimization are discussed. A sample drive cycle is used to demonstrate energy savings.

Chapter 4 discusses the issue of undesirable resonant oscillations due to LC filters between the inverter and the induction machine. A lossless damping method to suppress these oscillations is discussed. A method based on a small-signal model of the machine-filter system is proposed for the selection of the damping resistance value in the controller. Instead of fixing the resistance value for all operating conditions, this value can be dynamically adjusted for different operating conditions.

Chapter 5 presents a variable dc-link voltage scheme to reduce power electronics losses in the inverter. An algorithm is presented to derive the minimum value constraint for the dc link voltage. Dynamic simulation and experimental results are presented to verify closed-loop operation of the front-end converter, in addition to the speed and flux regulation loops. Major contributions of this dissertation and possible future research topics and extensions are summarized in Chapter 6.

Chapter 2

LITERATURE SURVEY AND BACKGROUND INFORMATION

This chapter provides a literature review of various methods used for loss minimization in induction motor drives, from a system viewpoint. This will be followed by a brief discussion on resonance in LC circuits and its suppression by active damping in different applications. Finally, a few issues associated with the fixed, high voltage inverter dc link are outlined. The benefits of using a variable link voltage are emphasized. Energy savings data as a result of using the variable voltage scheme are highlighted.

2.1 Loss Minimization in Induction Machine Drive Systems

Motor drive applications, ranging from automotive traction to more-electric aircraft, have widely varying speed and torque demands. Significant research in inverter-fed motor drives has contributed to developing loss minimization schemes. These offer substantial operational energy savings, especially for wide operating conditions of speed and torque [20]. Although improvements in materials and design aspects have been proposed, these are usually targeted only at machine efficiency around rated conditions [5, 6]. However, with wide variations in operating conditions, the drive system running efficiency is primarily governed by loss-minimizing control techniques [7]. Such techniques are generally classified as search-based (online) and model-based (offline) methods [3]. The former require iterative measurements that search for the optimum control variable resulting in minimum loss [21]. In addition to convergence issues, iterative methods can exhibit undesirable speed and torque ripple. Genetic algorithms have also been used to evaluate

the optimum magnetization flux in online minimization [22]. With improved algorithms, the dependence of loss minimization on motor parameters can be reduced [23]. The latter methods depend on offline loss calculation from models and command the optimum control variable, usually from a look-up table [24]. This relatively fast and simple method requires accurate parameters. Many successful model-based implementations for loss minimization have been demonstrated [25–27]. Sections 2.1.1 and 2.1.2 present some of these methods.

2.1.1 Improvements in Construction Techniques and Materials

Evolving design and construction techniques using new materials have helped achieve efficiency targets set by IEEE (Institute of Electrical and Electronics Engineers) 841 and NEMA (National Electrical Manufacturers Association) standards. Ongoing research efforts are also focused on achieving efficiency levels beyond NEMA *Premium*. High-temperature superconducting (HTS) materials are showing promise for high power applications. Machine efficiency can be potentially increased by 1-2% by using die-cast copper rotors instead of aluminum rotors [28]. This study has also indicated that high-temperature nickel-based alloy dies will substantially increase die-life when die-casting copper [29]. A comparison of losses in a cast-copper rotor with those of a standard aluminum rotor as reported in [6] is presented in Table 2.1. The loss in copper rotor is seen to be reduced by half the loss in its aluminum counterpart.

A formal optimization procedure is described in [30] to determine the rotor slot design to maximize efficiency. Typical slot shapes may be trapezoidal, rectangular, round or double cage. The study in [30] presents the design optimization results to discover the best rotor slot shape by considering a generic slot shape, as shown in Figure 2.1. Although it is possible to include more details in the rotor slot shape by introducing more sections, this will increase the time required to achieve the optimized design. Results indicate that the slot geometry can vary markedly, depending on the application and performance

specifications. An optimization study, based on FEA (finite element analysis) in [31] is done for rectangular, stepped and step-holed shapes of rotor slots and bar cross-sections, assuming the same cross-sectional area. Results indicate that an increased starting torque and efficiency of copper squirrel-cage induction motors can be obtained using step-holed rotor bar cross-section, without significant decrease of breakdown torque.

Table 2.1: Loss Comparison in Aluminum and Copper Rotor Motors [6]

	Aluminum	Copper
Core loss	99 W	99 W
Stator winding loss	313 W	314 W
Rotor cage loss	110 W	60 W
Stray loss	12 W	8 W
Friction and windage	43 W	40 W
Motor efficiency	92.8 %	93.5 %

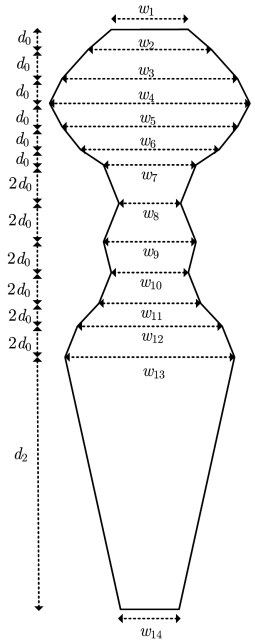

Figure 2.1: Generic rotor slot shape used for optimization in [30].

2.1.2 Improvements in Control Techniques

2.1.2.1 Machine Loss Minimization

A loss minimization method proposed in scalar-controlled motor drives uses stator current as the control variable. In the optimization control demonstrated for minimum machine loss in [7], only marginal improvements have been observed. A true minimum of machine losses was obtained in [24]. This minimization process takes a long time, but the authors claim it can be shortened by a trade-off with increased torque pulsations. Machine loss minimization is implemented in [26] by controlling the stator current and achieving a favorable balance between copper and iron losses. A closed-form expression for the optimum flux is developed in the flux-oriented frame. A further simplification of this approach using the approximate equivalent circuit is suggested in [32]. But this method ignores the leakage inductance in the circuit. In [27], rotor frequency is used as the control variable to achieve maximum machine efficiency. A slip frequency expression is derived in [33] to maximize machine efficiency and is

$$\omega_{slip-\eta_{max}} = \sqrt{\frac{R_r^2 R_s}{R_r L_m^2 + R_s L_r^2}} \tag{2.1}$$

It should be noted that (2.1) is an optimistic expression since it does not account for core losses. A generalized model for loss minimization in different motor types is developed in [34], which takes saturation effect into account. All these methods are largely aimed at machine loss reduction.

2.1.2.2 Torque Maximization

Maximum torque per ampere (MTPA) control can also be interpreted as minimization of stator current for a given torque. MTPA is developed in [33] by adjusting a control variable, such as the slip frequency, so that the stator current required to support a given load at a certain speed is minimized. Since the developed electromagnetic torque can be

given as $T_e = K_t i_{ds} i_{qs}$ for an FOC-based control, the torque function is maximized when i_{ds} is set equal to i_{qs}. Equivalently, the torque angle at this condition can be given as $\delta = 45°$, as seen from Figure 2.2. Here, K_t is a machine constant, and i_{ds} and i_{qs} refer to the d- and q-axes components of the stator current, respectively.

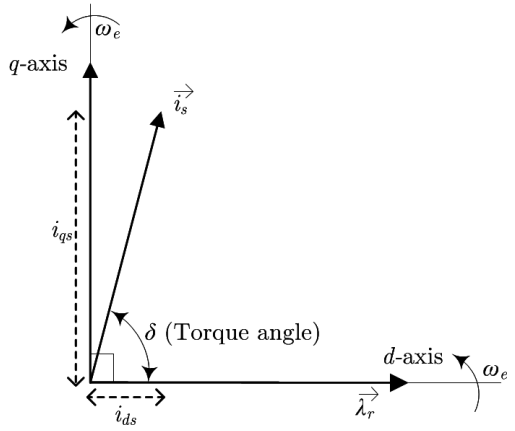

Figure 2.2: Stator current vector components in d-q coordinates.

An expression derived for the slip frequency which minimizes the stator current amplitude can be given as

$$\omega_{slip(MTPA)} = \frac{L_m R_r}{L_r \lambda_r} i_{qs} = \frac{L_m R_r}{L_r L_m i_{ds}} i_{qs} = \frac{1}{\tau_r} \tag{2.2}$$

where $\tau_r = \frac{L_r}{R_r}$ is the rotor time constant. This implies that to minimize stator current for a given torque, a constant slip equal to the inverse of the rotor time constant must be maintained. This approach has shown that the resulting motor efficiency is reasonably close to the optimal value and is insensitive to rotor resistance variation. At best, this approach can only minimize the stator current and hence, the stator copper losses. Maximum torque control can also be extended to the field-weakening region as discussed in [35]. In another approach, the torque angle can be controlled to improve power factor or efficiency [36]. In this scheme, the torque angle between the stator current and rotor flux is chosen based on the machine parameters and operation mode, such as MTPA,

maximum efficiency, or a combination of different indices. For the machine considered in [36], the torque angle result for maximum efficiency has been derived to be around 35°. Various correlations between torque angle control and MTPA, maximum efficiency and maximum power factor have also been analyzed in [36].

2.1.2.3 Inverter DC Link Current Minimization

Because of considerable dc link loss in CSI drives, techniques to minimize dc link current have been developed [37]. In a CSI drive, the dc choke used to provide a smooth and continuous current is typically sized in the range of 0.5-0.8 p.u. [38]. The importance of dc link loss reduction is highlighted in [39–41]. A lower dc link current rating can be obtained by using capacitor filters at the inverter output. This leads to lower conduction losses in the dc link and the switching devices [42]. CSI drives are increasingly used in many medium-voltage and high-power applications. In [37], the modulation control keeps the inverter modulation index at the maximum value. Though dc link current minimization was originally proposed for CSI drives, this can be applied to VSI drives using the duality principle [43]. A space vector map is used to explain the duality and establish the relationship between the switching states and patterns in both VSI and CSI, as shown in Section 2.2.

2.2 VSI-CSI Duality Principles

Inverters used in motor drives can be generally classified into VSI and CSI. The VSI outputs a defined PWM voltage waveform from a dc voltage input, whereas the CSI outputs a defined PWM current waveform from a dc current input. In practice, the dc current can be obtained from a CSR (current source rectifier) with a current feedback controller, as shown in Figure 2.3. The dc current is made continuous by using a dc choke at the output rectifier. The CSI usually requires capacitor filters at the output to provide a current path for energy stored in the phase inductances and prevent high-

voltage spikes [38]. Filters are used to output sinusoidal current and voltage waveforms. CSI also provides a reliable short-circuit protection capability by limiting the rate of current increase through the dc choke. The dynamic performance, however, is reduced because the dc current cannot be changed instantaneously during transients.

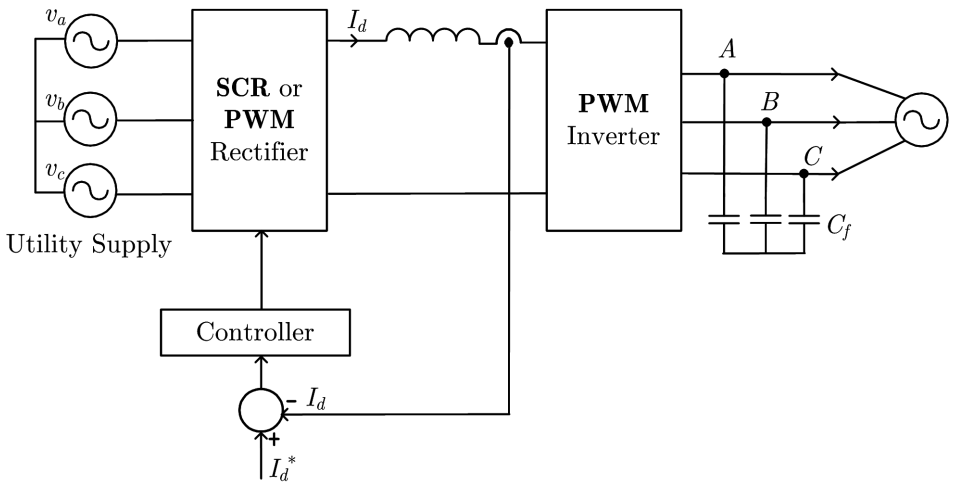

Figure 2.3: Realization of a dc current source from rectifier.

Ideal configurations of two-level VSI and CSI-based induction motor drives with filters are shown in Figures 2.4 and 2.5, respectively. VSI drives are the dominant topology for power conversion in the low power ranges, while CSI drives have advantages in specific applications. These include reduced electromagnetic interference and direct regeneration capabilities, in addition to inherent short-circuit protection. In contrast to a VSI fed by a constant dc voltage input, CSI drives have better dc bus utilization.

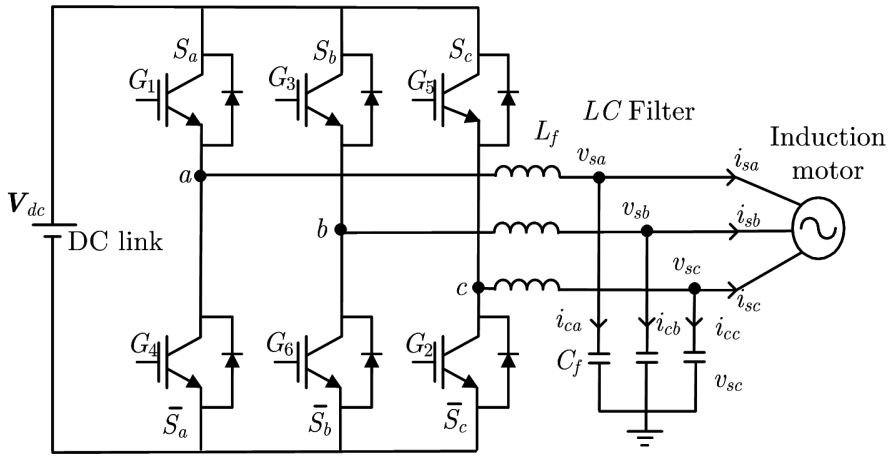

Figure 2.4: VSI-fed three-phase induction motor drive.

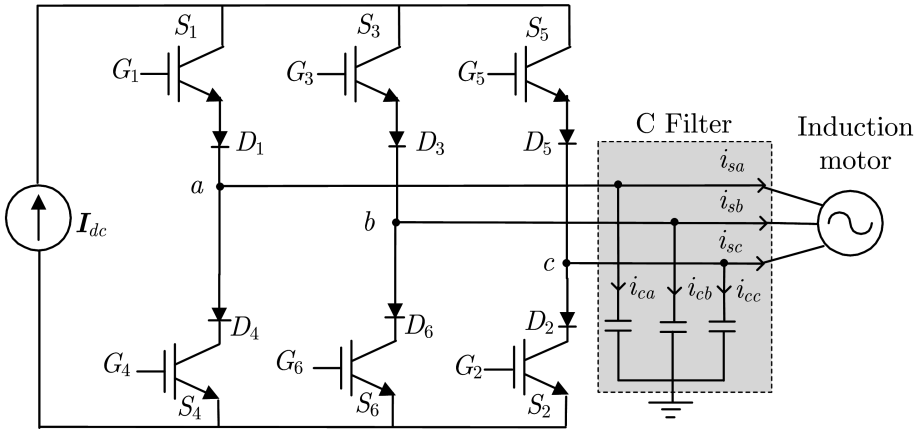

Figure 2.5: CSI-fed three-phase induction motor drive.

Modulation techniques for both VSI and CSI drives can be classified as *low-frequency* and *high-frequency* methods. Low-frequency methods include quasi-square PWM, trapezoidal PWM (TPWM) and selective harmonic elimination (SHE); high-frequency methods include sinusoidal PWM (SPWM) and space vector PWM (SVPWM). In general, high-frequency control techniques are more evolved for VSI than CSI [44]. With the development of high-power and self-commutated switching devices having adequate voltage and current handling capabilities, high-frequency control techniques are applicable to CSI. In fact, control techniques from VSI can be translated into equivalent CSI techniques and vice versa, based on duality [45, 46]. Because SVPWM is a widely used control in motor

drives, a space vector map can be used to explain this duality and establish the relationship between the switching states and patterns in both VSI and CSI [47]. Space vector diagrams of possible switching states in three-phase VSI and CSI are shown in Figures 2.6a and 2.6b respectively.

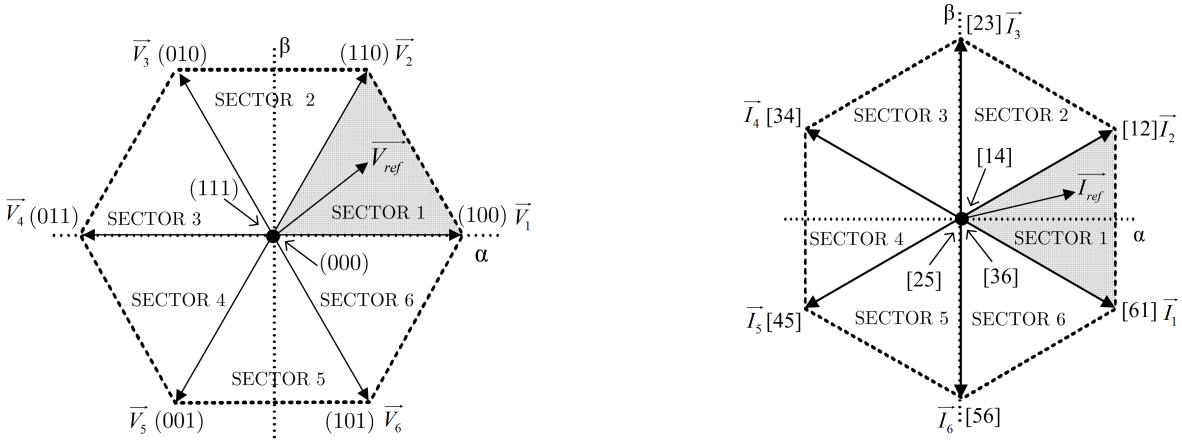

Figure 2.6: Space vector map of switching states in (a) VSI and (b) CSI.

Figure 2.7 shows the time domain modulating waveforms of space vector pulse width modulation (SVPWM) control. It is known that SVPWM is equivalent to SPWM with a third harmonic injection [48]. The corresponding frequency spectrums in Figure 2.8 indicate the relative harmonic performance between SVPWM control of VSI and CSI. Assuming identical phase references in Figure 2.6, space vector hexagons in VSI and CSI controls are out of phase by 30°. Any VSI-to-CSI PWM translation needs to account for this phase shift, which is critical for accurate vector control implementation in motor drives.

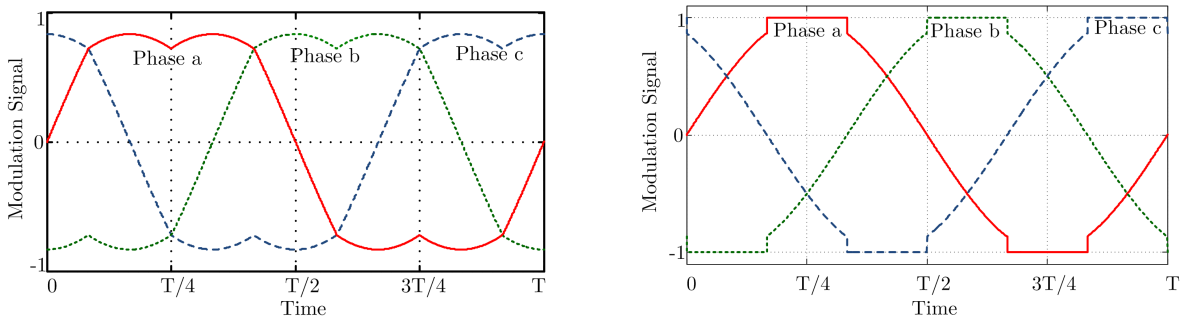

(a) (b)

Figure 2.7: Time domain modulation signals for (a) VSI (b) CSI.

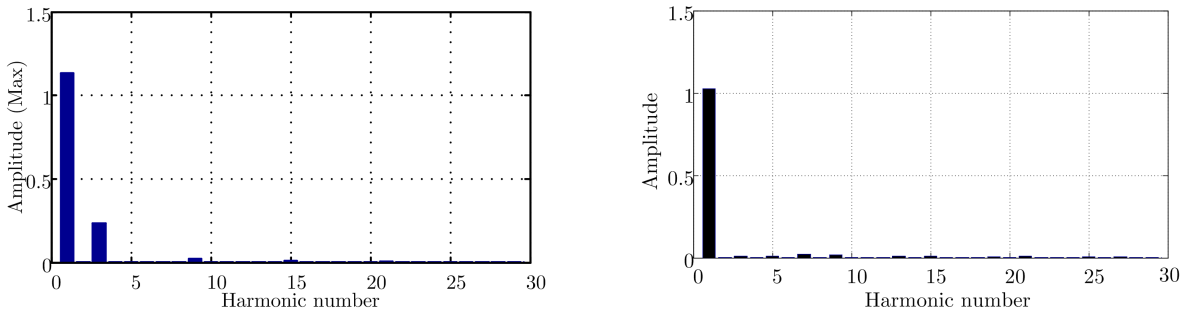

(a) (b)

Figure 2.8: Normalized Fourier spectrum for (a) VSI phase voltage (b) CSI phase current.

Simultaneous conduction of all three top or bottom switches of the VSI shown in Figure 2.4 constitute the zero states {(111), (000)}. VSI control must avoid switching overlap in the same inverter leg to prevent shoot through. Typically this condition is eliminated with dead time. CSI control should satisfy two conditions to make the PWM output current independent of load: A continuous path for dc input current must exist, and only two switches may conduct at any instant. Zero states {(000) , (111)} in the VSI map to zero states {(14) , (36) , (52)} in the CSI. CSI switches of the same leg conducting together lead to a bypass operation. Suitable CSI zero states can be selected to minimize the number of switch actions per sampling interval. For instance, use of vector (14) in Sector 1 of

the CSI space vector map implies that switch 1 conducts for the entire Sector I duration. This is inferred from the flat top in the modulation signal in Figure 2.7b. Any control must satisfy the corresponding switching constraints.

2.2.1 Space Vector Translation from VSI to CSI

The map of non-zero VSI states to non-zero CSI states is given in Table 2.2. Appropriate zero states are chosen to minimize the number of switching transitions between adjacent sectors. The conditions for inserting the desired zero states are given in Table 2.3. Boolean expressions to convert VSI to CSI states can be derived to obtain the combinational logic diagram shown in Figure 2.9. With this logic block, VSI switching signals can be used to trigger the CSI devices. The mapping can also be used for other modulation techniques including conventional sinusoidal, trapezoidal or SHE methods. Figure 2.10 shows an example of CSI phase current obtained by translated pulses from VSI.

Table 2.2: SVPWM Control: Translation of Non-Zero States

Non-Zero VSI states			Non-Zero CSI states					
S_a	S_b	S_c	S_1	S_2	S_3	S_4	S_5	S_6
0	0	1	0	0	0	1	1	0
0	1	0	0	1	1	0	0	0
0	1	1	0	0	1	1	0	0
1	0	0	1	0	0	0	0	1
1	0	1	0	0	0	0	1	1
1	1	0	1	1	0	0	0	0

Table 2.3: SVPWM Control: Translation of Zero States

Position of CSI vector	Required CSI zero state
Sector I or IV	(14)
Sector II or V	(25)
Sector III or VI	(36)

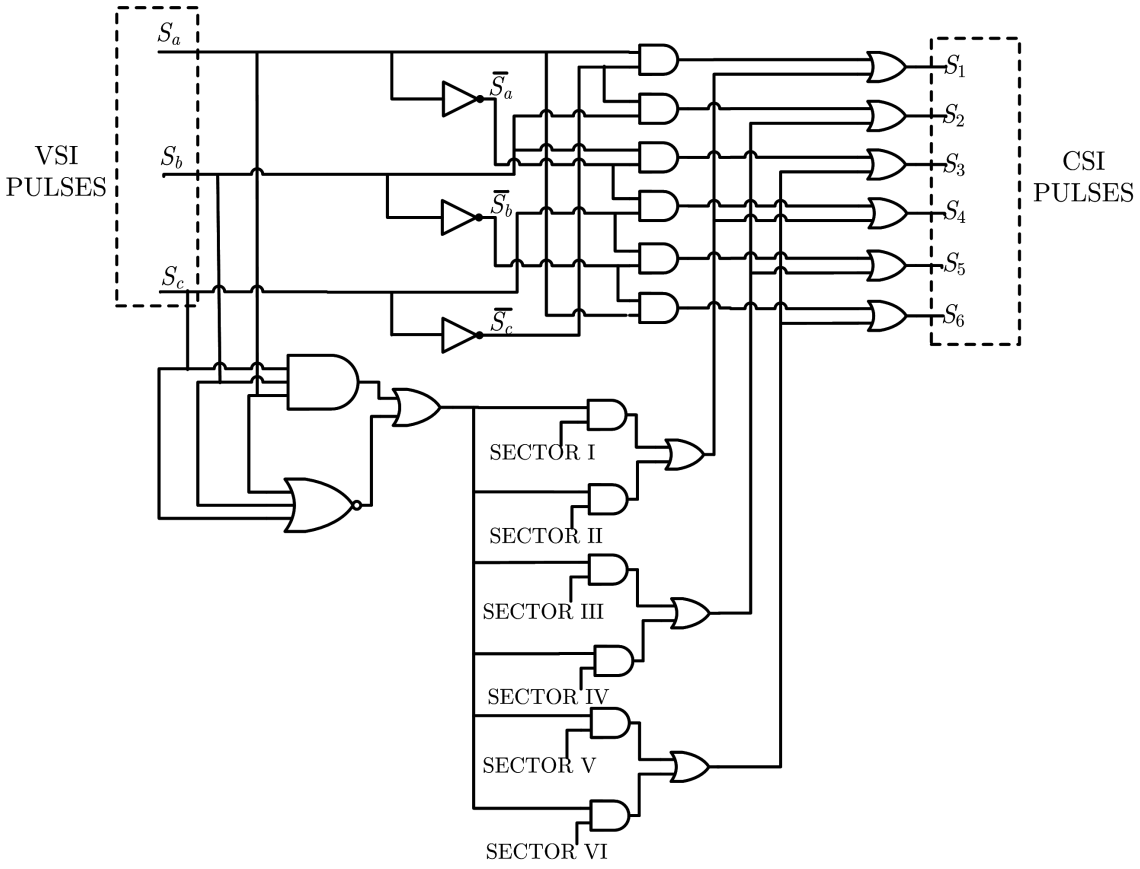

Figure 2.9: Logic gate realization to translate switching pulses from VSI to CSI.

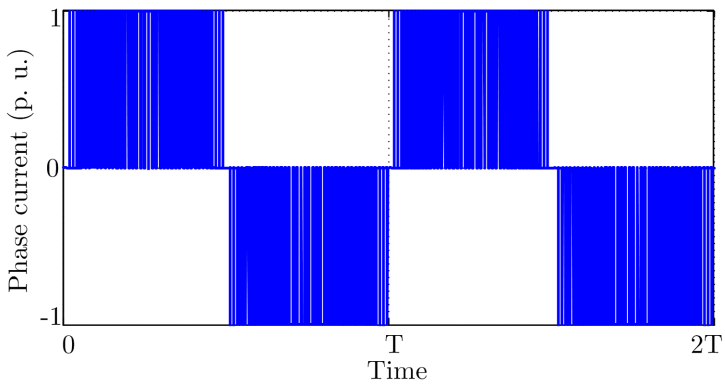

Figure 2.10: CSI phase current using translated VSI-SVPWM.

2.3 LC Resonance Suppression

2.3.1 Resonance in Series-Parallel Circuits

The induction motor-filter system is a combination of series and parallel resistive, inductive and capacitive elements. Adding resistance to such networks will alter the effective resonant frequency. For example, ESR or core losses in the inductors can shift the resonant peaks. This is illustrated in the following example. In the circuit shown in Figure 2.11a, the following values are assumed for the passive components: $L = 10$ mH, $C = 10$ μF, $R_L = 100\ \Omega$, $R_c = 10\ \Omega$. If the resistances are ignored, the resonant frequency can be easily computed as $\omega_{res} = \frac{1}{\sqrt{(10\times10^{-3}\times10\times10^{-6})}} = 3162$ rad/s. With the inclusion of R_L and R_C, the resonant frequency is shifted down to 3080 rad/s, as seen from Figure 2.11b. In an induction motor, the resistances are inherent in stator, rotor and core-loss elements of the equivalent circuit. This resonant frequency shift depends on the resistance location in the network, as summarized in Table 2.4.

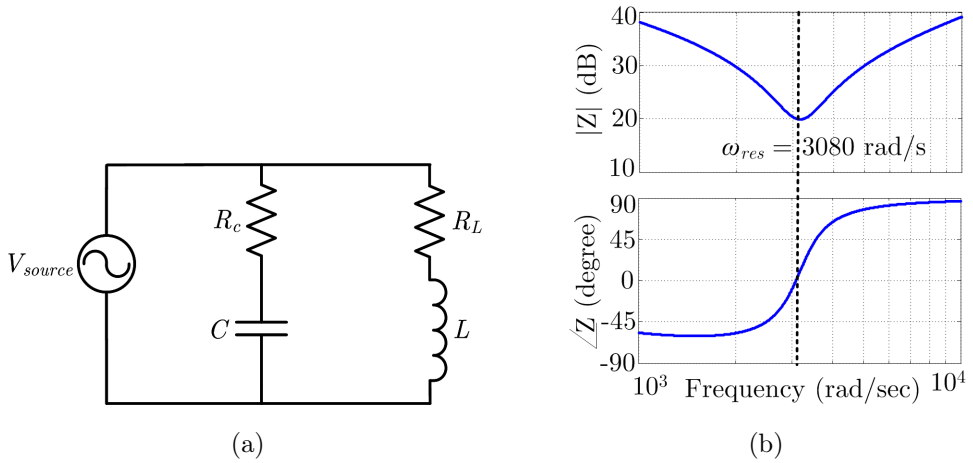

Figure 2.11: (a) Parallel LC circuit (b) Impedance magnitude and phase plot of the resonant circuit in (a).

Table 2.4: Effect of Resistance Location on Resonant Frequency

Parallel LC circuit	R in series with L	$\omega_{res} \downarrow$
	R in series with C	$\omega_{res} \uparrow$
Series LC circuit	R in parallel with L	$\omega_{res} \uparrow$
	R in parallel with C	$\omega_{res} \downarrow$

2.3.2 Damping Techniques

Inverter-fed ac drive systems impose high dv/dt or di/dt values and rapidly varying PWM switching signals on machines. These cause high bearing currents and shaft heating; they may produce sparks. Long cables between the inverter and motor can lead to voltage reflections causing increased voltages at the motor terminals [49, 50]. This can lead to further electromagnetic interference issues which cause improper operation of sensitive loads, harmonic distortion and stator insulation deterioration. LC filters have been used to mitigate these issues [51]. However, adding LC filters adds oscillatory modes. Reference

[52] discusses the electrical instability of an induction motor driven by CSI with output capacitors. Harmonic components in the inverter output close to the resonant mode of the motor-filter combination will result in undesirable oscillations in the motor terminal voltages and currents [53]. These oscillations will produce heavy pulsations in torque output. This can lead to prohibitive vibration and acoustic noise in motors [54, 55]. They can also damage switching devices in the inverter circuit. Since the motor winding resistances are generally designed to be low to achieve efficiency targets, they cannot provide damping sufficient to suppress resonance.

Traditional passive damping techniques use a physical resistor to damp these oscillations at the cost of additional losses [56, 57]. Active lossless damping techniques using virtual resistors have been widely explored to suppress these oscillations [55, 56, 58, 59]. Various approaches involving single-loop and multi-loop controllers have been proposed, both in stationary and synchronous reference frames [60, 61]. Most of these controllers operate by setting suitable gains in the control loop to achieve a specific damping ratio at all operating conditions [55, 58]. For open-loop operation, a damping controller based on power compensation is proposed in [59].

Active damping methods have also been reported for grid-connected applications [62]. An implementation is shown for active damping in a dc link capacitor, which forms a part of the rectifier circuit connected to the grid, as shown in Figure 2.12. Low dc link capacitance tends to act like negative impedance at high-power operating points with low input-line resistance and high line inductance [63]. This method seeks to reduce total harmonic distortion in the input line current. Feedback linearization is used to stabilize constant power loads in [8]. This method relies on a nonlinear feedback of all state variables including line current and dc link voltage, and requires a complex implementation. In [64], a high virtual capacitance is added to the the load to ensure stable operation and transient control of the dc link capacitor.

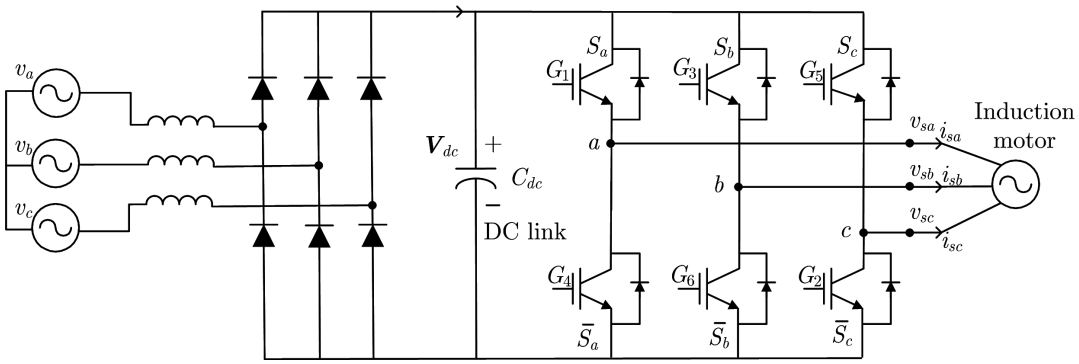

Figure 2.12: Active damping for dc link rectifier.

With increasing penetration of renewable energy resources into the power grid, stringent regulations are imposed on power quality. Reducing harmonics is essential for high-performance grid-connected PWM rectifiers to fulfill standards such as IEEE 519-1992, IEC 61000-3-2 and IEC 61000-3-4. Instead of a large input inductance, which inhibits rectifier dynamic performance, an LCL filter is usually added, as shown in Figure 2.13. Low inductances are used with the capacitor to provide current ripple attenuation [28]. Series virtual resistance is used in this active damping solution. The virtual voltage drops of the oscillating capacitor voltages are subtracted from the voltage references for the VSI. The dual of this method involves generating virtual damping currents by emulating parallel resistance across the resistor. These currents are subtracted from the VSI current references.

The virtual damping method can also be treated as feedback compensation. In [65], a lead-lag compensator in the synchronous reference frame applied to the capacitor voltage feedback is demonstrated. Here, the active damping loop is speed-dependent and required to be the fastest loop in the control system. The current-control loop bandwidth has been enhanced by processing the control algorithm within half of the carrier period and updating PWM output twice per carrier period. A feedforward control for the LC filter is suggested in [66] to improve the deteriorated performance due to the additional filter. Since this method is used in a three-level inverter, the filtering requirements are lower.

This allows a smaller filter than that required of a two-level inverter.

An adaptive full-order observer using cascaded control loops is used in [67] for estimating the system states to implement the FOC method in VSI drives with LC filters. Active damping has also been implemented on a DTC platform for a three-level, neutral-point-clamped (NPC), VSI drive with LC filters [68]. In this implementation, the inverter is supposed to deliver only the active power, and the capacitor in the LC filter provides the reactive power required by the induction motor. The regulation loop needed to damp the filter oscillations adds the correction terms to the torque and flux set values. An additional regulation to modulate the hysteresis bandwidth in the controller acts on both the torque and flux loops to increase or decrease the switching frequency. The method demonstrated in [69] requires the resonant frequency information of the machine-filter combination. However, it is claimed that small changes in the resonant frequency caused due to the variation of leakage inductance will not affect the control action. A phase-advancement technique is also introduced into the controller to compensate for the delay introduced by the inverter. In [55], the dynamic performance degradation due to using a filter in the virtual damping loop is highlighted. Here, a control-signal shaping technique has been shown to improve the damping performance.

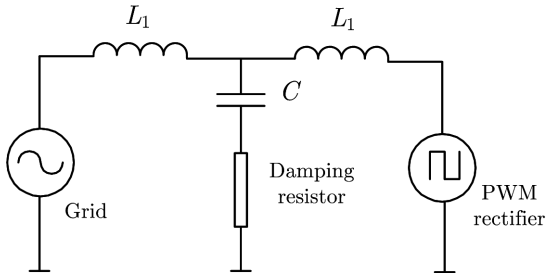

Figure 2.13: Single-phase equivalent of a three-phase PWM rectifier connected to the grid with LCL filters.

2.4 Inverter Link Voltage Optimization

Most VSI-based induction motor drives operate from a fixed, high-voltage dc bus. However, at low drive speeds, use of a high dc link voltage will result in a low modulation index for the inverter, leading to poor bus utilization. Hysteresis-based current controllers have been widely used in motor-drive applications for their fast dynamic response and inherent peak-current limiting capability. Such controllers, however, will lead to increased switching losses with higher link voltages [70–72]. The inverter semiconductor switches are also subject to increased voltage stress, potentially leading to reliability deterioration. High-voltage slew rates and high common-mode voltages can cause premature winding failures, ground leakage currents, shaft voltages, bearing currents and conducted or radiated electromagnetic interference. These can have a number of detrimental effects as outlined below [8].

- Increased overlap of voltage and current waveforms in the switch during turn-on and turn-off intervals increases the switching losses in the device.
- With prolonged hard switching operation, the reliability of the switch can deteriorate due to the stress caused.
- High dv/dt or di/dt rates and parasitic effects can create EMI issues that can impact the normal operation of circuits nearby. Large displacement currents can damage machine insulation over a period of time.
- Common-mode dv/dt across the stator winding creates a circulating current to ground through the machine shaft and stray capacitance of the insulated bearing, causing them to wear out quickly.
- High dv/dt at the inverter outputs tends to boost the motor terminal voltage by

reflection of high-frequency traveling waves. Excessive voltage can cause breakdown of machine insulation.

The above effects can be mitigated by using a variable voltage for the inverter dc link. The variable voltage is obtained by using a front-end, dc-dc converter between a fixed-voltage dc bus and the inverter. Prior work has discussed the use of variable dc link voltage schemes toward better drive performance. A variable dc link voltage scheme discussed in [73] is aimed at improving the resolution in the low-output voltage command of an SVPWM-based sensorless induction motor drive in the low-speed range.

A self-controlled drive with variable dc link and fixed-frequency PWM is proposed in [74] to provide better harmonic performance at low frequencies. The variable dc link discussed in [75] provides improved accuracy for sensorless induction motor drive in the motor's low-speed range. In electric vehicles that are powered by battery, an additional dc-dc converter added between the battery and the VSI provides the following useful features [76].

- Using a boost conversion stage, high voltage motors can be powered from batteries with lower output voltages.
- Stacking of a large number of series-connected cells can be avoided or reduced.
- Converter voltage output can be dynamically changed based on the drive operating conditions to enable loss reduction in the drive system.
- Optimal operating conditions of the battery can be maintained through appropriate converter control.

The energy recovered from the regenerative braking process increases overall efficiency and potentially increases the automobile's range. The adjustable link voltage in [76] is demonstrated on an interior permanent magnet synchronous machine (IPMSM). The optimal dc bus voltage derived is maintained constant throughout the drive cycle. Optimal voltages and percentage energy savings corresponding to different drive cycles including Highway Fuel Economy Driving Schedule (HWFET), New York City Cycle (NYCC) and New European Driving Cycle (NEDC), as claimed in [76] are given in Table 2.5. A graph of optimal line-to-line voltage of the IPMSM for a system without dc-dc converter is shown in Figure 2.14, for a battery voltage of 400 V. At high motor speeds, the dc bus voltage limit is reached.

A maximum efficiency operating strategy is developed for an IPMSM in [77]. The dependence of switching loss on the link voltage is included in the objective function formulated for maximum efficiency. Optimal stator currents are obtained by a search algorithm. It is shown that the use of a maximum efficiency method increases the drive efficiency by 0.3 % in comparison to the MTPA method for similar loading conditions. The total energy saving potential depends on the distribution of operating points in a given drive cycle. As more operating points occur in the low-speed range, more energy savings are possible.

Apart from optimal voltage methods, optimal modulation methods have also been developed to reduce converter system losses, by producing an optimized pulse pattern [78]. Additional losses arise due to harmonics associated with PWM switching in VSI. An improved high-frequency loss model making use of experimental coefficients is proposed in [79]. The harmonic loss models are based on the frequency dependence of motor resistances and inductances due to skin effects. Using the measured loss points, a curve-fit is performed using the following expression for motor losses.

$$P_{loss} = K_{cu} \sum_{f} \frac{V_f^2}{f^{1.5}} + K_{fe} \sum_{f} \frac{V_f^2}{f^d} \tag{2.3}$$

where K_{cu}, K_{fe} and exponent d are required to be evaluated. Equation (2.3) implies that wide variations in switching frequencies will result in a widely distributed loss spectrum. Although the equation suggests higher PWM frequencies for reduced losses, the increase in switching loss can eventually exceed the reduction in motor loss.

Table 2.5: Energy Savings for Drive Cycles [76]

	HWFET	NYCC	NEDC
Optimal dc bus voltage (V)	250	100	125
Energy demand without dc-dc converter (kWh/100 km)	15.88	32.07	16.23
Energy demand with dc-dc converter (kWh/100 km)	15.17	18.19	14.05

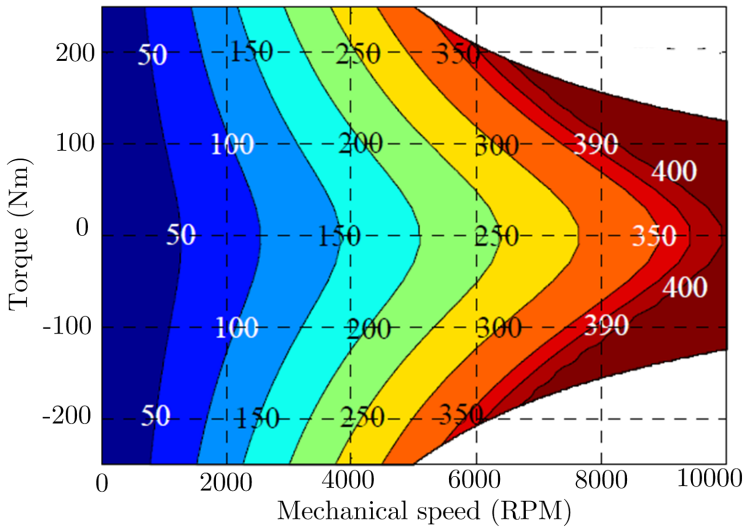

Figure 2.14: Optimal line-line voltage of the IPMSM without dc-dc converter at a battery voltage of 400 V, as reported in [76].

The influence of dc link voltage on the efficiency and operating limits of an IPMSM system is discussed in [80]. The converter control is extended to the six-step mode from a regular SVPWM for the optimal dc link voltage controlled by an MTPA strategy.

However, this results in increased harmonic content in the output voltage waveforms. The inverter operating area also increases due to transition to the six-step mode. A control scheme is given to commutate between SVPWM and six-step operation. In [81], it is shown that the iron loss from the inverter PWM operation is the largest loss component at low speeds under high-torque conditions. A strong case for the use of a dc-dc converter is presented in [82], where a cascaded control structure is realized for both inductor current and output voltage. Discontinuous conduction mode has been used to improve the converter's efficiency at low loads. Also, the desired dc link voltage is calculated based on the stator flux linkage which corresponds to the requested torque on the MTPA trajectory. An efficiency table for reduced dc link voltage to reduce losses in NEDC drive cycle, is given in Table 2.6. Machine core losses have been neglected in these simulations.

Table 2.6: Percentage Energy Savings for NEDC Drive Cycle [76]

Efficiency at low speeds	DC link voltage		
	400 V	300 V	200 V
Machine	95.8 %	96.1 %	96.9 %
Inverter	86.3 %	86.9 %	87.4 %

2.5 Concluding Remarks

The literature survey reviewed various component-level loss minimization strategies in induction machine drives. Widely used machine loss reduction, MTPA and dc link current reduction have been discussed. Most of these methods have focused on component loss minimization. However, system-level loss minimization is essential to obtain overall energy savings in a drive. Also, any loss minimizing method should be capable of addressing a

wide range of speed and torque operating conditions, especially in automotive and more-electric aircraft applications.

Existing methods for damping resonant oscillations caused by the use of passive LC filters were presented. The disadvantages of passive damping methods were also highlighted, implying the need for active damping. A simple transfer function-based method will be used to choose the resistance value in the active damping controller. As this resistance is only virtual, its value can be dynamically adjusted.

Advantages of using a variable dc link scheme have been highlighted. A fixed, high-voltage dc bus will not result in an optimal system operation. Efficiency improvements highlight the benefits of using a dc-dc converter to obtain variable voltage. This dissertation will investigate whether it is beneficial to use variable dc link voltage for all operating conditions. All the above aspects will be addressed in the following chapters.

Chapter 3

SYSTEM-LEVEL DRIVE LOSS MINIMIZATION

Most loss minimization methods have focused on loss reduction only in particular components such as machine copper and core, inverter or its dc link. However, loss minimization in a specific component cannot ensure minimum drive system loss. This chapter presents a comprehensive model-based optimization approach to obtain minimum system loss. This approach will be demonstrated on an FOC-based induction motor drive. Figure 3.1 shows a typical configuration of a VSI-based induction motor drive with passive filters and nonidealities. It is known that undesirable resonant oscillations are created in motor terminal voltages and currents because of the LC filter [51]. Passive methods to damp these oscillations require a physical resistor in the circuit, resulting in additional losses. An active lossless damping with virtual resistors will be discussed in detail in Chapter 4. The induction machine model and control are discussed in Section 3.1.

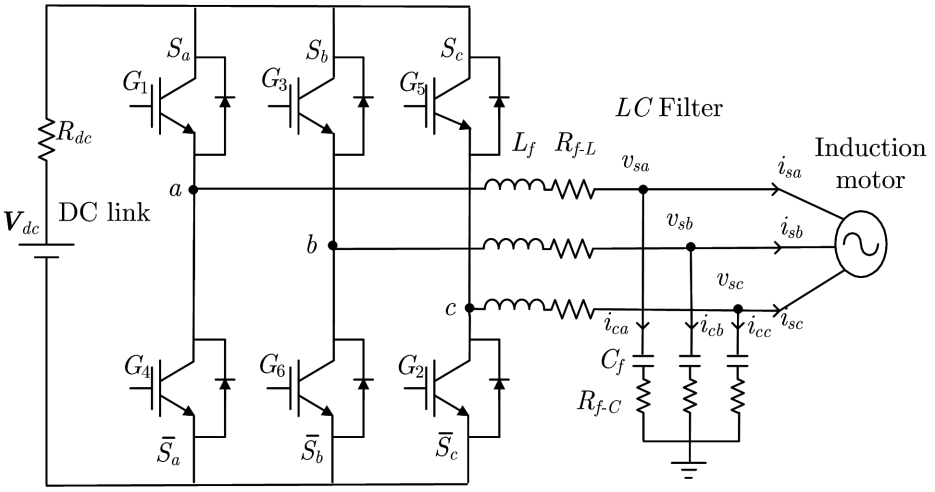

Figure 3.1: Three-phase VSI induction motor drive with nonidealities.

3.1 Induction Machine Model and Control

The dq-axis voltage equations of the induction motor, without considering saturation, in the synchronous reference frame [83] are given as

$$\begin{aligned} v_{ds} &= R_s i_{ds} + \frac{d}{dt}\lambda_{ds} - \omega_e \lambda_{qs} \\ v_{qs} &= R_s i_{qs} + \frac{d}{dt}\lambda_{qs} + \omega_e \lambda_{ds} \\ v_{dr} &= R_r i_{dr} + \frac{d}{dt}\lambda_{dr} - (\omega_e - \omega_r)\lambda_{qr} \\ v_{qr} &= R_r i_{qr} + \frac{d}{dt}\lambda_{qr} + (\omega_e - \omega_r)\lambda_{dr} \end{aligned} \tag{3.1}$$

where v, i, R, ω and λ represent voltage, current, resistance, angular velocity and flux linkages, respectively. The suffixes d and q represent the corresponding direct and quadrature axis components. Suffixes s and r refer to stator and rotor and ω_e denotes the synchronous speed in rad/s. The electromagnetic torque (T_e) developed by the motor can be expressed in many ways. A convenient form of the expression for FOC is given as

$$T_e = \frac{3}{2}\frac{n_p}{2}\frac{L_m}{L_r}(i_{qs}\lambda_{dr} - i_{ds}\lambda_{qr}) \tag{3.2}$$

where n_p is the pole number, and L_m, L_r refer to mutual and rotor inductances, respectively. For a squirrel cage rotor, $v_{dr} = v_{qr} = 0$ in (3.1).

Field oriented control seeks to decouple flux (i_{ds}) and torque-producing (i_{qs}) stator current components to achieve control capabilities analogous to those of a dc machine. Use of rotor flux orientation aligns the rotor flux vector $\left(\overrightarrow{\lambda_r}\right)$ with the d-axis, enforcing $\lambda_{qr} = 0$ and $\lambda_{dr} = \left|\overrightarrow{\lambda_r}\right|$. The electromagnetic torque equation under this control reduces to

$$T_e = K_t \lambda_r i_{qs} \tag{3.3}$$

The rotor flux λ_r in steady state and the machine constant K_t are given as

$$\lambda_r = L_m i_{ds}, K_t = \frac{3}{2}\frac{n_p}{2}\frac{L_m}{L_r} \tag{3.4}$$

Figure 3.2 shows a block diagram of an FOC implementation for VSI, along with an active damping loop. The active damping controller is important because any harmonic component of inverter voltage that is close to the resonant mode of the motor-filter combination can cause undesirable oscillation in the motor terminal voltages and currents [53, 69]. This resonant mode depends on the effective inductance, capacitance and resistance values in the circuit. For a typical active damping implementation, the current flow (i_{d-damp}) and (i_{q-damp}) in the virtual damping resistor across the filter capacitor is emulated in the control loop using resonant components of motor voltage feedback. These damping currents are then subtracted from the output of flux and speed controller blocks, to yield the required set of d and q axis stator current references, respectively, for the inverter. To obtain the desired steady-state and dynamic performance of the controller, a small-signal transfer function-based approach can be used to select the resistance value [84].

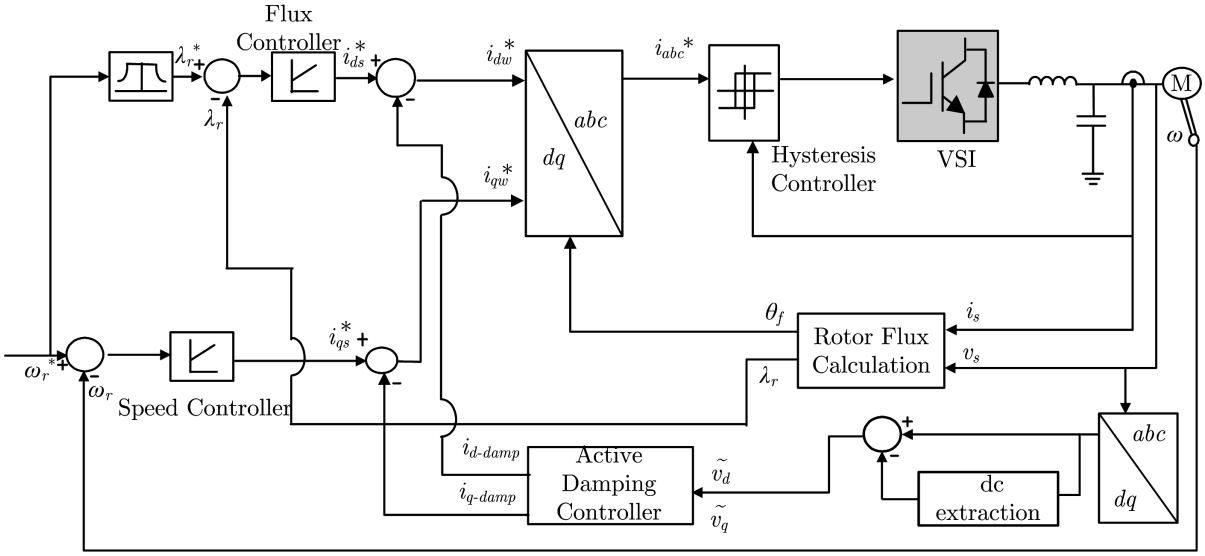

Figure 3.2: Rotor flux FOC implementation in VSI with active damping controller.

3.2 Loss Models of Induction Motor Drive Components

Electrical losses in the drive system occur in the machine as stator and rotor copper and core losses, in the inverter as conduction and switching losses, and in the equivalent series resistances (ESR) of filter components and dc link capacitor. The steady-state loss equations of each drive component depicted in Figure 3.1, are discussed below.

3.2.1 Stator and Rotor Copper Losses

Losses occurring in both stator and rotor winding resistances are called as "copper losses", even if the cages are made of aluminum. These are directly given in the *d-q* reference frame as

$$P_{cu-loss} = \left(i_{ds}^2 + i_{qs}^2\right) R_s + \left(i_{dr}^2 + i_{qr}^2\right) R_r \tag{3.5}$$

Using FOC with rotor-flux orientation, the steady-state stator and rotor current components can be derived as

$$i_{ds} = \frac{\lambda_r}{L_m}, i_{qs} = \frac{T_e}{K_t \lambda_r}, i_{dr} = 0, i_{qr} = -\left(\frac{L_m}{L_r}\right) i_{qs} \tag{3.6}$$

3.2.2 Core Losses

Widely used empirical expressions for the hysteresis and eddy current losses, lumped together as core losses ($P_{core} = P_{hys} + P_{eddy}$) are given as

$$P_{hys} = K_h f \lambda_s^{1.6} \tag{3.7}$$

$$P_{eddy} = K_e f^2 \lambda_s \tag{3.8}$$

In the above expressions, λ_s refers to the stator flux magnitude. K_h and K_e are constants

depending on the number of turns and core material and geometry. These constants can be empirically determined from experimental machine loss data found at various frequencies (f). Under FOC operation, the stator flux magnitude, in terms of the rotor flux variable, can be expressed as

$$\lambda_s = (\sigma L_s i_{qs})^2 + \left(L_m \frac{\lambda_r}{L_r} + \sigma L_s i_{ds} \right)^2 \tag{3.9}$$

where σ refers to the machine leakage factor, given as $1 - L_m^2 / (L_s L_r)$.

3.2.3 Losses in Filter Resistances

Connecting leads and plates have resistance in a practical capacitor. Leakage resistance is also present due to imperfect insulation. Both effects can be modeled as a single ESR which results in a non-zero power loss [85]. Usually, ESR losses in the filter inductor (R_{f-L}) and capacitor (R_{f-C}) are insignificant in a typical motor power range. However, for the sake of completeness, the losses ($P_{filter-loss} = P_{C-fil} + P_{L-fil}$) can be given as

$$P_{C-fil} = \left(i_{cd}^2 + i_{cq}^2 \right) R_{C-fil} \tag{3.10}$$

$$P_{L-fil} = \left(i_{dw}^2 + i_{qw}^2 \right) R_{L-fil} \tag{3.11}$$

where i_{dw}, i_{qw} are the inverter output currents flowing through the filter inductor and i_{cd}, i_{cq} are the currents flowing through the capacitor. ESR values can be obtained from datasheets or known parasitic estimation methods [85]. Core losses in the filter inductor are neglected in the considered power range. If film-based ac capacitors with low ESR values are used, R_{f-C} is negligible. Typical ESR values of standard ac voltage aluminum capacitors do not exceed a few hundred milliohms. The steady-state capacitor currents in (3.10) can be found as

$$i_{cd} = \omega_e v_{qs} C_f, \qquad i_{cq} = -\omega_e v_{ds} C_f \tag{3.12}$$

where v_{ds} and v_{qs} can be evaluated from (3.1) for given operating conditions. The inverter output currents in (3.11) can be expressed as

$$i_{dw} = \left(\frac{1 - \omega_e^2 C_f \sigma L_s}{L_m} - \frac{\omega_e^2 C_f L_m}{L_r} \right) \lambda_r - \left(\frac{\omega_e C_f R_s T_e}{K_t} \right) \frac{1}{\lambda_r} \tag{3.13}$$

$$i_{qw} = \frac{T_e}{K_t \lambda_r} \left(1 - \omega_e^2 C_f \sigma L_s \right) + \left(\frac{\omega_e C_f R_s}{L_m} \right) \lambda_r \tag{3.14}$$

3.2.4 DC Link Losses

Inverter dc link losses occur in the input capacitor ESR and additional cable resistances. These resistances are lumped as R_{dc}. The losses are given as

$$P_{dc-loss} = i_{dc}^2 R_{dc} \tag{3.15}$$

where $i_{dc}^2 = i_{dw}^2 + i_{qw}^2$.

3.2.5 Power Semiconductor Losses

Switch on-states can be modeled as a forward voltage drop in series with a resistance. Conduction losses (P_{cond}) are a function of the forward voltage (V_{for}) and the on-state series resistance (R_{on}) and given as

$$P_{cond} = V_{for} < |I| > + I_{rms}^2 R_{on} \tag{3.16}$$

where $< |I| >$ and I_{rms} refer to the averaged magnitude and rms value of current flowing through the switch, respectively.

Switching losses (P_{sw}) due to nonideal commutation during turn-on (t_{on}) and turn-off

(t_{off}) intervals are directly proportional to switching frequency (f_{sw}). Assuming a first-order approximation to device current transition, the switching loss in each device can be approximated as

$$P_{sw} = V_{off} < |I| > (t_{on} + t_{off})\, f_{sw} \tag{3.17}$$

where V_{off} is the off-state switch voltage. For an aperiodic current controller, the average of f_{sw} can be substituted.

3.3 Component-Level Loss Optimization Schemes

Some widely used techniques for component-level loss minimization were reviewed in Section 2.1.2 and are briefly outlined below. The drive system loss obtained using each of these methods will be compared.

3.3.1 Machine Loss Optimization

The fundamental idea of machine loss reduction involves achieving a favorable balance between copper and core losses [21, 24]. In an FOC-based VSI drive, machine losses can be expressed as a function of the rotor flux variable [27]. The optimum (load-dependent) flux that results in minimum machine losses is used as the reference command. Other control variables such as stator flux or air-gap flux can also be used to implement machine loss minimization. The objective function for machine loss minimization ($P_{machine-loss}$) is obtained by adding losses in (3.5), (3.7) and (3.8).

3.3.2 Maximum Torque per Stator Ampere (MTPA)

Maximum torque per ampere control is equivalent to stator current minimization for a given load torque [33]. For an FOC-based drive, the developed electromagnetic torque is given as $T_e = K_t L_m i_{ds} i_{qs}$. The value of rotor flux required to minimize stator current can be derived as

$$\lambda_r = \sqrt{\frac{T_e L_m}{K_t}} \tag{3.18}$$

It is obvious that the MTPA approach can minimize the stator current and, hence, the stator copper losses. Although this strategy does not, in general, yield the same flux as in true machine loss optimization, it offers a convenient tradeoff that emphasizes stator copper loss optimization. Maximum torque per ampere control can be extended to the field-weakening region, as discussed in [35].

3.3.3 DC Link Loss Minimization

The dc link losses in a drive may not be negligible, particularly when the ESR of the dc link storage element and the connecting cable resistances are large. So, control techniques to minimize the dc link current have also evolved [37]. Use of shunt capacitors at the inverter output, as shown in Figure 3.1, can reduce the dc link current requirement, leading to lower losses in the dc link and the inverter, even though the stator current demand is fixed for given torque and flux references. The objective function ($P_{dclink-loss}$) that is minimized here, is given in (3.15).

The control methods discussed above can reduce specific loss components in the drive but cannot guarantee minimum total loss. Therefore, a comprehensive system loss function combining individual component losses is developed.

3.4 Constrained System Loss Function Formulation

An overall loss function is formulated to achieve minimum system-level losses, as

$$P_{loss}^{total} = P_{machine-loss} + P_{dclink-loss} + P_{filter-loss} + P_{cond} + P_{sw} \tag{3.19}$$

The rotor flux is usually maintained at the rated value to achieve a high degree of dynamic performance, but this leads to increased losses, particularly at light loads. Losses can be

reduced by dynamically varying the rotor flux command based on operating conditions. The total loss in (3.19) is a function of rotor flux and capacitance, for a given mechanical load. In a current-controlled VSI, the series inductance value is selected based on the maximum switching frequency and switching ripple targets. Analytical optimization of (3.19) can be unwieldy, since the total loss expression is complex. So, a grid search is used to find the optimum rotor flux (λ_{opt}) and capacitance values (C_{opt}), given constraints on both. Using flux maps from look-up tables for various operating conditions, instabilities and convergence problems associated with dynamic optimization can be avoided [75]. Lower and upper bounds on optimum flux should be enforced to ensure machine operation within thermal and saturation limits: $\lambda_{therm} \leq \lambda_{opt} \leq \lambda_{sat}$. The thermal limit is

$$\lambda_{therm} = \frac{T_e}{K_t i_{qsmax}} \tag{3.20}$$

where i_{qsmax} is the maximum allowable q-axis stator current for the given operating point. For a practically feasible design, limits are also enforced on the optimum capacitance value: $C_{lower} \leq C_{opt} \leq C_{upper}$. Upper and lower limits are chosen to reflect physical size limitations and total harmonic distortion (THD) specifications, respectively. A conceptual step-wise procedure of the system-level optimization is given in Figure 3.3.

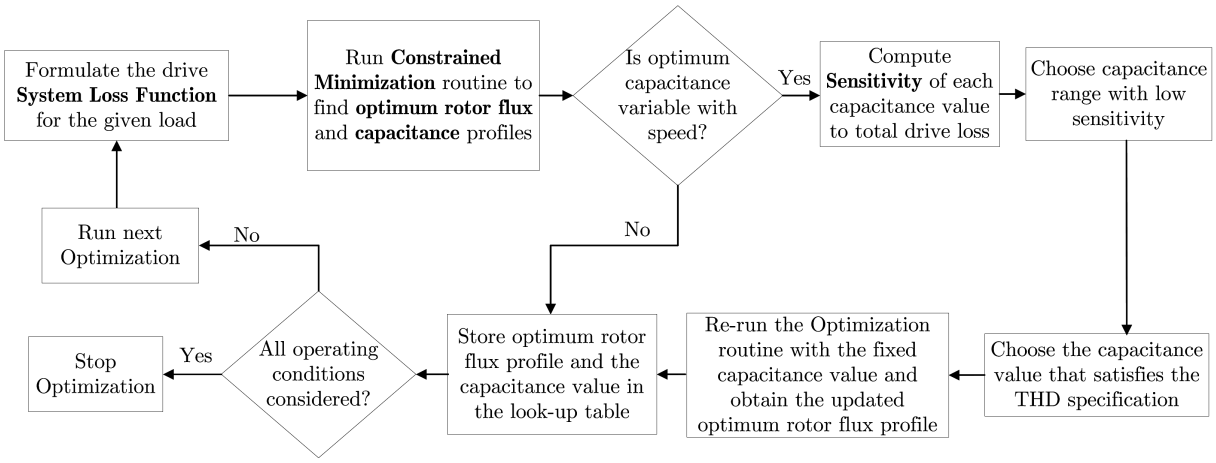

Figure 3.3: Procedural development of system-level optimization.

3.5 Simulation Studies

Both the component-level and proposed constrained system-level loss minimization schemes discussed in Sections 3.3 and 3.4 are simulated on a 3-ϕ, 5 hp induction motor drive, for a wide range of rotor speeds and torques. Details are given in Table 3.1. Table 3.2 gives the results achieved at rated speed under different methods both at light (3 Nm) and rated load (15 Nm). Loss reduction is about 7% compared to the best conventional alternative (machine optimization in this example) and more than 16% compared to MTPA. Notice that machine optimization gives the best results among the prior examples. Although MTPA does not inherently address core loss, the emphasis on current minimization tends to reduce loss in the dc link and filter components.

Table 3.1: Drive Parameters for Simulation Studies

Induction motor	460 V, 3-ϕ, 5 hp, 60 Hz, 1750 rpm
Stator resistance (R_s), Leakage inductance (L_{ls})	1.115 Ω, 5.974 mH
Rotor resistance (R'_r), Leakage inductance (L'_{lr})	1.083 Ω, 5.974 mH
Rotor flux saturation limit (λ_{sat})	1.1 Vs
Mutual inductance (L_m)	203.7 mH
Hysteresis and eddy current loss constants	$K_h = 1.9 \times 10^5$, $K_e = 3.2 \times 10^3$
Number of pole pairs (P)	2
Shunt capacitor range	$C_{lower} = 5$ μF, $C_{upper} = 35$ μF
Series inductance, Fixed shunt capacitance	11 mH, 35 μF
Equivalent series resistances	$R_{dc} = 4$ Ω
	$R_{f-C} = 0.1$ Ω, $R_{f-L} = 0.25$ Ω
DC link voltage	$V_{dc} = 600$ V

Table 3.2: Total Loss Comparison at Rated Speed

Control Scheme	Total loss at 2 Nm (W)	Total loss at 15 Nm (W)
Machine loss minimization	139	531
Maximum torque per ampere	151	593
DC link loss minimization	466	591
System-loss minimization	130	494

Loss curves for various rotor speeds are shown in Figure 3.4. It is clear that the total loss obtained from constrained system-based minimization is the lowest, except in the low-speed range due to the constraint on the capacitance values. DC link current minimization causes higher losses and must be avoided, particularly at light loads. Figure 3.5 shows that the optimum flux profile for MTPA is not dependent on speed, whereas a system-based approach benefits from modest field weakening that increases with speed.

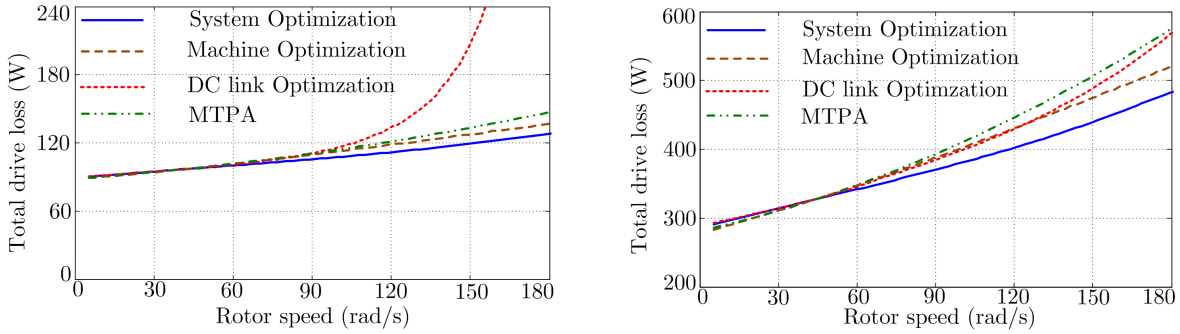

Figure 3.4: Total loss comparison for different optimization schemes at various rotor speeds for (a) $T_{load} = 3$ Nm (b) $T_{load} = 15$ Nm.

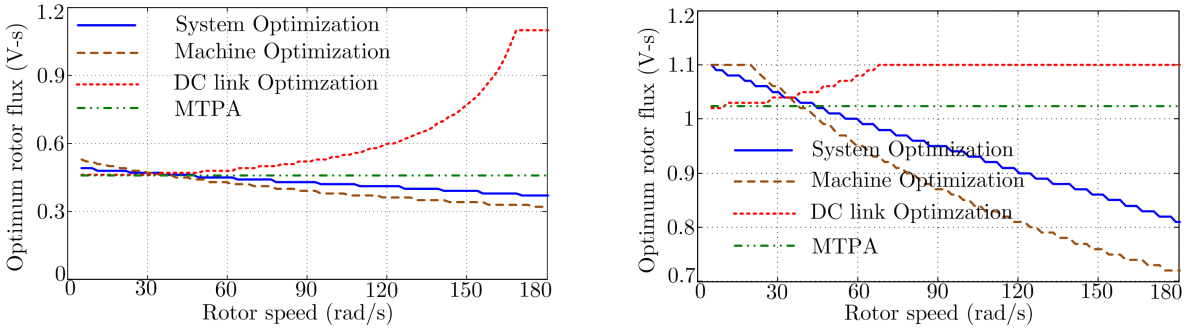

Figure 3.5: Optimum flux comparison for different optimization schemes at various rotor speeds for (a) $T_{load} = 3$ Nm (b) $T_{load} = 15$ Nm.

The capacitance profile for system-based optimization in Figure 3.6b indicates that the best value of filter capacitance is dependent on speed. Given the practical challenges of speed-varying capacitance, loss sensitivity to the capacitance value was explored. Figure 3.7 confirms that minimum losses are relatively insensitive to capacitance values in the range considered (5−35 μF) for optimization. As such, a fixed-value capacitance can be used. Figure 3.8 indicates that total loss depends very strongly on rotor flux than the capacitance value. Fixing C_{opt} at 35 μF, the percentage distribution of constituent losses in the system is shown in Figure 3.9.

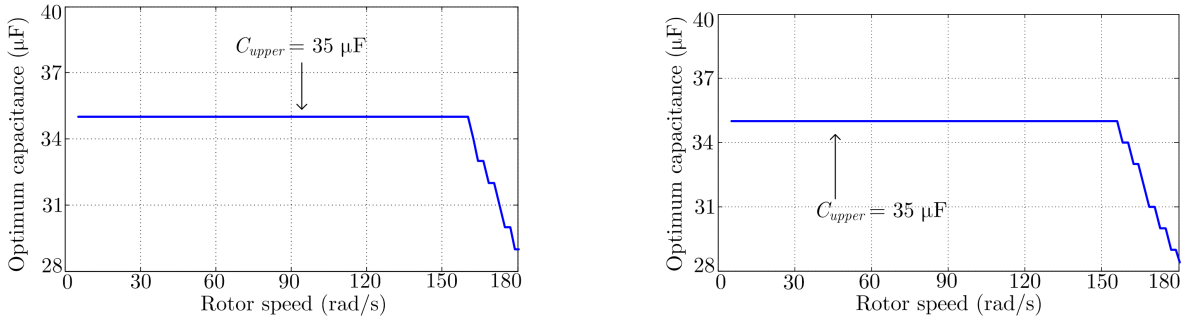

Figure 3.6: Optimum capacitance comparison for different optimization schemes at various rotor speeds for (a) $T_{load} = 3$ Nm (b) $T_{load} = 15$ Nm.

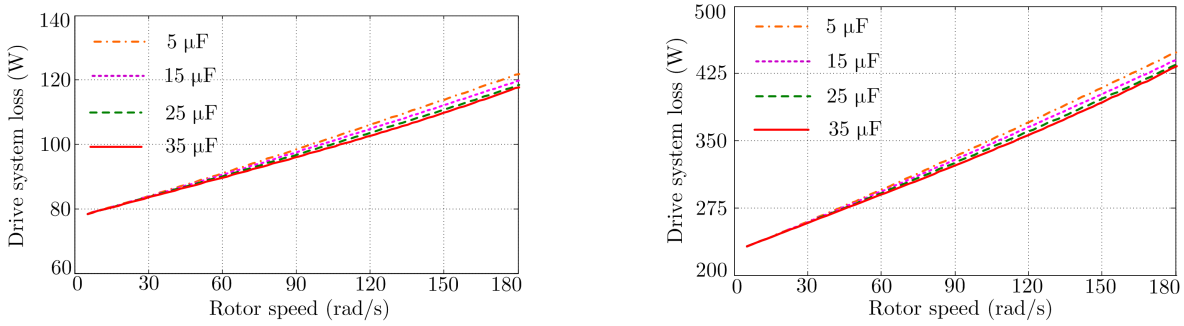

Figure 3.7: Total loss versus rotor speed at different capacitance values (a) $T_{load} = 3$ Nm (b) $T_{load} = 15$ Nm.

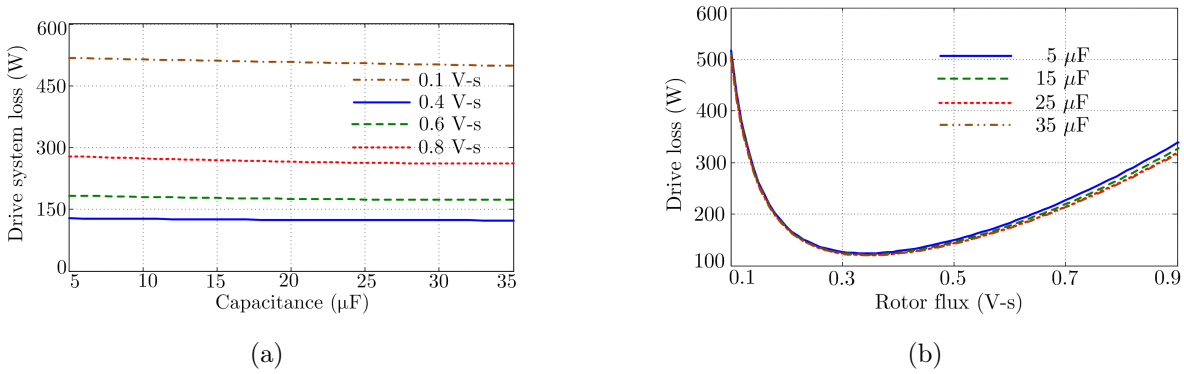

Figure 3.8: (a) Total loss versus capacitance at constant flux (b) Total loss versus rotor flux at constant capacitance.

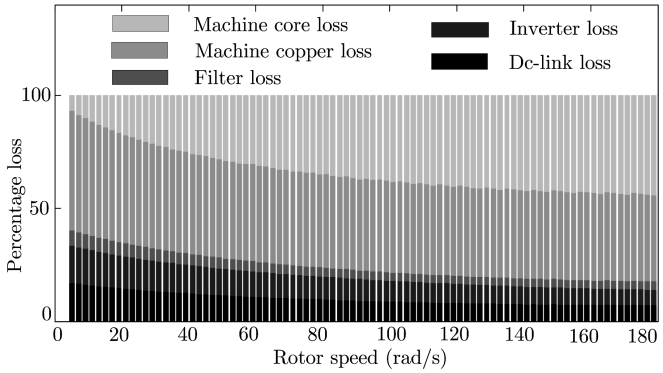

Figure 3.9: Percentage constitution of different loss components for the minimum total loss condition at $T_{load} = 15$ Nm.

3.5.1 Drive Cycle Case Study

A sample drive cycle, as shown in Figure 3.10 is used to validate system-based loss optimization benefits for variable speed and torque demand profiles [86]. With C_{opt} fixed at 35 μF for the drive cycle, Figure 3.11 compares the total drive loss and flux profiles among the different schemes. From Table 3.3, it can be found that the cumulative energy loss percentage for the entire drive cycle is a minimum for the system-level optimization scheme. This shows a 6% loss reduction compared to machine optimization.

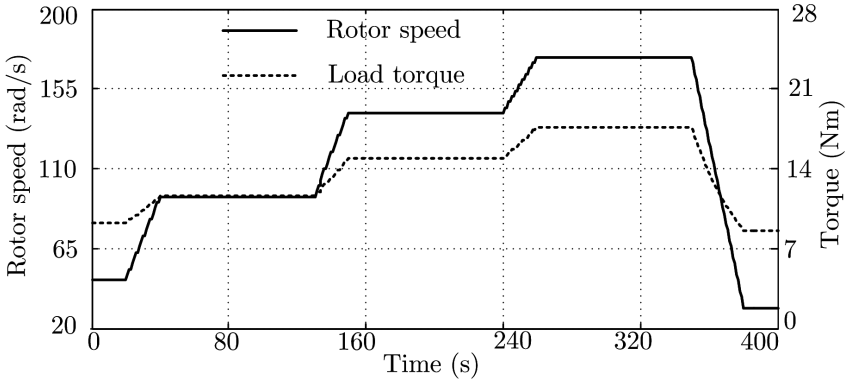

Figure 3.10: Sample drive cycle used for simulation.

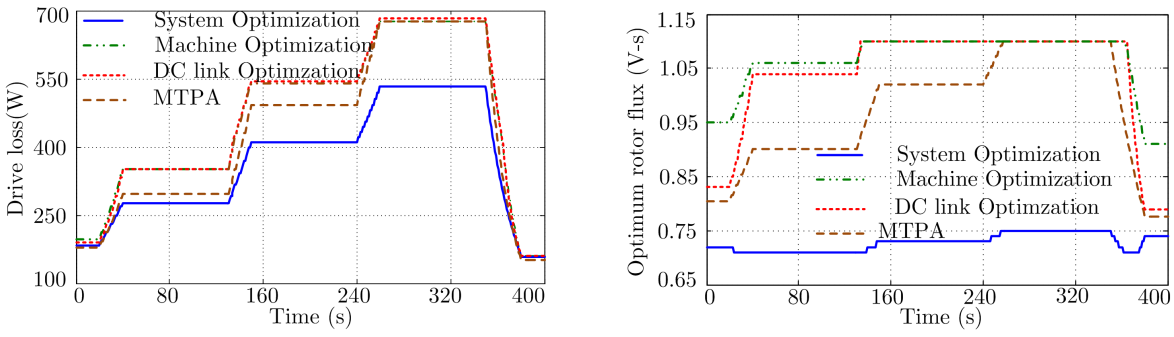

(a) (b)

Figure 3.11: Sample drive cycle case: (a) Total loss comparison (b) Optimum rotor flux profile.

Table 3.3: Drive Cycle Cumulative Energy Loss Comparison

Control Scheme	Energy Loss (%)
Machine loss minimization	26.8
Maximum torque per ampere	29.7
DC link loss minimization	29.9
System-loss minimization	25.3

3.6 Experimental Verification

A 2 hp induction motor drive with an IGBT-based, two-level inverter is used for experimental studies. The experimental drive parameters are given in Table 3.4.

Table 3.4: Drive Parameters for Experimental Studies

Induction motor	230 V, 3-ϕ, 2 hp, 60 Hz, 3450 rpm
Stator resistance (R_s), Leakage inductance (L_{ls})	1.207 Ω, 4.083 mH
Rotor resistance (R'_r), Leakage inductance (L'_{lr})	1.128 Ω, 6.094 mH
Mutual inductance (L_m)	154.9 mH
Number of pole pairs (P)	1
Series inductance, Fixed shunt capacitance	28 mH, 50 μF
Equivalent series resistances	$R_{dc} = 0.7$ Ω
	$R_{f-C} = 0.1$ Ω, $R_{f-L} = 0.1$ Ω
DC link voltage	$V_{dc} = 300$ V
Load torque	$6 \times 10^{-6}\omega_r^2 + 3.5 \times 10^{-3}\omega_r + 0.1958$

Experimental sensitivity of drive loss to both rotor flux and capacitance variables is explored. Total loss is strongly dependent on rotor flux than the capacitance value, validating the simulation results. The graphs indicating drive loss sensitivity at different

operating points, are shown in Figures 3.12, 3.13 and 3.14.

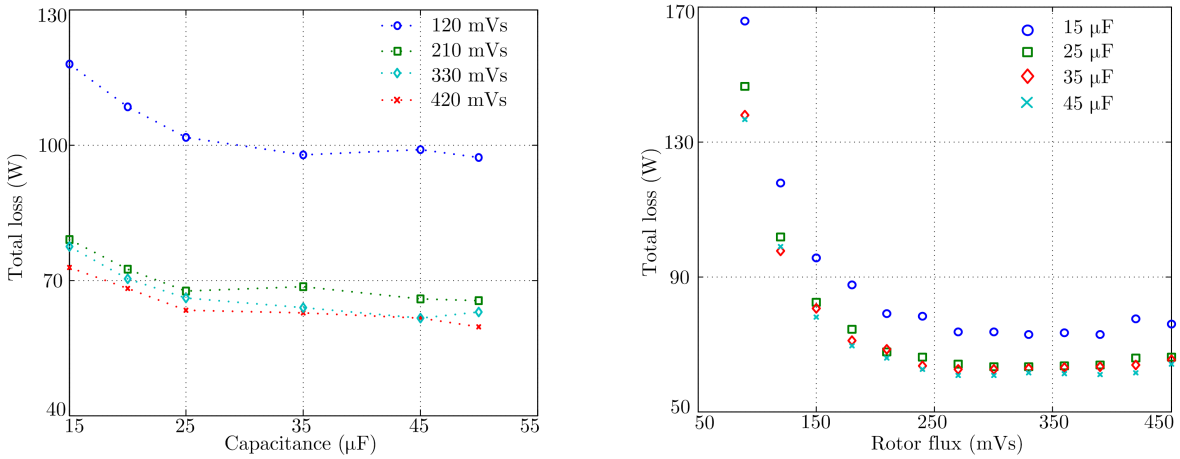

(a) (b)

Figure 3.12: Results at 100 rad/s and 0.5 Nm (a) Total loss versus capacitance (b) Total loss versus rotor flux.

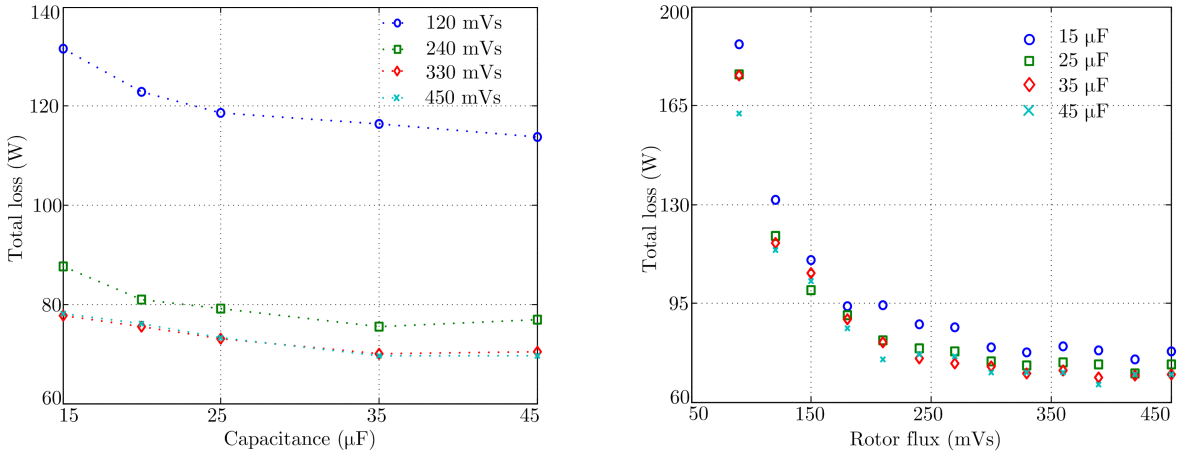

(a) (b)

Figure 3.13: Results at 300 rad/s and 0.5 Nm (a) Total loss versus capacitance (b) Total loss versus rotor flux.

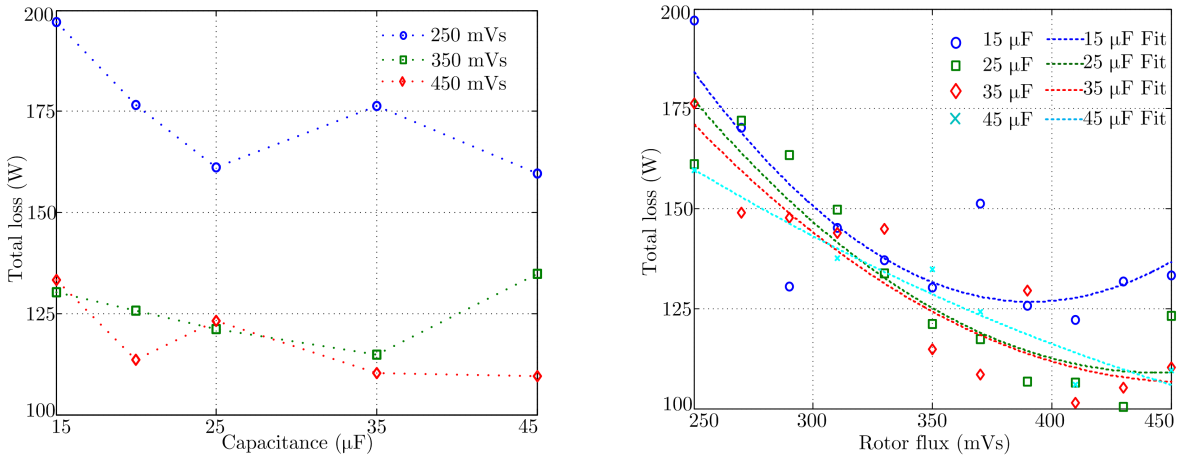

(a) (b)

Figure 3.14: Results at 300 rad/s and 1.4 Nm (a) Total loss versus capacitance (b) Total loss versus rotor flux.

The drive cycle speed and torque profiles implemented in the experiment are shown in Figure 3.15. The instantaneous drive cycle power is calculated from the dc bus voltage (v_{dc}) and current (i_{dc}) waveforms sampled from a Tektronix MSO4034 mixed signal oscilloscope at the rate of 2500 samples/second, as shown in Figure 3.16. Real-time values of the experimental rotor speed and flux, sampled from the RTDX (Real Time Data eXchange) channels of the MATLAB interface, are plotted in Figures 3.17 and 3.18.

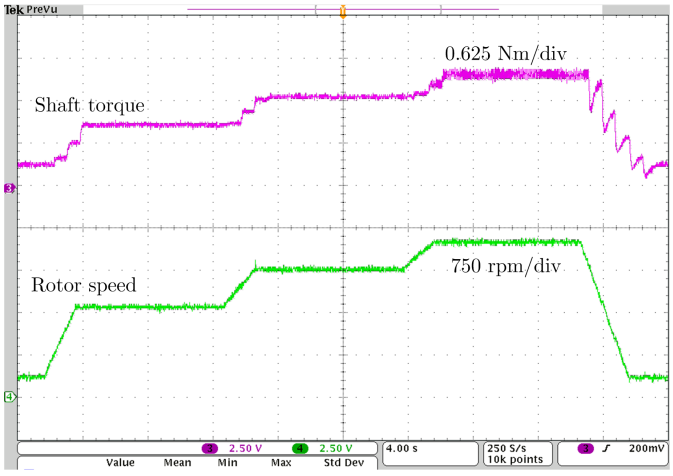

Figure 3.15: Sample drive cycle implementation in the experiment.

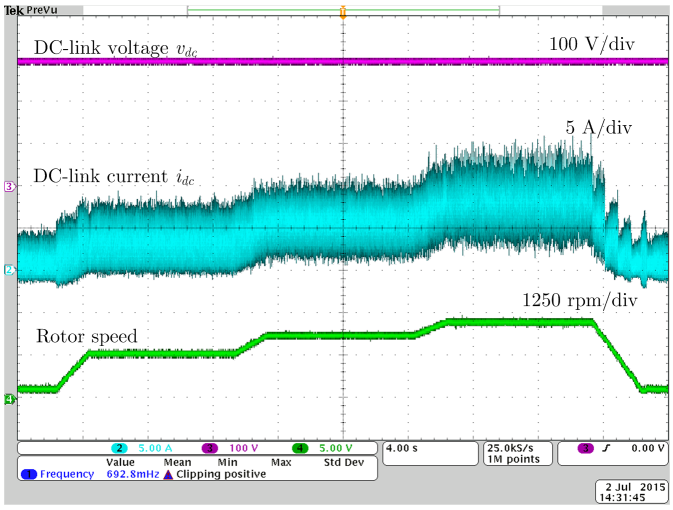

Figure 3.16: DC link voltage and current waveforms used for instantaneous power calculation.

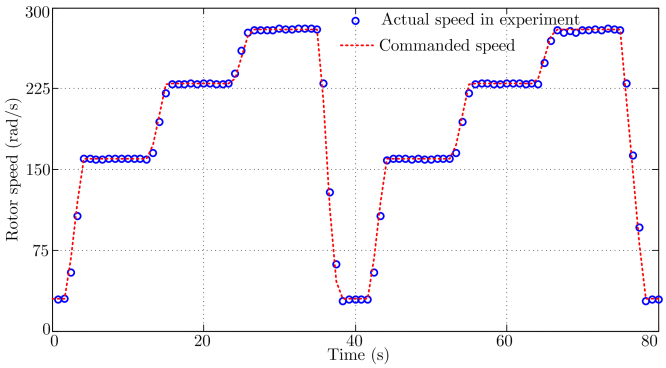

Figure 3.17: Sampled real-time experimental rotor speed.

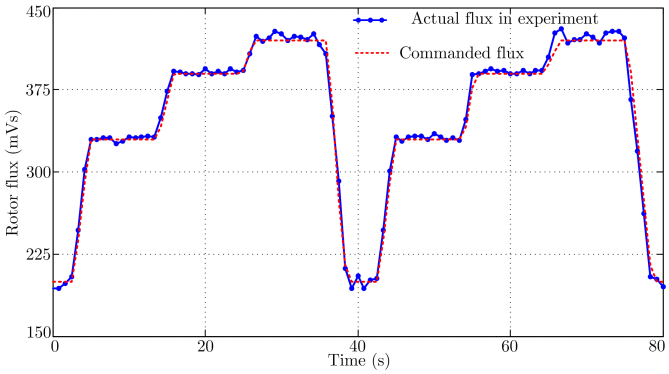

Figure 3.18: Sampled real-time experimental rotor flux.

The energy input to the drive system from the dc side can be calculated as

$$E_{dc-input} = \int_0^{T_{drv}} v_{dc}(t) i_{dc}(t) dt \tag{3.21}$$

where T_{drv} refers to the entire duration of the drive cycle. The cycle's cumulative energy consumption can be computed from the expression

$$E_{drive-cycle} = \int_0^{T_{drv}} T_{load} \omega_r dt \tag{3.22}$$

Energy calculations shown in (3.21) and (3.22) are computed offline. The net energy loss in the cycle can be easily computed as $(E_{dc-input} - E_{drive-cycle})$. It can be seen from Table 3.5 that system-level optimization gives the highest energy efficiency, verifying the simulation results.

Table 3.5: Experimental Drive Cycle Energy Efficiency Comparison

Control Scheme	Avg. loss (W)	Energy efficiency (%)
Machine loss minimization	128	65.2
Maximum torque per ampere	127	65.5
DC link loss minimization	107	69.2
System-loss minimization	98	71.4

3.7 Discussion on the Dynamic Limits of Optimization

The optimization routines discussed previously have been executed as offline procedures. It is known that online loss minimization depending on iterative measurements of input power suffers from convergence issues [7]. Instead of relying exclusively on input power measurements to determine the optimum control variable, model-based optimization can also be executed in an online manner. However, there are different limits imposed by such an optimization and are briefly discussed in the following.

3.7.1 Model Adjustment for New Conditions

Though the model developed in equations (3.1) is dynamic, a point-wise optimization has been carried out in the implementation. For a single operating point, the time required to run the optimization routine is observed to be less than 1 ms (≈0.75 ms) on a personal computer (Intel® Core i5-2430M CPU @ 2.40 GHz 64 bit). This value is much smaller than the machine time constants. The torque and speed information of the operating point are taken to be readily available as optimization inputs. If delays due to the torque and speed sensor outputs are ignored, the optimum variable can be updated as fast as the optimization execution time.

3.7.2 Limits Imposed by Machine Time Constants

Accurate tracking of optimum control variables depend on actual slew rates of the control variables, governed by machine time constants. Though the model optimization routine can be executed at a high speed, a highly dynamic drive cycle can be detrimental to the loss minimization objective if the actual variable is not able to closely follow the optimum command profile, leading to sub-optimal operation. The maximum rate of change of the rotor flux command and rotor time constant in the experiment are found to be around 70 mVs/s and 0.2 s respectively, which support dynamic tracking with reasonable accuracy. Valid update rates in such a case will be of the order of one second. If rapid changes in the optimum command profile do not support dynamic tracking, averaging methods on the drive cycle characteristics can be alternatively explored.

3.7.3 Long-Term Accuracy

It is known that machine parameters such as the stator and rotor resistances are subject to variations as a result of long-term operations. These variations are generally much slower compared to the time scales discussed in the previous cases. Resistance variation in the windings due to thermal effects can be taken care of by directly updating the

resistance value based on temperature feedback. In the case of aging effects, the transition from optimum to sub-optimal operation happens only very gradually and can be taken care of by standard tests carried out periodically on the machine.

3.8 Concluding Remarks

A system-level loss minimization approach is formulated from widely known loss models for the components of the drive system, using a comprehensive loss model of an induction motor drive. Total losses from the proposed minimization are compared to the results from component-level methods. Results demonstrate that substantial loss reduction can be achieved with system-level loss minimization, whenever there are considerable component losses. A sample drive cycle has been used for demonstration on an FOC-based induction motor drive, to illustrate the cumulative loss minimization.

Chapter 4

ACTIVE DAMPING OF RESONANCE

Passive damping techniques have been used to damp resonant oscillations caused by the addition of LC filters at the inverter output. Figure 4.1 shows a typical configuration of a VSI induction motor drive with passive filters. Because passive methods result in additional losses, active damping controller using virtual resistors have been widely explored [55, 56, 58, 59]. Any controller design should be stable and effective throughout the entire drive operation. Virtual resistance is a crucial element in the damping controller. An incorrect choice of virtual resistance can result either in insufficient damping or an excessively damped system with poor dynamic characteristics. The ideal value should be adjusted for operating conditions. In this chapter, a method to determine the active damping resistance value directly using small-signal transfer functions is developed. The proposed method uses a small-signal model of an induction motor drive system derived around an operating point [60]. Instead of fixing the effective resistance value for all operating conditions, the value is adjusted based on desired response specifications. This offline procedure is repeated for various operating points to determine corresponding resistance values. The entire control design is formulated in the synchronous reference d-q frame, which provides flexibility to implement a differential damping approach where the virtual d and q axis resistance values (R_{d-m}) and (R_{q-m}) are not restricted to be equal.

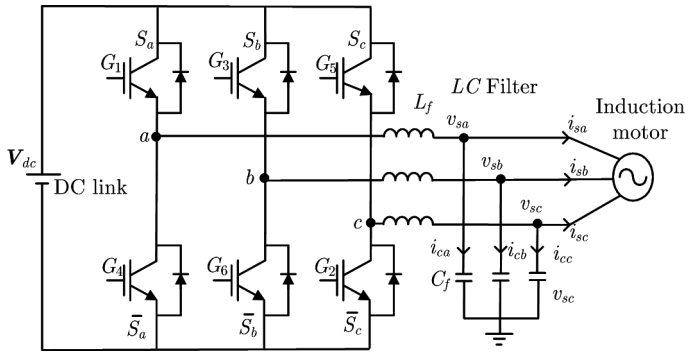

Figure 4.1: Three-phase VSI induction motor drive with output filters.

4.1 Active versus Passive Damping

Use of physical resistors across the capacitors to passively damp the resonant oscillations is subject to the following limitations.

- The resistance value is required to be equal in all the phases for a balanced system.
- Due to heat dissipation, size constraints and cooling requirements are involved.
- Once fixed, the effective resistance value cannot be easily altered to account for dynamic operating conditions.
- Fundamental and harmonic voltage components cannot be distinguished. This results in unwanted damping for fundamental components and possibly degraded performance.

Each of the above limitations can be overcome by using a virtual damping controller. By introducing virtual resistance in the transformed d-q domain, a differential damping approach is possible which allows selection of different resistance values in the d- and q-axes. Since no physical resistor is used, heat dissipation is not involved. The resistance value can be dynamically programmed into the controller. The resonant component can

be extracted from the motor voltages by using a low-pass filter, so that the fundamental motor voltage and current are not subject to damping ($R_{damp} = \infty$). The controller does not require resonant frequency information. Moreover, capacitor current feedback is not required to maintain field orientation. But, it should be noted that an incorrect choice of resistance value can result in a poor damping performance, as demonstrated in the following example.

Let arbitrarily low values of three-phase resistance be inserted across the capacitor at 0.5 s of simulation: Here, $R_{a-m} = R_{b-m} = R_{c-m} = 2\ \Omega$. The results are shown in Figure 4.2. Apart from a slow rotor speed transient response after damping is activated, excessive currents flow through the resistors. This can damage the inverter switches. For very high resistance values, say $R_{a-m} = R_{b-m} = R_{c-m} = 1500\ \Omega$, damping is ineffective as shown in Figure 4.3. Resonant oscillations are present even after damping has been activated. This indicates that an appropriate value must be determined.

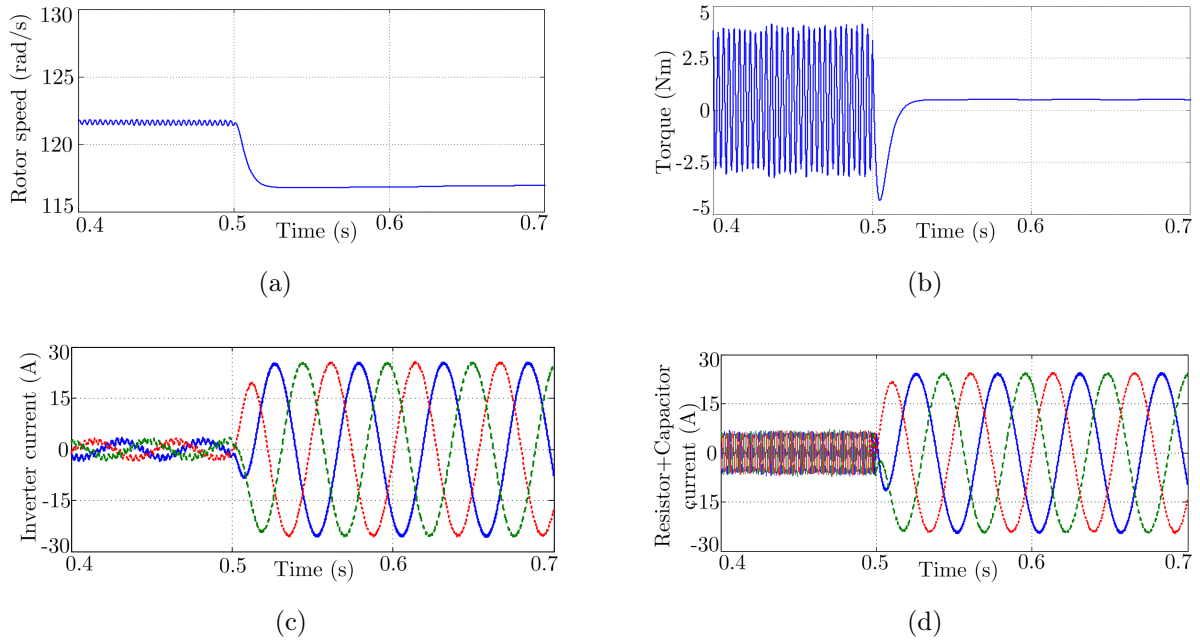

Figure 4.2: Effect of low damping resistance on: (a) rotor speed (b) torque (c) inverter currents (d) capacitor+resistor currents.

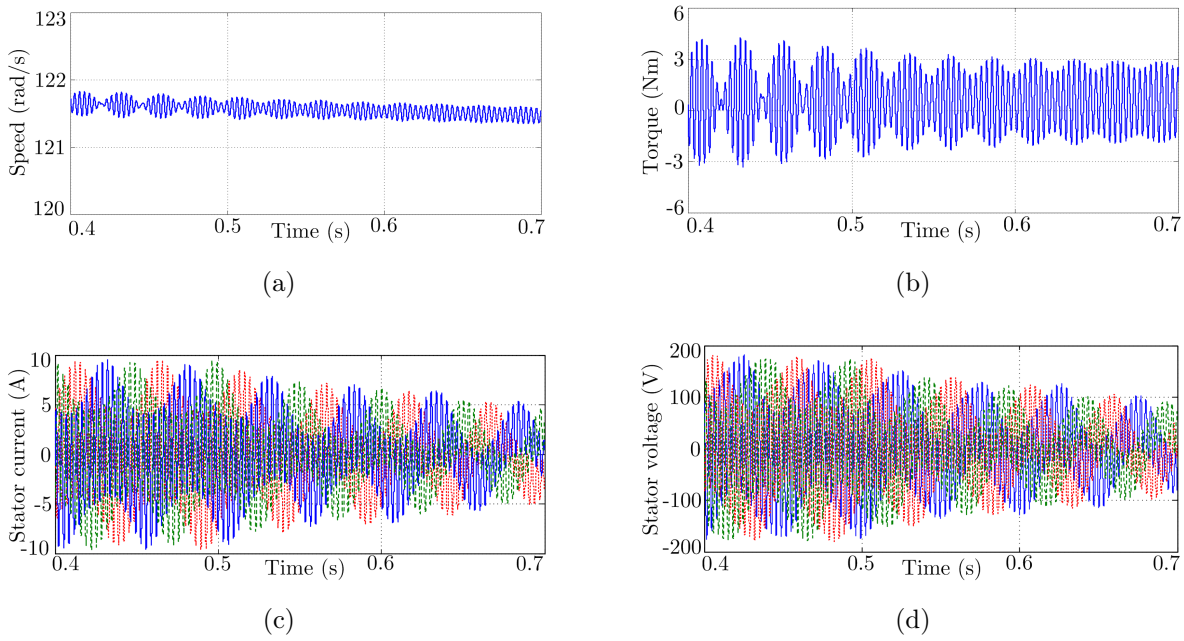

Figure 4.3: Effect of high damping resistance on: (a) rotor speed (b) torque (c) stator currents (d) stator voltages.

4.2 Mathematical Model of Machine-Filter System

A transformation from the stationary reference frame into a frame that rotates with the rotor flux vector, as proposed in [87], is used for the induction motor model. This gives a set of dynamic equations suitable for implementing rotor-flux FOC. The motor equivalent circuits in the d- and q-axes are shown in Figure 4.4. When FOC is applied, the equivalent circuits can be further simplified using $\psi_{qr} = 0$ and $\psi_{dr} = |\psi_r| = \psi$. Further, assuming negligible leakage factor ($\sigma = 0$) will result in $\psi_{qs} = 0$. The simplified equivalent circuits, given in Figure 4.5, indicate that the d-axis is independent of the speed voltage terms.

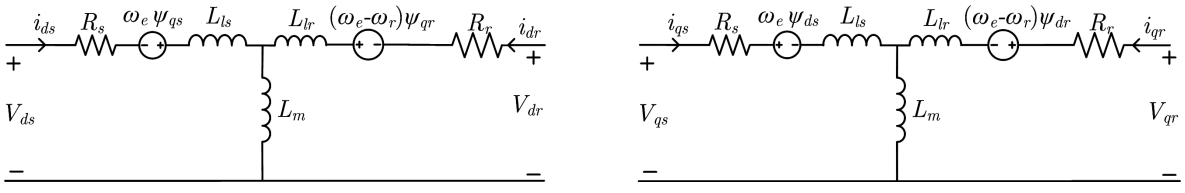

(a) (b)

Figure 4.4: Induction motor model in the synchronous reference frame in (a) d-axis (b) q-axis.

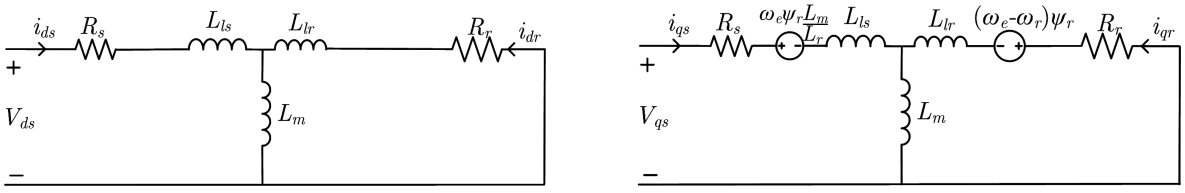

(a) (b)

Figure 4.5: Simplified model under FOC with leakage factor $\sigma = 0$ in (a) d-axis (b) q-axis.

The final equations of the fifth-order nonlinear induction motor model, without considering magnetic saturation, are (4.1)-(4.5). Core loss is neglected in this model, because it is frequency-dependent and requires adjusting for different speeds and therefore cannot be implemented with the current modeling framework. FOC operation is less-dependent on the core loss resistance, compared to other machine parameters [88].

$$\frac{d\omega_r}{dt} = \frac{3n_pL_m}{2JL_r}\psi i_q - \frac{T_{load}}{J} \tag{4.1}$$

$$\frac{d\psi}{dt} = -\frac{R_r}{L_r}\psi + \frac{R_rL_m}{L_r}i_d \tag{4.2}$$

$$\frac{di_{ds}}{dt} = -\left(\frac{L_m^2 R_r}{\sigma L_r^2} + \frac{R_s}{\sigma}\right) i_{ds} + \frac{L_m R_r}{\sigma L_r^2}\psi + n_p \omega_r i_{qs} + \frac{R_r L_m i_{qs}^2}{L_r \psi} + \frac{1}{\sigma} v_{ds} \tag{4.3}$$

$$\frac{di_{qs}}{dt} = -\left(\frac{L_m^2 R_r}{\sigma L_r^2} + \frac{R_s}{\sigma}\right) i_{qs} - \frac{L_m n_p}{\sigma L_r}\omega_r \psi - n_p \omega_r i_{ds} - \frac{R_r L_m i_{ds} i_{qs}}{L_r \psi} + \frac{1}{\sigma} v_{qs} \tag{4.4}$$

$$\frac{d\rho}{dt} = n_p \omega_r + \frac{R_r L_m i_{qs}}{L_r \psi} \tag{4.5}$$

Equation (4.5) represents the rate of change of rotor flux angle (ρ) and hence denotes the synchronous electrical frequency, ω_e. Since the filter forms a part of the stationary circuit, the filter variables must be transformed to represent the entire system in the synchronous frame. For current-controlled VSI applications, control is easier when the damping resistor is connected across the filter capacitor [56, 61]. The resulting d-axis and q-axis equivalent circuits of the motor-filter system are shown in Figures 4.6 and 4.7, respectively. The virtual damping resistor branch in Figure 4.6a is represented as a voltage-controlled current source, as shown in Figure 4.6b.

A useful damping controller should offer no resistance ($R_{d-m} = R_{q-m} = \infty$) to the fundamental voltage components. Only the oscillating components of capacitor voltages in the synchronous frame denoting the resonant components are used to generate the damping current references. A first-order, low-pass filter with cut-off frequency a, is used to extract fundamental capacitor voltage components.

$$\frac{dv_{d(q)s-filt}}{dt} = -a v_{d(q)s-filt} + v_{d(q)s} \tag{4.6}$$

Applying KCL at the node connecting the filter capacitance, virtual resistor and the stator terminal,

$$\frac{dv_{ds}}{dt} = \frac{i_{dw}}{C_f} - \frac{1}{R_{d-m}C_f}\left(v_{ds} - v_{ds-filt}\right) - \frac{i_{ds}}{C_f} + \omega_e v_{qs} \tag{4.7}$$

$$\frac{dv_{qs}}{dt} = \frac{i_{qw}}{C_f} - \frac{1}{R_{q-m}C_f}\left(v_{qs} - v_{qs-filt}\right) - \frac{i_{qs}}{C_f} - \omega_e v_{ds} \tag{4.8}$$

where $\left(v_{d(q)s} - v_{d(q)s-filt}\right)$ is the resonant voltage, also represented as $\widetilde{v}_{d(q)s}$. Similarly, the q-axis circuit is shown in Figure (4.7).

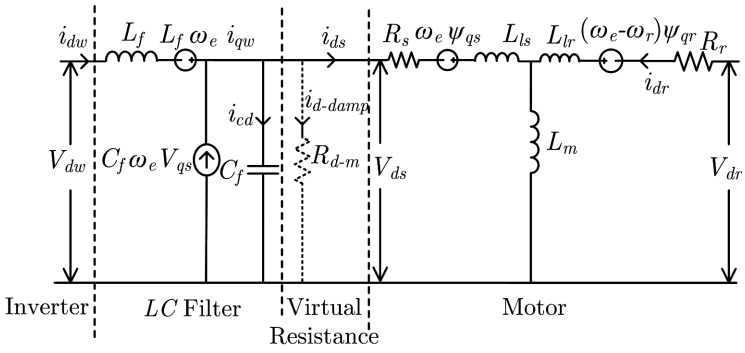

(a)

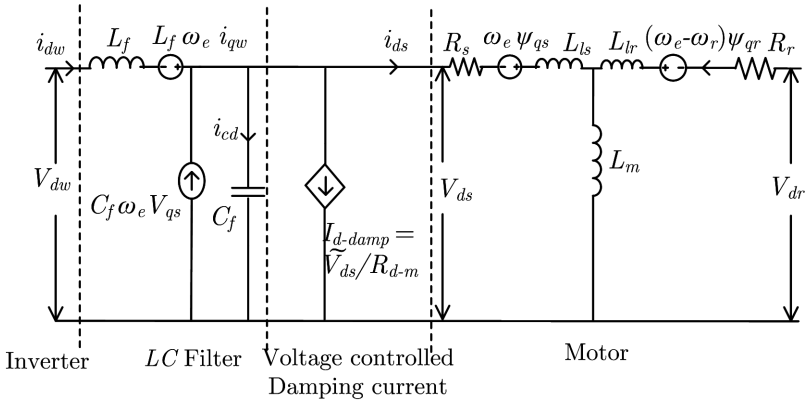

(b)

Figure 4.6: Damping in d-axis circuit of the motor-filter system represented as (a) virtual resistor (b) voltage-controlled current source.

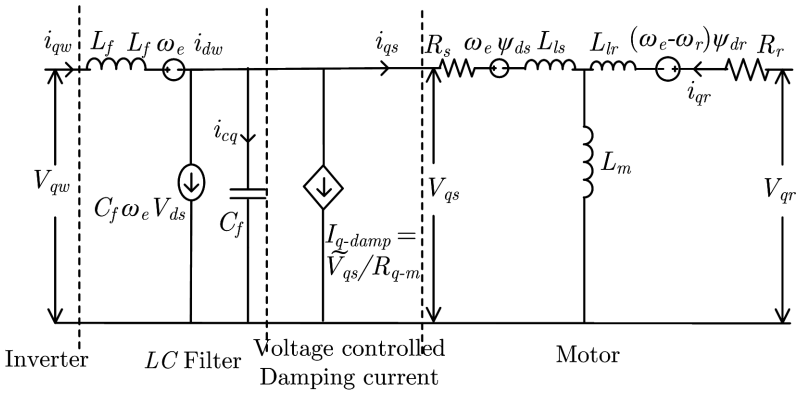

Figure 4.7: Damping in q-axis circuit of the motor-filter system.

Applying KVL across the inverter input and stator terminal voltage loop, the dynamics of inverter currents can be written as

$$\frac{di_{dw}}{dt} = \frac{v_{dw}}{L_f} - \frac{v_{ds}}{L_f} + \omega_e i_{qw} \tag{4.9}$$

$$\frac{di_{qw}}{dt} = \frac{v_{qw}}{L_f} - \frac{v_{qs}}{L_f} - \omega_e i_{dw} \tag{4.10}$$

The induction motor model in (4.1)-(4.5) is augmented with (4.6)-(4.10) to form a combined system. Since (4.5) represents the synchronous electrical frequency, it is substituted for ω_e in all the other equations. The final model represented by (4.1)-(4.10) is nonlinear. It is necessary to develop a linear approximate model to use conventional tools for analysis and control. This requires linearization of these equations about a quiescent operating point, using perturbation analysis [85, 89]. The derivatives in (4.1)-(4.10) are set to zero and solved for the state variables at equilibrium. Products of perturbations are ignored in the small-signal model because the perturbations are small by definition. Transfer functions can be derived, once a small-signal model is available around the given operating point. The perturbed state variables are

$$
\begin{aligned}
\omega_r &= \omega_{ss} + \hat{\omega_r} & v_{qs} &= V_{qs} + \hat{v}_{qs} \\
\psi &= \psi_{ss} + \hat{\psi} & v_{ds-filt} &= V_{ds-filt} + \hat{v}_{ds-filt} \\
i_{ds} &= I_{ds} + \hat{i}_{ds} & v_{qs-filt} &= V_{qs-filt} + \hat{v}_{qs-filt} \\
i_{qs} &= I_{qs} + \hat{i}_{qs} & i_{dw} &= I_{dw} + \hat{i}_{dw} \\
v_{ds} &= V_{ds} + \hat{v}_{ds} & i_{qw} &= I_{qw} + \hat{i}_{qw}
\end{aligned}
\tag{4.11}
$$

In (4.11), the vector $\begin{bmatrix} \hat{\omega_r} & \hat{\psi} & \hat{i}_{ds} & \hat{i}_{qs} & \hat{v}_{ds} & \hat{v}_{qs} & \hat{v}_{ds-filt} & \hat{v}_{qs-filt} & \hat{i}_{dw} & \hat{i}_{qw} \end{bmatrix}^T$ represents the state variables in the small-signal model around the quiescent operating point given as $\begin{bmatrix} \omega_{ss} & \psi_{ss} & I_{ds} & I_{qs} & V_{ds} & V_{qs} & V_{ds-filt} & V_{qs-filt} & I_{dw} & I_{qw} \end{bmatrix}^T$. The small-signal input vector becomes $\hat{U} = \begin{bmatrix} \hat{T}_{load} & \hat{v}_{dw} & \hat{v}_{qw} \end{bmatrix}$. The final model is derived in the form

$$
\dot{\hat{X}} = A_L \hat{X} + B_L \hat{U} \tag{4.12}
$$

where the elements of the A_L and B_L matrices are given in (4.13) and (4.14), respectively. Considering that the objective is to suppress resonant oscillations in stator currents i_{ds} and i_{qs}, the transfer functions $\frac{\hat{i}_{ds}(s)}{\hat{v}_{dw}(s)}$ and $\frac{\hat{i}_{qs}(s)}{\hat{v}_{qw}(s)}$ can be derived by converting (4.12) into

$$A_L = \begin{bmatrix}
0 & K_t I_q & 0 & K_t \psi_{ss} & 0 & 0 & 0 & 0 & 0 & 0 \\
0 & -\frac{R_r}{L_r} & \frac{R_r L_m}{Lr} & 0 & 0 & 0 & 0 & 0 & 0 & 0 \\
n_p I_q & K_2 - \frac{K_3 I_q^2}{\psi_{ss}^2} & K_1 & n_p \omega_{ss} + 2\frac{I_q K_3}{\psi_{ss}} & \frac{1}{\sigma} & 0 & 0 & 0 & 0 & 0 \\
K_4 \psi_{ss} - n_p I_d & K_4 \omega_{ss} - \frac{K_5 I_d I_q}{\psi_{ss}^2} & \frac{K_5 I_q}{\psi_{ss}} - n_p \omega_{ss} & K_1 + \frac{K_5 I_d}{\psi_{ss}} & 0 & \frac{1}{\sigma} & 0 & 0 & 0 & 0 \\
n_p V_{qs} & -\frac{L_m V_{qs} I_q}{\tau_r \psi_{ss}^2} & -\frac{1}{C_f} & \frac{L_m V_{qs}}{\tau_r \psi_{ss}} & -\frac{1}{R_{d-m} C_f} & \omega_e & \frac{1}{R_{d-m} C_f} & 0 & \frac{1}{C_f} & 0 \\
-n_p V_{qs} & \frac{L_m V_{ds} I_q}{\tau_r \psi_{ss}^2} & 0 & -\frac{1}{C_f} - \frac{L_m V_{ds}}{\tau_r \psi_{ss}} & -\omega_e & -\frac{1}{R_{q-m} C_f} & 0 & \frac{1}{R_{q-m} C_f} & 0 & \frac{1}{C_f} \\
0 & 0 & 0 & 0 & 1 & 0 & -a & 0 & 0 & 0 \\
0 & 0 & 0 & 0 & 0 & 1 & 0 & -a & 0 & 0 \\
n_p I_{qw} & -\frac{L_m I_q I_{qw}}{\tau_r \psi_{ss}^2} & 0 & \frac{L_m I_{qw}}{\tau_r \psi_{ss}} & -\frac{1}{L_f} & 0 & 0 & 0 & 0 & \omega_e \\
-n_p I_{dw} & \frac{L_m I_{dw} I_q}{\tau_r \psi_{ss}^2} & 0 & -L_m I_{dw} & 0 & -\frac{1}{L_f} & 0 & 0 & -\omega_e & 0
\end{bmatrix} \tag{4.13}$$

the Laplace domain.

$$B_L = \begin{bmatrix} -\frac{1}{J} & 0 & 0 \\ 0 & 0 & 0 \\ 0 & 0 & 0 \\ 0 & 0 & 0 \\ 0 & 0 & 0 \\ 0 & 0 & 0 \\ 0 & 0 & 0 \\ 0 & 0 & 0 \\ 0 & \frac{1}{L_f} & 0 \\ 0 & 0 & \frac{1}{L_f} \end{bmatrix} \tag{4.14}$$

The constants in (4.13) and (4.14) are given below.

$$K_t = \frac{1.5 n_p L_m}{J L_r}, K_1 = \frac{L_m^2 R_r}{\sigma L_r^2} + \frac{R_s}{\sigma}, K_2 = \frac{L_m R_r}{\sigma L_r^2}, K_3 = \frac{L_m R_r}{L_r}, K_4 = \frac{L_m n_p}{\sigma L_r} \tag{4.15}$$

4.3 Active Damping Controller Design for FOC

The block diagram for a typical rotor FOC implementation with active damping control is shown in Figure 4.8. The sensed motor voltages are passed through the *abc-dq* transformation block, which converts only the fundamental components into dc quantities. The harmonics of the transformation output, which correspond to the resonant components, are extracted using a low-pass type filter. The resonant voltages are then used to generate damping current references.

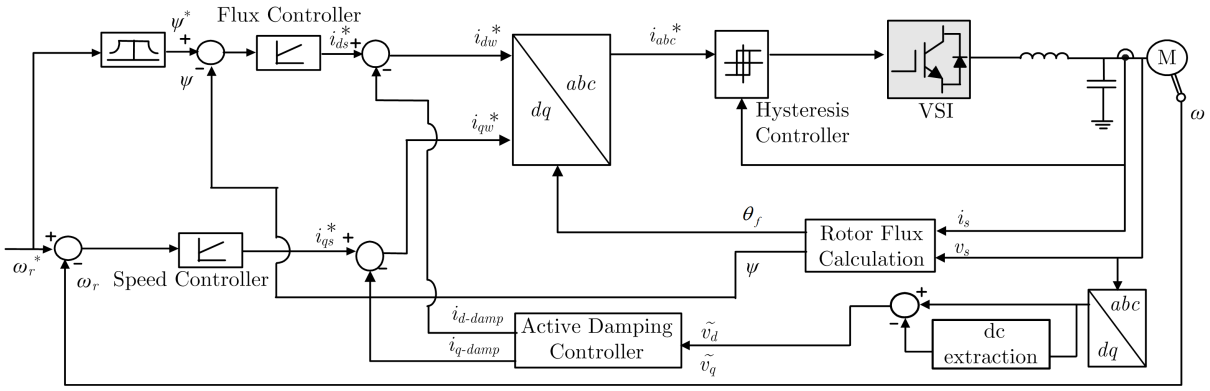

Figure 4.8: Rotor flux FOC implementation with active damping controller.

The emulated damping currents i_{d-damp} and i_{q-damp} flowing through the virtual resistors R_{d-m} and R_{q-m} are subtracted from the reference currents obtained from the flux and speed controllers [69, 90]. Under this control, the steady-state stator currents (i_{ds}) and (i_{qs}), at operating flux (ψ_{ss}) and load torque (T_{load}) reduce to the following equations:

$$I_{ds} = \frac{\psi_{ss}}{L_m}, \qquad I_{qs} = \frac{T_{load}}{\frac{3}{2}\left(n_p L_m / L_r\right)\psi_{ss}} \tag{4.16}$$

For indirect FOC, the steady-state slip frequency (ω_{slip}) can be derived as

$$\omega_{slip} = \frac{R_r L_m I_{qs}}{L_r \psi_{ss}} \tag{4.17}$$

which is then added to the rotor speed ω_r to compute the synchronous electrical frequency.

$$\omega_e = \omega_{slip} + n_p \omega_r \tag{4.18}$$

Steady-state values are substituted for the matrix elements in (4.13) and (4.14), which define the system state around the operating point.

4.4 Simulation Studies

A 3-ϕ, 5 hp induction motor drive with parameters given in Table 4.1 is used for sim-

ulation. The effect of changing the damping resistance values (R_{d-m}) and (R_{q-m}) in the transfer functions is analyzed. Desired frequency- and time-domain performance requirements are specified to determine appropriate resistance values. For example, gain and phase margins and settling time for stator current transfer functions may be considered. Setting $R_{d-m} = R_{q-m} = \infty$, the damping controller is not active initially in the control loop. The transfer functions $\frac{\widehat{i}_{ds}(s)}{\widehat{v}_{dw}(s)}$ and $\frac{\widehat{i}_{qs}(s)}{\widehat{v}_{qw}(s)}$, corresponding to the equivalent circuits in Figures 4.6b and 4.7, respectively, are evaluated at the operating condition given in Table 4.1. The actual numerical transfer functions for $R_{d-m} = R_{q-m} = \infty$ are given in (4.19) and (4.20).[1] The Bode plots of both transfer functions are shown in Figure 4.9. It can be observed that the closed-loop system is unstable due to negative margins. Therefore, virtual damping must be added for stability. The resistance value is varied over a wide range and the eigen value movement of system matrix A_L is observed in Figure 4.10. LC filter poles move towards the left when resistance is decreased, indicating increased stability.

[1]

$$\frac{\hat{i}_{ds}}{\hat{v}_{dw}} = \frac{\begin{array}{c}3.013\times10^{-12}s^9 + 3.725\times10^{-8}s^8 + 1.996\times10^{9}s^7 + 4.75\times10^{11}s^6 + 4.78\times10^{16}s^5 + \\ 9.572\times10^{18}s^4 + 1.513\times10^{20}s^3 + 6.298\times10^{20}s^2 + 6.217\times10^{20}s + 1.78\times10^{20}\end{array}}{\begin{array}{c}s^{10} + 465.3s^9 + 4.809\times10^{7}s^8 + 2.053\times10^{10}s^7 + 5.779\times10^{14}s^6 + 2.241\times10^{17}s^5 + \\ 3.214\times10^{19}s^4 + 1.126\times10^{21}s^3 + 2.575\times10^{21}s^2 + 1.933\times10^{21}s + 4.725\times10^{20}\end{array}} \tag{4.19}$$

$$\frac{\hat{i}_{qs}}{\hat{v}_{dw}} = \frac{\begin{array}{c}4.036\times10^{-12}s^9 - 1.192\times10^{-7}s^8 + 1.996\times10^{9}s^7 + 4.656\times10^{11}s^6 + 4.779\times10^{16}s^5 + \\ 9.346\times10^{18}s^4 + 3.467\times10^{19}s^3 + 2.692\times10^{19}s^2 + 2.002\times10^{18}s - 2.221\times10^{18}\end{array}}{\begin{array}{c}s^{10} + 465.3s^9 + 4.809\times10^{7}s^8 + 2.053\times10^{10}s^7 + 5.779\times10^{14}s^6 + 2.241\times10^{17}s^5 + \\ 3.214\times10^{19}s^4 + 1.126\times10^{21}s^3 + 2.575\times10^{21}s^2 + 1.933\times10^{21}s + 4.725\times10^{20}\end{array}} \tag{4.20}$$

Table 4.1: Drive Parameters for Simulation Studies

Induction motor	460 V, 3-ϕ, 2 hp, 60 Hz, 3450 rpm
Stator resistance (R_s), Leakage inductance (L_{ls})	1.2073 Ω, 4.083 mH
Rotor resistance (R'_r), Leakage inductance (L_{lr})	1.1275 Ω, 6.094 mH
Rotor flux saturation limit (λ_{sat})	1.1 Vs
Mutual inductance (L_m)	154.9 mH
Number of pole pairs (P)	1
Series inductance, Fixed shunt capacitance	2 mH, 25 μF
Steady-state operating point	$\psi_{ss} = 0.4$ Vs, $\omega_{ss} = 120$ rad/s
	$T_{load} = 0.5$ Nm

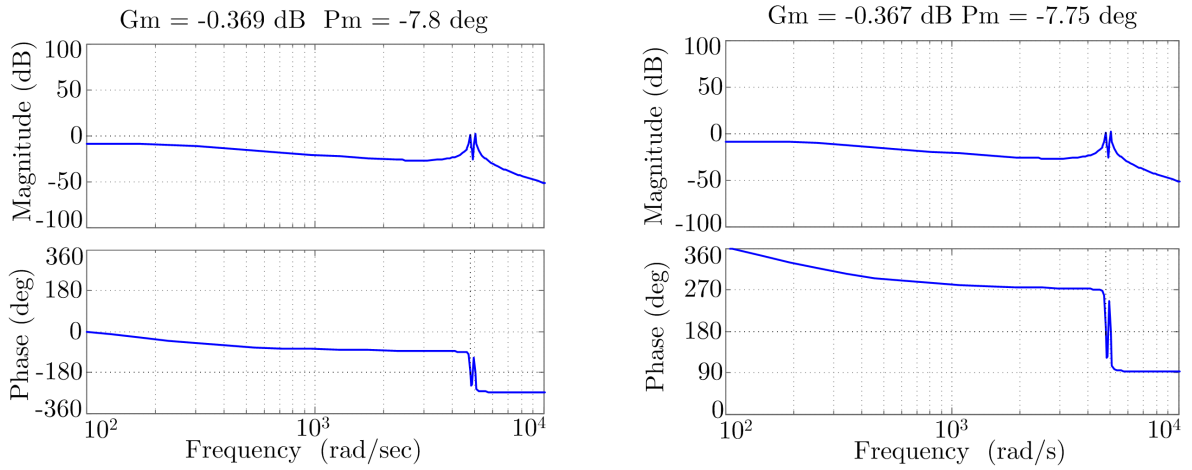

(a) (b)

Figure 4.9: Bode plots of transfer functions with $R_{d-m} = R_{q-m} = \infty$: (a) d-axis (b) q-axis.

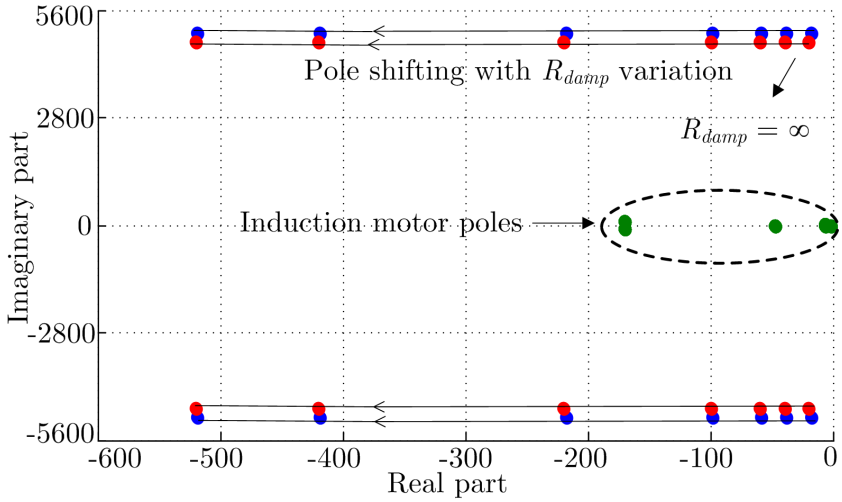

Figure 4.10: Eigen value movement with resistance variation.

A sample plot for R_{d-m}=R_{q-m}= 40 Ω is presented in Figure 4.11. The gain plot never crosses the 0 dB axis and shows a gain margin of 28.1 dB. The damping behavior in the low- and high-frequency range as the virtual resistance value is changed is shown in Figure 4.12, with an enlarged view. It can be observed that the gain and phase plots of the transfer function are not affected in the low-frequency range. The gain and phase at the fundamental frequency of 120 rad/s are found to be -8.93 dB and -11.4°, respectively. However, in the high-frequency range around the resonant frequency, the effect of resistance reduction can be clearly observed. The resonant peak magnitude is shown to be reduced by a factor of 15 (from 1.29 dB to -22.2 dB) as a result of damping. For example, to maintain a minimum gain margin of 15 dB in the d-axis transfer function, the value of R_{d-m} as a function of torque and rotor speed should not exceed the values shown in the surface plot in Figure 4.13. It is to be noted that the damping controller is designed in the time domain by varying the resistance value in the matrix given in (4.13) and interpreting the characteristics in the frequency domain for each of these trials. In the block diagram shown in Figure 4.8, the *dq-abc* transformation block is synchronized to the fundamental electrical frequency input at the machine terminals. This implies that any non-fundamental component of stator voltage is treated as an undesirable component

and subject to damping by the virtual resistance. Practical restrictions on sampling rates of three-phase stator voltages fed as inputs to the transformation block will limit the maximum frequency content in $\widetilde{v}_d$ and $\widetilde{v}_q$ that can be subject to damping.

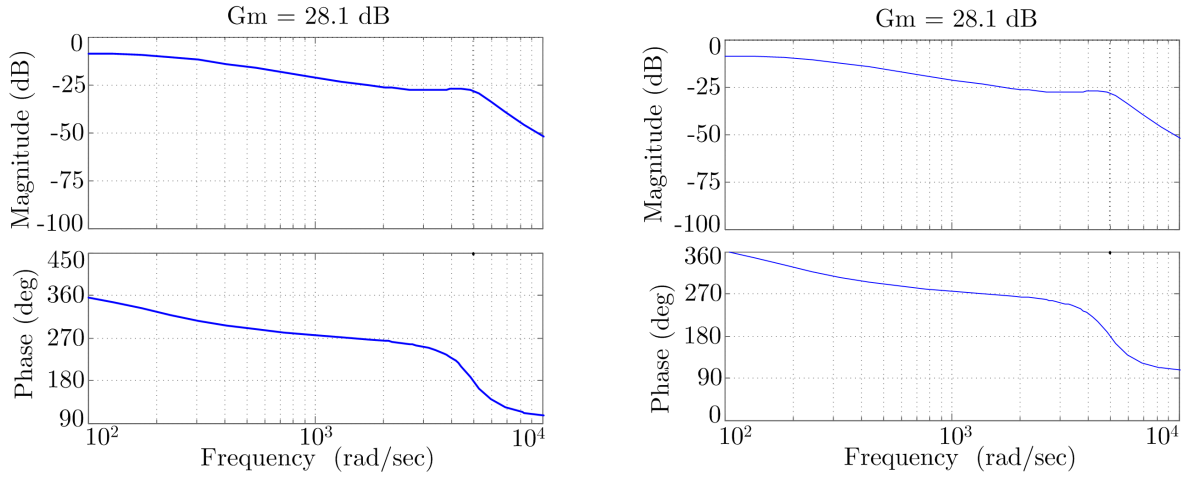

Figure 4.11: Bode plots of transfer functions with $R_{d-m} = R_{q-m} = 40\ \Omega$: (a) d-axis (b) q-axis.

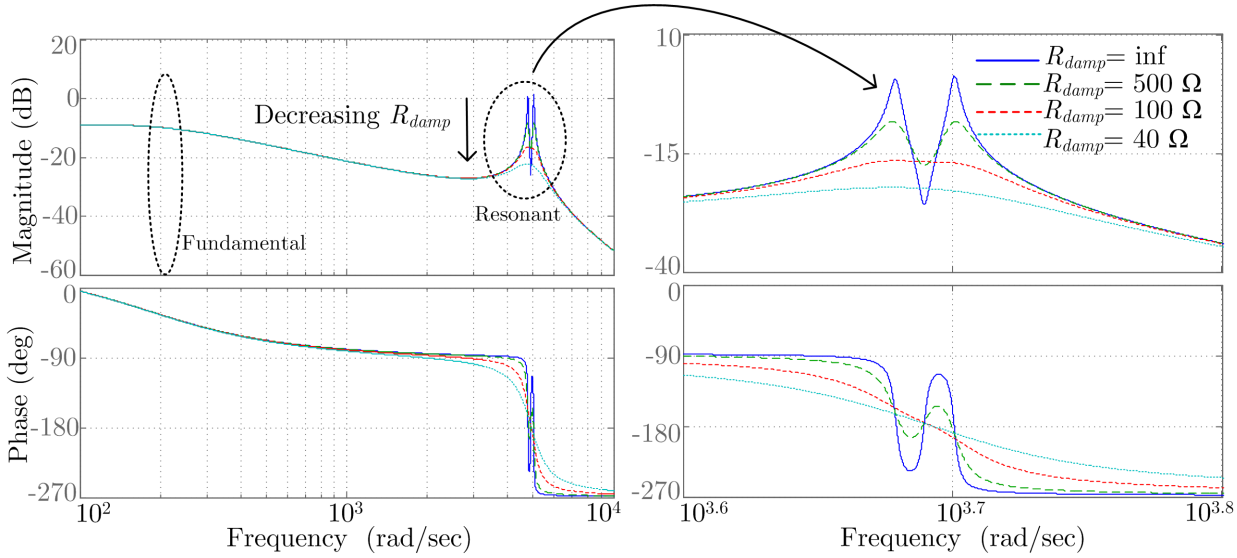

Figure 4.12: Damping behavior in the low- and high-frequency bands with change in resistance value.

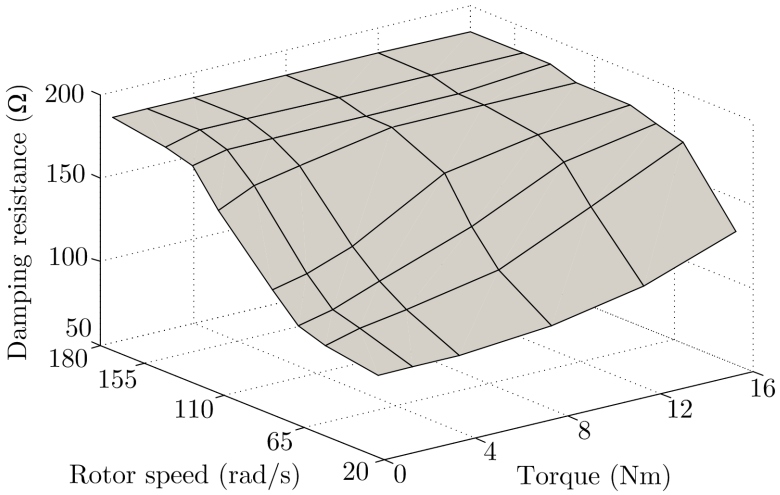

Figure 4.13: Resistance to maintain a minimum gain margin of 15 dB.

Differential damping is explored by varying resistances in both axes (R_{d-m}) and (R_{q-m}) independently over a sample range of 160 Ω to 1 Ω. The effects of resistance variation on the transfer function gain margins and settling time are presented as a surface plot in Figure 4.14. Although the gain margin values are completely decoupled, the settling times of stator currents in both axes are strongly influenced by R_{q-m}. As an example, a minimum gain and phase margin of 10 dB and 45° are specified for a reasonable trade-off between bandwidth and relative stability. From Figure 4.14, it can be seen that as R_{q-m} decreases, the settling time in the d-axis decreases, whereas it increases in the q-axis. In general, the torque loop will be subjected to more dynamics than the flux loop. Because the phase margin is requirement is already satisfied by using damping resistance, the values of R_{d-m} and R_{q-m} are chosen to meet the gain margin and settling time requirements. R_{d-m} can be fixed at 15 Ω and R_{q-m} at 25 Ω, using the plots in Figure 4.14. These values are adopted for a dynamic drive simulation with active damping enabled.

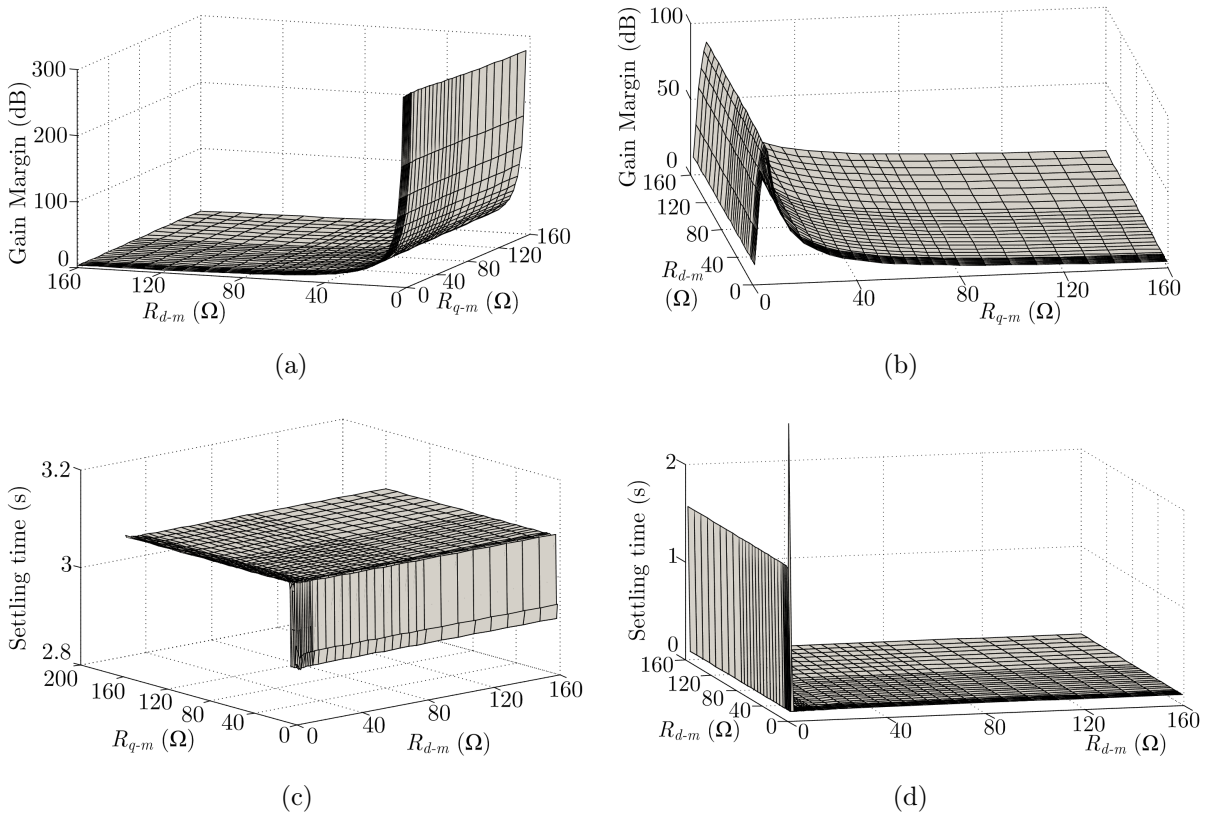

Figure 4.14: Gain margin in (a) d-axis (b) q-axis, settling time in (c) d-axis (d) q-axis.

Before damping, the motor voltage and current waveforms have undesirable resonant oscillations. When the damping controller is activated at 0.5 s with the determined resistance values, the oscillations in the voltages and current waveforms are effectively suppressed, as seen in Figures 4.15a and 4.15b, respectively. The speed and torque ripple are shown in Figures 4.15c and 4.15d, respectively.

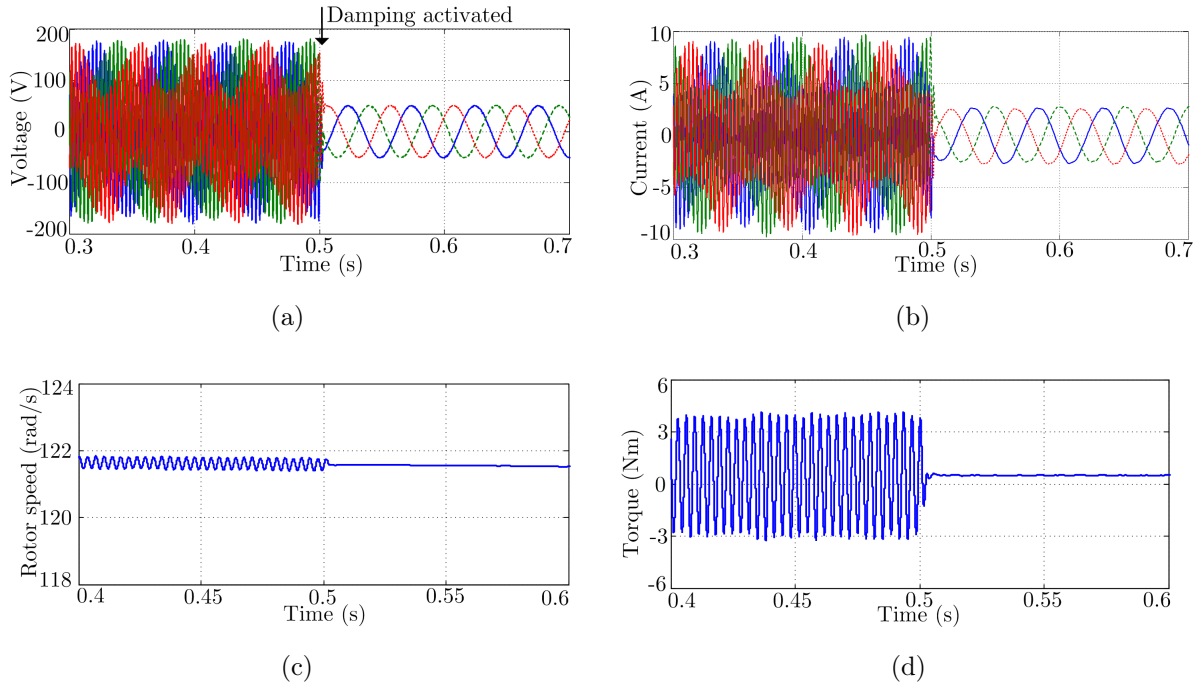

Figure 4.15: Before and after damping at 0.5 s: (a) three-phase *abc* stator voltages (b) three-phase stator currents (c) rotor speed (d) torque.

The THD in stator voltages and currents before and after damping is compared in Table 4.2, to show resonance cancellation. The *d*-*q* damping current references and voltages are shown in Figures 4.16a and 4.16b, respectively. The *d*-axis equivalent circuit is less-dependent on speed voltages. This can be ascertained from the gain margin variation at different values of rotor flux, shown in Figure 4.17. Here $R_{d-m} = R_{q-m} = 180\ \Omega$.

Table 4.2: Total Harmonic Distortion Comparison before and after Damping

	Phase	Voltage		Current	
		Before 0.5 s	After 0.5 s	Before 0.5 s	After 0.5 s
THD (%)	*a*	50.7	1.2	200.8	3.1
	b	51.7	1.0	160.6	4.5
	c	46.5	0.9	188.2	4.7

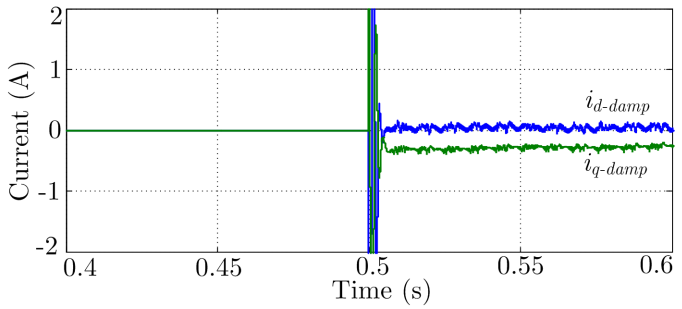

(a)

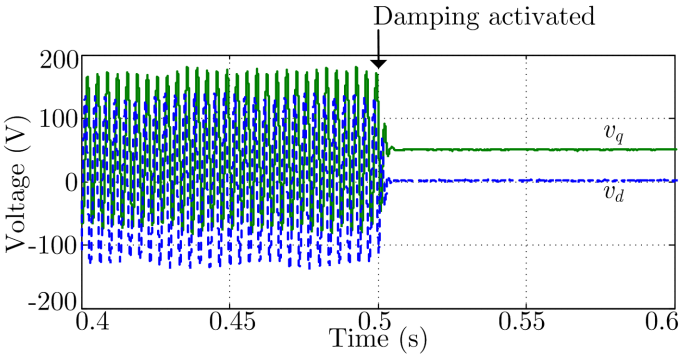

(b)

Figure 4.16: (a) Damping current references in d- and q-axes (b) d-q stator voltages.

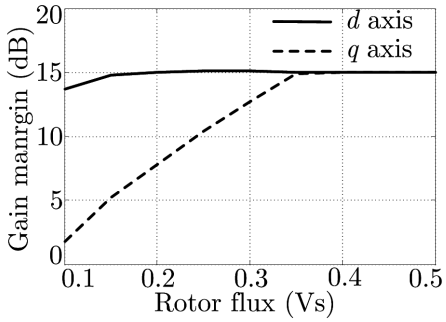

Figure 4.17: Gain margin variation with rotor flux.

4.4.1 Dynamic Tuning of the Controller

Virtual resistance values may need to be adjusted to meet drive performance specifications for dynamic operating conditions. The following example demonstrates a speed change from 120 rad/s to 157 rad/s. R_{d-m} is changed from 15 Ω to 30 Ω. R_{q-m} is changed

from 25 Ω to 40 Ω. The results are shown in Figure 4.18. The new speed is commanded at 0.5 s with a simultaneous update to the virtual resistance values. The transients observed in the voltage, current and torque waveforms result from the speed change. Using the updated resistance values, the damping operation continues after 0.5 s.

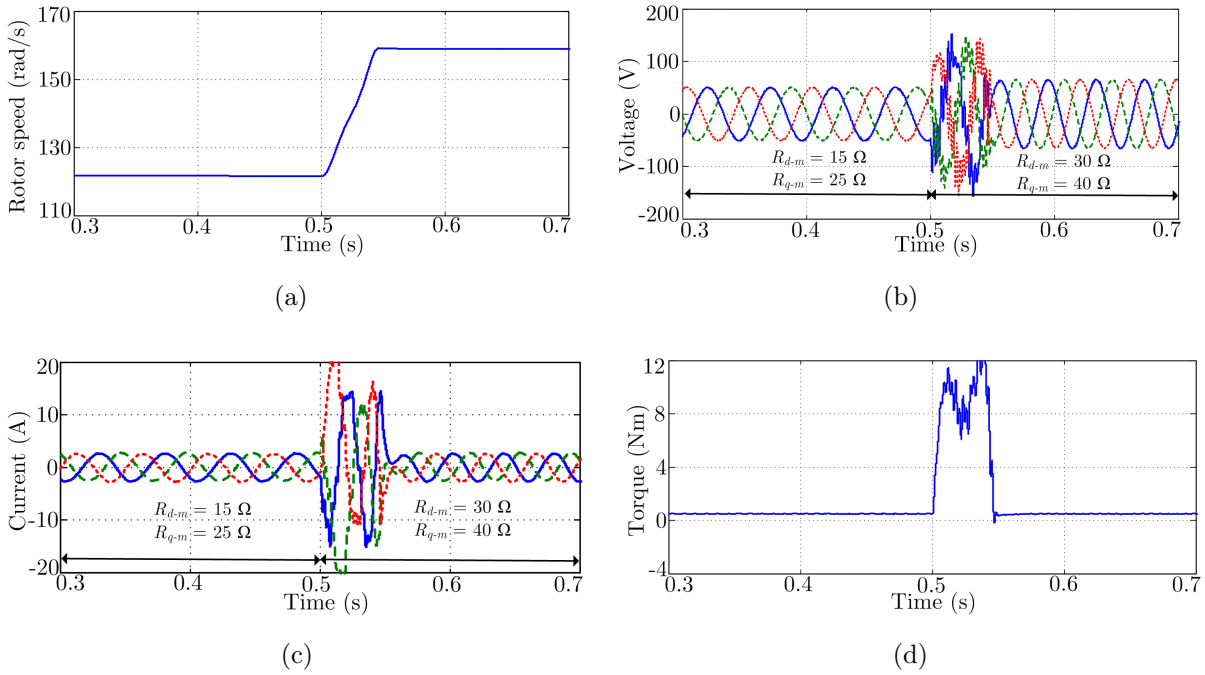

Figure 4.18: Updating virtual resistance value for change in speed command: (a) actual rotor speed (b) stator voltages (c) stator currents (d) torque.

4.5 Experimental Verification

Experimental investigations are carried out on a 2 hp induction motor drive with parameters given in Table 4.3. Using the procedure outlined in Section 4.4, the values of R_{d-m} and R_{q-m} are determined to be 15 Ω and 25 Ω, respectively, at the operating point considered. The experimental waveforms in Figure 4.19 indicate effective damping of resonant oscillations after the controller is activated. The frequency of resonant oscillations is calculated from the motor-filter equivalent circuit to be 332 Hz, which corresponds closely to that of oscillations observed in the motor voltage and current waveforms. Computa-

tional requirements restrict the sampling rate of the analog channels of the controller. This limits the maximum inverter switching frequency achievable in the inverter to about 3 kHz in the experimental studies.

Table 4.3: Experimental Drive Parameters

Induction motor	230 V, 3-ϕ, 2 hp, 60 Hz, 3450 rpm
Stator resistance (R_s), Leakage inductance (L_{ls})	1.2073 Ω, 4.083 mH
Rotor resistance (R'_r), Leakage inductance (L_{lr})	1.1275 Ω, 6.094 mH
Mutual inductance (L_m)	154.9 mH
Number of pole pairs (P)	1
Series inductance, Fixed shunt capacitance	10 mH, 25 μF
Steady-state operating point	$\psi_{ss} = 0.35$ Vs, $\omega_{ss} = 200$ rad/s
	$T_{load} = 0.5$ Nm
Virtual resistances	$R_{d-m} = 15\ \Omega$, $R_{q-m} = 25\ \Omega$

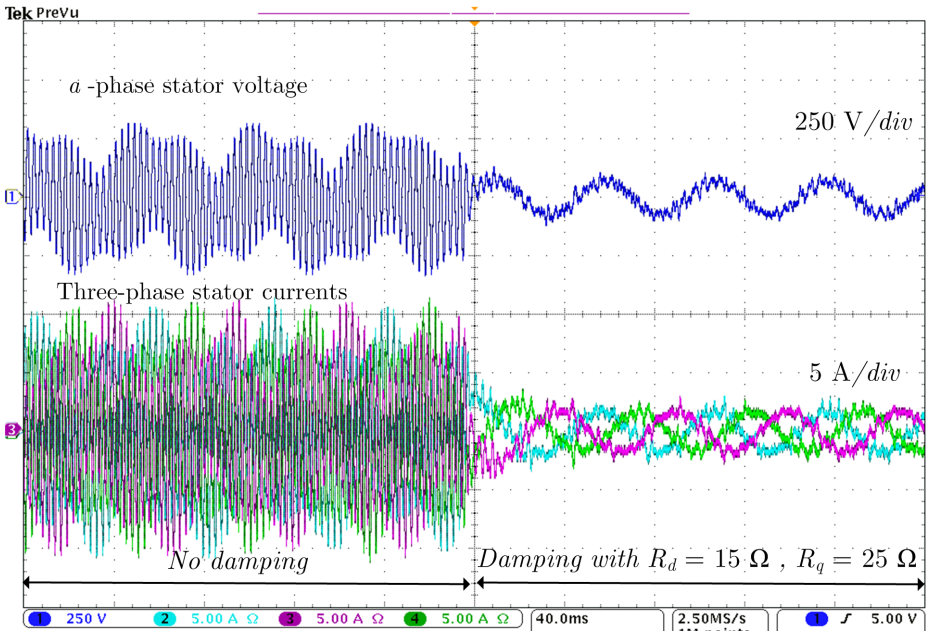

Figure 4.19: Motor stator voltage and current waveforms: Before and after damping at $T_{load} = 0.5$ Nm, $\omega_{ss} = 200$ rad/s, $\psi_{ss} = 0.35$ Vs.

4.6 Effect of Switching Frequency Limitation on Damping

The VSI must have a sufficient bandwidth to track currents in the resonant frequency range. The fundamental objective in active damping is to suppress resonance by injecting a set of currents opposite in phase to those causing oscillations. Limited controller bandwidth will restrict the inverter's maximum switching frequency, thereby reducing the damping performance. To simulate this condition, the current controller bandwidth is intentionally limited to 10 kHz. The motor voltage and current waveforms shown in Figure 4.20 correspond to the observations made in the experimental results.

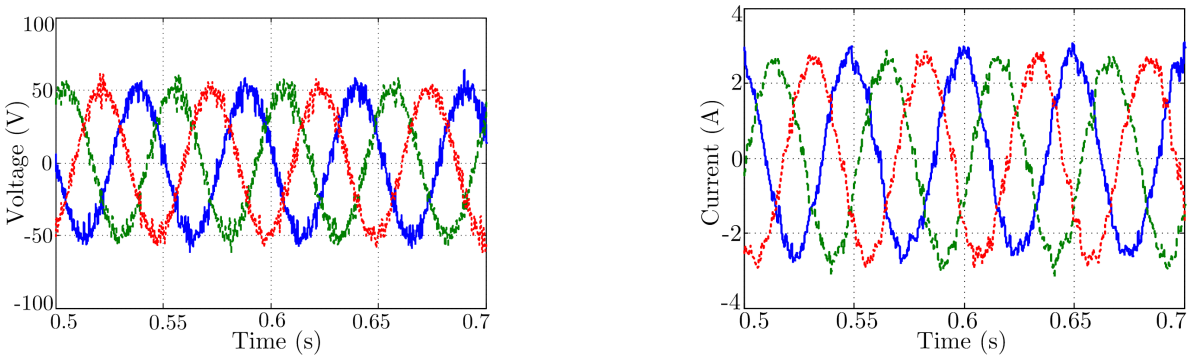

(a) (b)

Figure 4.20: Incomplete damping due to switching frequency limitation: (a) stator voltage (b) stator current.

4.7 Concluding Remarks

A small-signal transfer-function approach is proposed for selecting active damping resistance values to damp undesired resonant oscillations. Though virtual resistance techniques exist in the literature, the following improvements were proposed in this chapter.

- The virtual resistance value can be adjusted based on drive operating conditions instead of using fixed values.

- The controller design in a synchronous d-q reference frame provides the flexibility of differential damping, in which the resistances in the d- and q-axes need not be equal.
- The controller makes no use of explicit resonant frequency information.

The proposed method is useful in designing a damping controller for given frequency- and time-domain specifications. Simulation and experimental studies were carried out to demonstrate active damping in the motor-filter system.

Chapter 5

VARIABLE DC LINK VOLTAGE OPTIMIZATION

Dc link voltage optimization has been shown to result in increased motor drive efficiency [76]. The variable voltage is obtained by inserting a front-end, dc-dc converter between a fixed voltage dc bus and the inverter. Because inserting the additional front-end converter also contributes to loss, it is important to consider whether the variable dc link voltage is beneficial for all operating conditions. In this chapter, an objective function is formulated to derive the optimal dc link voltage for minimum power electronics loss in a converter-set. An algorithm is developed to derive a lower limit constraint on the optimal voltage command. Total losses for a wide range of rotor speed and torque conditions are evaluated to verify the benefits of the proposed scheme.

A front-end dc-dc buck converter added to a typical hex-bridge VSI motor drive is shown in Figure 5.1. The fixed-voltage dc input and variable voltage dc link are represented as V_{in} and $2V_{dc}$ (V_{dc} with respect to a midpoint), respectively. Section 5.1 describes the loss models used to formulate the objective function.

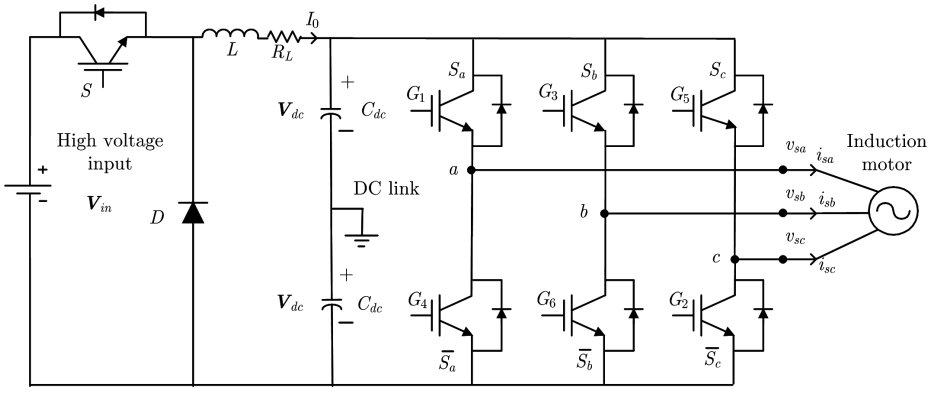

Figure 5.1: Three-phase VSI induction motor drive with front-end buck converter.

5.1 Converter and Inverter Loss Models

Losses in a power converter can be calculated using numerous methods [91,92]. Typical waveforms during hard turn-on and turn-off transitions are shown in Figure 5.2. Piecewise linearity is assumed for the shown voltage and current waveforms during the transient intervals. The approximations must be modified based on whether the loads are resistive, inductive or capacitive. The front-end, dc-dc buck converter and three-phase inverter illustrated in Figure 5.1 consist of insulated gate bipolar transistor (IGBT) semiconductor switches. Since the inverter operates in a hysteresis current control mode, its switching frequency varies [93]. An expression for switching frequency is derived in Section 5.1.2. The average switching frequency is required to estimate average switching losses in the inverter.

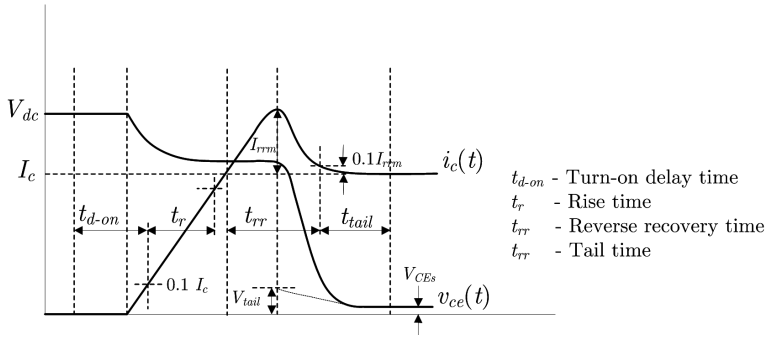

(a)

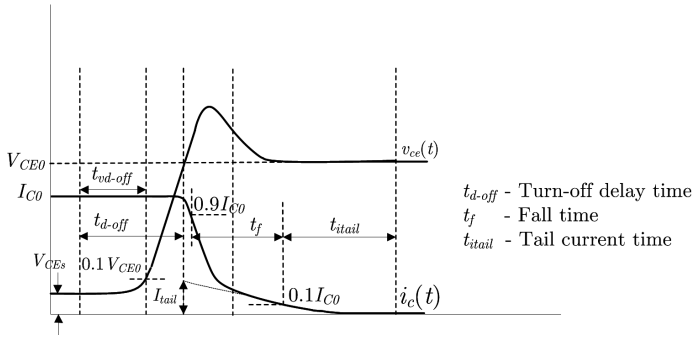

(b)

Figure 5.2: Transient waveforms for IGBT switching loss calculations during (a) turn-on transient (b) turn-off transient.

5.1.1 Front-End Buck Converter Losses

Conduction and switching losses in the switch S and diode D are derived as follows. Switch device on-states can be modeled as a forward voltage drop (V_{CEon}) in series with a resistance (R_{ce}). The conduction loss (P_{cond-s}) of the switch S is given as

$$P_{cond-s} = V_{CEon} I_{avg-s} + I_{rms}^2 R_{ce} \tag{5.1}$$

where I_{avg-s} and I_{rms-s} are, respectively, the average and rms value of currents flowing through the switch. Switching losses (P_{sw-s}) due to nonideal commutation during turn-on (t_{on}) and turn-off (t_{off}) intervals are directly proportional to switching frequency (f_{sw}). After computing the switch turn-on (E_{on}) and turn-off energy losses (E_{off}), the switching losses can be given by

$$P_{sw-s} = (E_{on} + E_{off})\, f_{sw} \tag{5.2}$$

The values of V_{CEon}, R_{ce} can be obtained from the device datasheet. E_{on-s} and E_{off-s} can be computed from the voltage-current transitions during the t_{on} and t_{off} intervals, respectively. The conduction (P_{cond-d}) and switching losses (P_{sw-d}) in the freewheeling diode (D) can be expressed similarly to (5.1) and (5.2) as

$$P_{cond-d} = V_{for} I_{avg-d} + I_{rms-d}^2 R_d \tag{5.3}$$

$$P_{sw-d} = (E_{on-d} + E_{off-d})\, f_{sw} \tag{5.4}$$

where V_{for} and R_d, respectively represent the diode forward-voltage drop and resistance. Assuming that the converter operates in continuous conduction mode (CCM), the average (I_{avg}) and rms (I_{rms}) expressions of the switch and diode currents can be found as

$$I_{avg-s} = I_0 D, I_{rms-s} = I_0 \sqrt{D} \tag{5.5}$$

and

$$I_{avg-d} = I_0 \left(1 - D\right), I_{rms-d} = I_0 \sqrt{(1 - D)} \tag{5.6}$$

In (5.5) and (5.6), D is the steady-state duty ratio and I_0 is the constant current output of the buck converter. The duty ratio for a constant current output I_0, including nonidealities can be derived as

$$D = \frac{V_{out} + V_{for} + I_0 R_{L-esr}}{V_{in} + V_{for} - V_{CEon}} \tag{5.7}$$

where V_{out} is the converter output voltage and R_{L-esr} is the equivalent series resistance of the inductor. From Figure 5.1 $V_{out} = 2V_{dc}$. The total losses ($P_{loss-buck}$) in the front-end converter can be written as

$$P_{loss-buck} = P_{cond-s} + P_{sw-s} + P_{cond-d} + P_{sw-d} \tag{5.8}$$

5.1.2 Three-Phase Inverter Losses

The conduction and switching losses in the IGBT switch and antiparallel diode in the inverter are similar to the expressions given in (5.1)-(5.4). However, the average and rms expressions for the inverter switch and diode currents are different [94] and can be derived as

$$I_{avg-s} = I_0 \left(\frac{1}{2\pi} + \frac{m_a \cos\phi}{8}\right), I_{rms-s} = I_0 \sqrt{\frac{1}{8} + \frac{m_a \cos\phi}{3\pi}} \tag{5.9}$$

$$I_{avg-d} = I_0 \left(\frac{1}{2\pi} - \frac{m_a \cos\phi}{8}\right), I_{rms-d} = I_0 \sqrt{\frac{1}{8} - \frac{m_a \cos\phi}{3\pi}} \tag{5.10}$$

In (5.9) and (5.10), m_a and ϕ represent the inverter modulation index and power factor angle, respectively. For any operating condition, the power factor angle can be directly computed from the steady-state induction motor equivalent circuit.

The switching frequency expression for a hysteresis-controlled VSI can be derived from the on and off durations in a switching period, within a hysteresis band h, as shown in Figure 5.3.

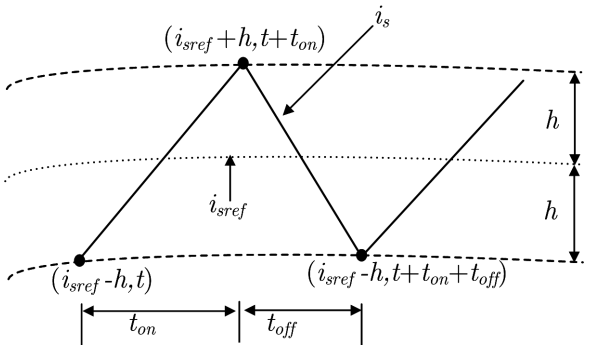

Figure 5.3: Current tracking in hysteresis control mode.

The on-time duration (T_{on}) can be derived as

$$T_{on} = \frac{2hL_s}{V_{dc} - V_{CEon} - I_s R_s - V_s \sin\theta} \tag{5.11}$$

where V_s and I_s represent the peak amplitude of stator phase voltage and current, respectively. L_s and θ represent the stator inductance and instantaneous angle, respectively, of the stator voltage waveform. The freewheeling off-time is given as

$$T_{off} = \frac{2hL_s}{V_{dc} + V_{for} + I_s R_s + V_s \sin\theta} \tag{5.12}$$

An instantaneous switching frequency expression can be computed using (5.11) and (5.12) as $(T_{on} + T_{off})^{-1}$. Integrating this expression over a fundamental stator votlage period, the average switching frequency can be derived as

$$f_{swavg} = \frac{2\left(V_{dc} + V_{for}\right)\left(V_{dc} - V_{CEon}\right) - V_s^2 - 2I_s^2R_s^2 - 2I_sR_s\left(V_{for} + V_{CEon}\right)}{4L_sh\left(2V_{dc} + V_{for} - V_{CEon}\right)} \tag{5.13}$$

The total inverter losses due to all switches shown in Figure 5.1, are given as

$$P_{loss-inv} = 6\left(P_{cond-s} + P_{sw-s} + P_{cond-d} + P_{sw-d}\right) \tag{5.14}$$

An objective function for total power electronics losses can be formulated by combining the losses in the front-end converter and the inverter as

$$P_{loss}^{total} = P_{loss-buck} + P_{loss-inv} \tag{5.15}$$

The goal is to minimize (5.15) by deriving the optimal dc link voltage command V_{dc}^*. The motor model and control equations corresponding to FOC implementation have already been discussed in Section 3.1. In Section 5.2, expressions are developed for stator currents, induced voltages and electrical frequency to formulate the link voltage lower limit.

5.2 Stator Voltage Estimation

For given flux (λ_r^*) and speed (ω_r^*) reference commands at a steady-state load torque (T_e^*), the reference stator current (i_s^*) can be derived using the FOC current equation (3.6) as

$$i_s^* = \sqrt{\left(\lambda_r^*/L_m\right)^2 + \left(T_e^*/\left(K_t\lambda_r^*\right)\right)^2} \tag{5.16}$$

The corresponding d- and q-axes stator flux references can be derived as

$$\lambda_{ds}^* = \sigma L_s i_{ds}^* + L_m\lambda_r^*/L_r \tag{5.17}$$

$$\lambda_{qs}^{*} = \sigma L_s i_{qs}^{*} \tag{5.18}$$

Substituting the stator flux references in (3.1), the steady-state induced stator voltages can be calculated as

$$v_{ds}^{*} = R_s i_{qs}^{*} - \omega_e^{*} \sigma L_s i_{qs}^{*} \tag{5.19}$$

$$v_{qs}^{*} = R_s i_{ds}^{*} + \omega_e^{*} \left(\sigma L_s i_{qs} + L_m \lambda_r^{*} / L_r\right) \tag{5.20}$$

For a given operating condition, the steady-state reference slip (ω_{slip}^{*}) , can be derived as

$$\omega_{slip}^{*} = \frac{R_r L_m i_{qs}^{*}}{L_r \lambda_r^{*}} \tag{5.21}$$

The slip frequency is then added to the rotor speed reference (ω_r^{*}) to compute the synchronous electrical frequency.

$$\omega_e^{*} = \omega_{slip}^{*} + n_p \omega_r^{*} \tag{5.22}$$

The induced stator voltage magnitude (v_s^{*}), can be given as

$$v_s^{*} = \left(v_{ds}^{*2} + v_{qs}^{*2}\right)^{1/2} \tag{5.23}$$

For effective tracking of the reference currents i_{ds}^{*} and i_{qs}^{*}, the dc link voltage V_{dc} has to be greater than at least v_s^{*}. Therefore, the objective function in (5.15) should be minimized, subject to the constraint $V_{dc} > v_s^{*}$. An offline grid search method is used to find the optimal link voltage value, which becomes the output voltage command for the buck converter. Figure 5.4 shows the overall block diagram of the closed-loop implementation for the variable link scheme.

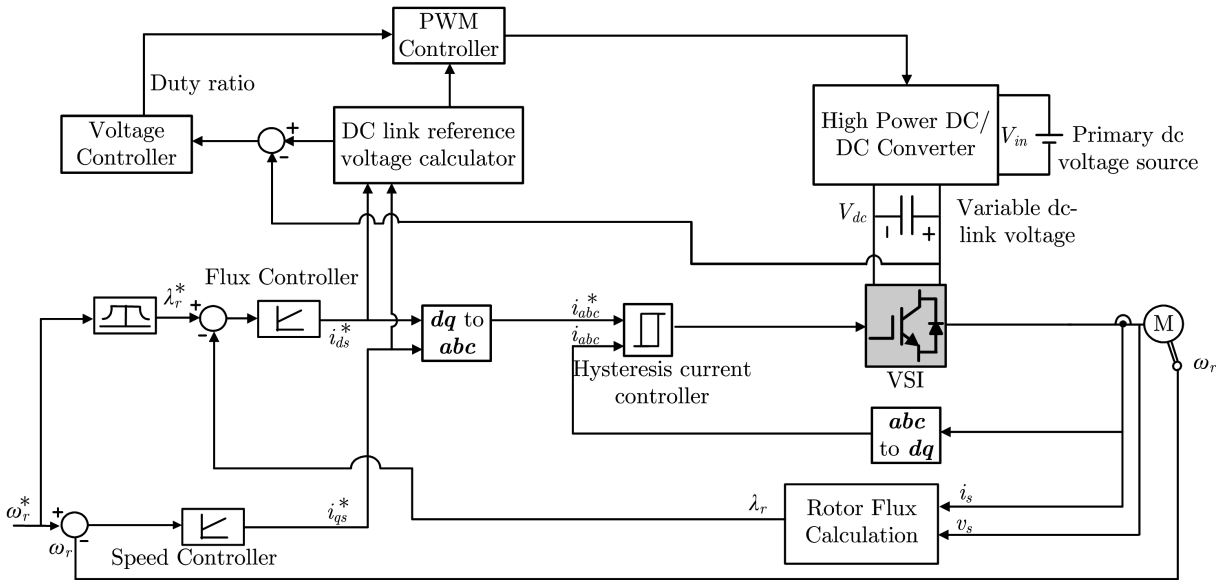

Figure 5.4: Rotor-flux FOC implementation in VSI with variable dc link front-end converter.

5.3 Simulation Studies

Both the fixed and variable link schemes are simulated on a 3-ϕ, 5 hp induction motor drive with parameters shown in Table 5.1. The front-end buck converter and the inverter are comprised of IGBT switches and diodes, whose parameters are also included in the table. Two different cases are considered. The first is simulated with the rated rotor flux command and the second with that optimum rotor flux command which results in minimum machine magnetic and copper loss [21, 27].

Table 5.1: Drive Parameters for Simulation Studies

Induction motor	460 V, 3-ϕ, 5 hp, 60 Hz, 1750 rpm
Stator resistance (R_s), Leakage inductance (L_{ls})	1.115 Ω, 5.974 mH
Rotor resistance (R'_r), Leakage inductance (L_{lr})	1.083 Ω, 5.974 mH
Rotor flux saturation limit (λ_{sat})	1 Vs
Mutual inductance (L_m)	203.7 mH
Number of pole pairs (P)	2
IGBT, diode voltage drop	V_{CEon}= 2.5 V, V_{for}= 3.4 V
On resistances in IGBT, diode	R_{ce}= 70 mΩ, R_d = 95 mΩ
Discrete diode voltage drop	V_{for}= 2.5 V
On resistance in discrete diode	R_{diode}= 45 mΩ
V_{in} (Front-end input)	1000 V
Hysteresis band ($2h$)	4 % of stator current amplitude
Buck converter switching frequency (f_{sw})	1 kHz

5.3.1 Rotor Flux at Rated Value

With rotor flux fixed at the rated value, the rotor speed and load torque are explored up to their rated values. The optimum value of the link voltage is shown as a surface plot in Figure 5.5a. As expected, the voltage command is strongly dependent on speed but not on torque. The modulation index for the inverter at each of these operating points is calculated and found to be uniformly close to unity, as shown in Figure 5.5b. In other words, optimum operation in this range adjusts the bus voltage for near-maximum modulation depth.

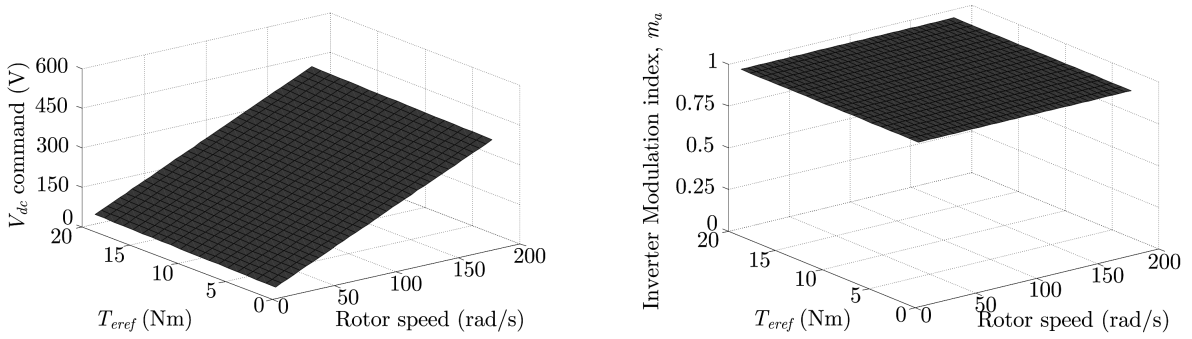

Figure 5.5: (a) DC link voltage command for different torque and rotor speed commands (b) corresponding inverter modulation index.

Power electronics losses and average switching frequencies are compared between the fixed and variable link systems and plotted with respect to speed and torque in Figure 5.6. The variable link voltage system is more beneficial at low-speed and torque ranges. At higher speeds, where dc bus utilization is inherently effective, the buck converter increases total loss, although marginally. This demonstrates that considerable energy savings should be possible in applications that involve large variation in operating speeds. A comparison of losses at different speed and torque conditions is shown in Table 5.2. The percentage loss reduction is shown in Figure 5.7. A marginal increase in losses can also be observed when the variable link scheme is operated close to rated conditions.

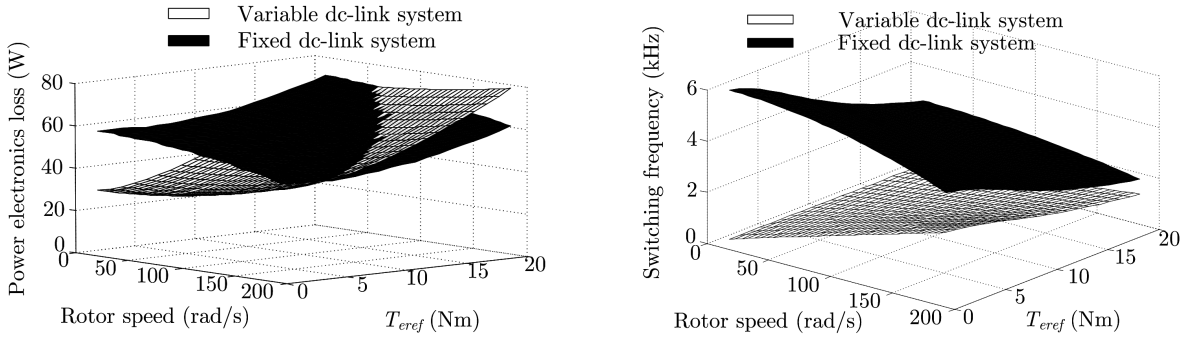

Figure 5.6: Comparison between the fixed and variable dc link schemes at rated rotor flux condition: (a) power electronics loss (b) average switching frequency.

Table 5.2: Power Electronics Loss Comparison: Simulation

Load torque	2 Nm		20 Nm	
Speed	Fixed-dc	Variable-dc	Fixed-dc	Variable-dc
60 rad/s	56 W	31 W	70 W	69 W
120 rad/s	52 W	35 W	66 W	73 W
180 rad/s	46 W	42 W	61 W	78 W

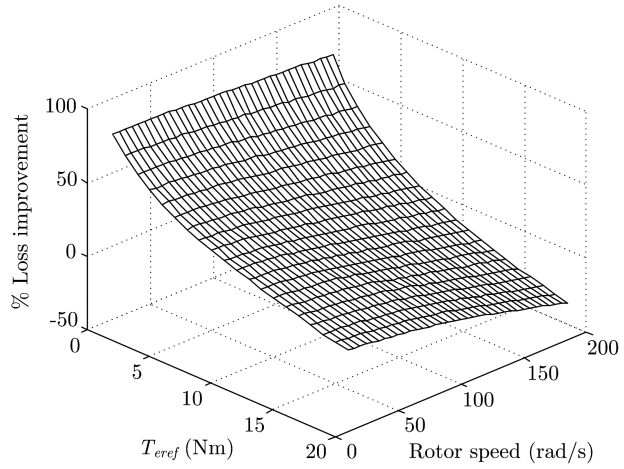

Figure 5.7: Percentage loss improvement in variable dc link over fixed dc link.

A dynamic simulation of the induction motor drive is performed in Simulink®, for varying speed references, at 900 rpm, 1300 rpm and 1700 rpm, with the load torque at $5\times10^{-4}\omega_r^2$ Nm. The dc link voltage reference is computed from the optimization procedure discussed in Section 5.2. Figure 5.8 illustrates closed-loop operation of the speed, torque and link voltage controllers.

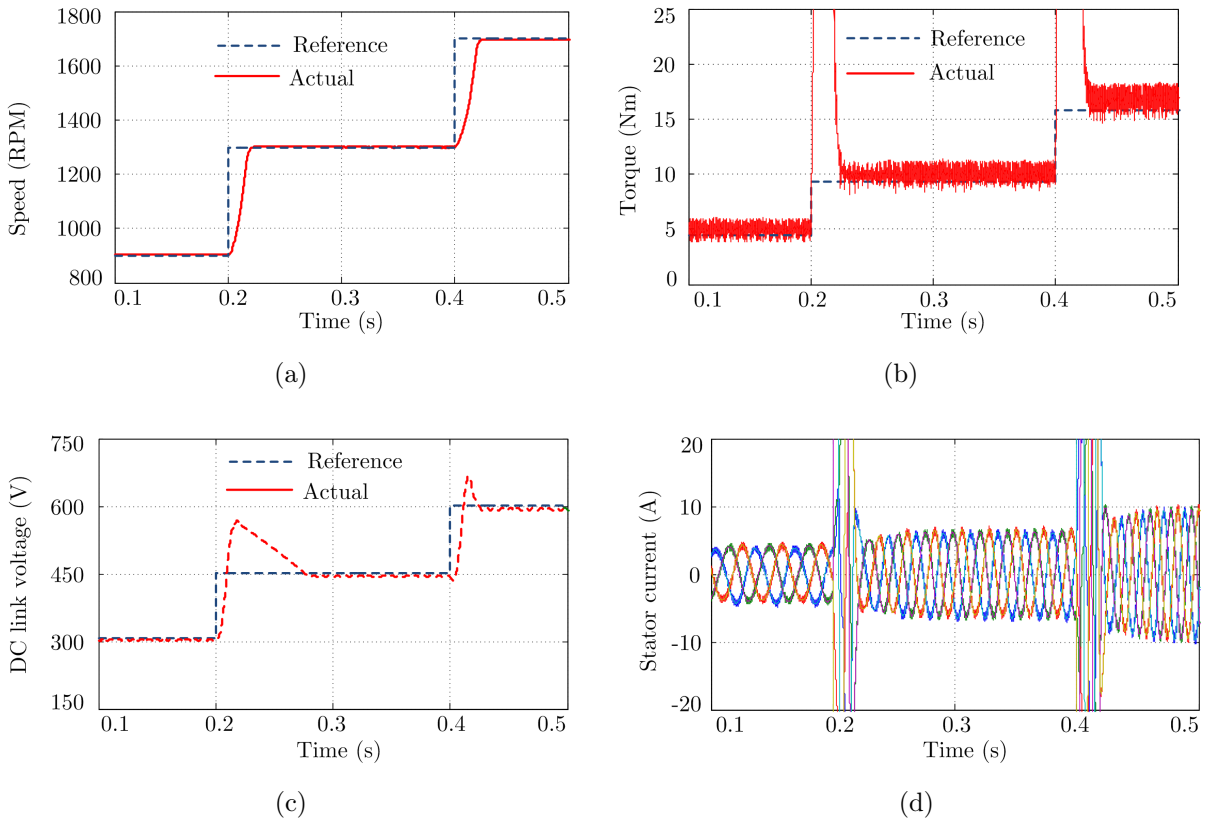

Figure 5.8: (a) Dynamic implementation in simulation: Actual and reference waveforms of (a) rotor speed (b) load torque (c) dc link voltage (d) stator currents.

5.3.2 Rotor Flux at Optimum Value

The dc link voltage reference can be further reduced by using the optimum flux command instead of rated flux. The optimum rotor flux command which gives the minimum machine copper and magnetic losses, and the dc link voltage command, are shown in Figure 5.9. The power electronics loss and average switching frequency, as a function of speed and torque, are shown in Figure 5.10.

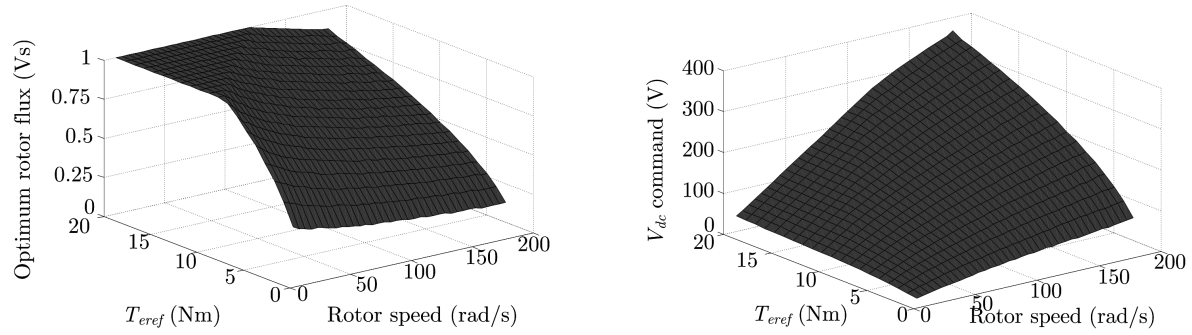

(a) (b)

Figure 5.9: (a) Optimum rotor flux command derived for different operating points (b) corresponding dc link voltage command.

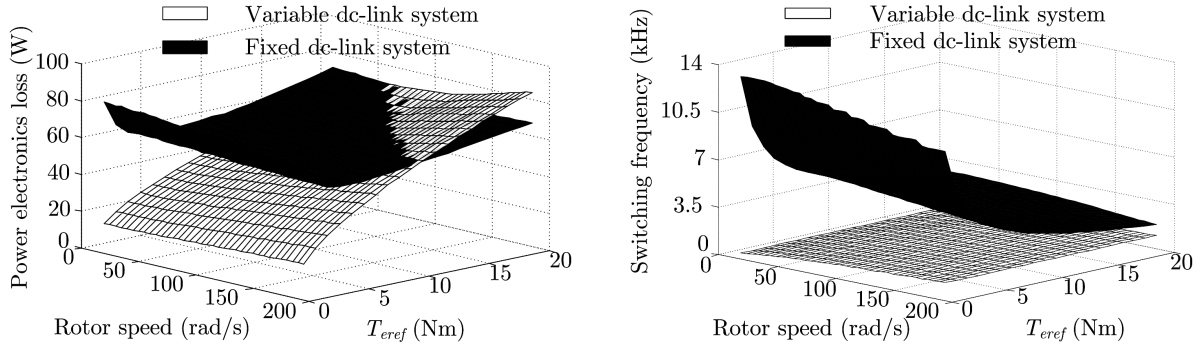

(a) (b)

Figure 5.10: Comparison between the fixed and variable dc link schemes at optimum rotor flux condition: (a) power electronics loss (b) average switching frequency.

5.3.3 Drive Cycle Case Study

A sample drive cycle with both acceleration and deceleration characteristics, is used to implement a dynamically varying dc link. The rotor flux and load torque are maintained constant at 1 Vs and 15 Nm, respectively, throughout the drive cycle. The buck converter is operated at a switching frequency of 2 kHz. The actual rotor speed follows the reference speed command, as shown in Figure 5.11. The primary dc supply voltage is 700 V. Corresponding dc link voltage reference is computed using the optimization procedure discussed in Section 5.2. The actual and reference dc link voltages are shown Figure 5.12.

Overall drive losses are compared in Table 5.3.

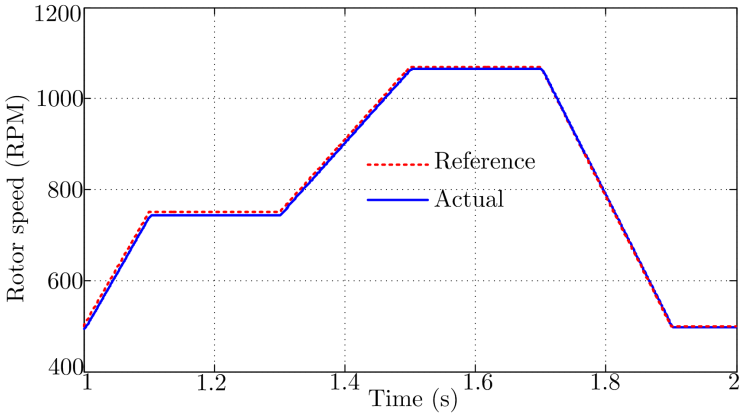

Figure 5.11: Sample drive cycle used in simulation.

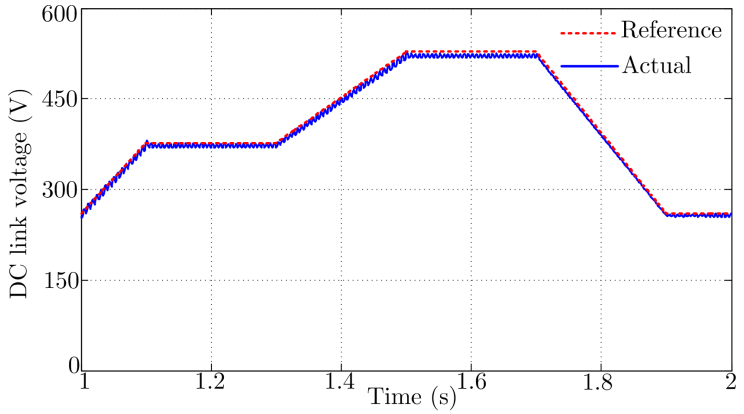

Figure 5.12: Reference and actual dc link voltage in the drive cycle.

Table 5.3: Drive Cycle Energy Efficiency (η) Comparison

Load torque	15 Nm		15 Nm	
Speed	Fixed dc		Variable dc	
	Net loss (W)	η (%)	Net loss (W)	η (%)
Drive cycle (V_{dc} = 600 V)	893	60.0	619	68.1
60 rad/s (V_{dc} = 600 V)	914	53.0	513	64.1
120 rad/s (V_{dc} = 600 V)	779	70.7	728	72.2
150 rad/s (V_{dc} = 700 V)	954	71.3	944	71.6

5.4 Experimental Verification

Experimental investigations are carried out on a 2 hp induction motor drive with details shown in Table 5.4. A summary of total losses in both the fixed and variable link schemes is shown in Table 5.5, with the loss surface plot in Figure 5.13a. Loss reduction of about 20% is observed under low-power operating conditions. A dynamic implementation of the variable link voltage scheme is demonstrated on an FOC motor drive to verify closed-loop operation of the flux, torque and link voltage controllers. Simulations are repeated using the experimental parameters shown in Table 5.4. Corresponding results of loss comparison are tabulated in Table 5.6 and shown as a surface plot in Figure 5.13b. It can be seen that both experiment and simulation results show identical trends of loss improvement. However, the actual loss magnitudes are different, as observed in Figure 5.14. This variation, which can be attributed to differences in actual and computed switching frequency (due to hysteresis band violations) and other unmodeled losses in the system, is observed to be uniform and hence does not significantly affect optimal operating points. Figure 5.15 shows experimental results for the load torque fixed at 0.1 Nm using the dynamometer controller. When the rotor speed command is changed from 160 rad/s to 90 rad/s, the duty ratio of the converter changes correspondingly to track the reference voltage. The inductor current in the dc-dc converter is also shown, indicating CCM operation. The closed-loop current controller operation can be verified from the three-phase stator currents shown in Figure 5.16.

Table 5.4: Drive Parameters for Experimental Studies

Induction motor	230 V, 3-ϕ, 2 hp, 60 Hz, 3450 rpm
Stator resistance (R_s), Leakage inductance (L_{ls})	1.2073 Ω, 4.083 mH
Rotor resistance (R'_r), Leakage inductance (L_{lr})	1.1275 Ω, 6.094 mH
Rotor flux saturation limit (λ_{sat})	0.5 Vs
Mutual inductance (L_m)	154.9 mH
Number of pole pairs (P)	1
IGBT, diode voltage drop	V_{CEon}= 2.45 V, V_{for}= 1.6 V
On resistances in IGBT, diode	R_{ce}= 7.5 mΩ, R_d = 8 mΩ
Rise time, Fall time	t_r =11 ns, t_f = 30 ns
V_{in} (Front-end input)	400 V
Hysteresis band ($2h$)	4 % of stator current amplitude
Buck converter switching frequency (f_{sw})	2 kHz

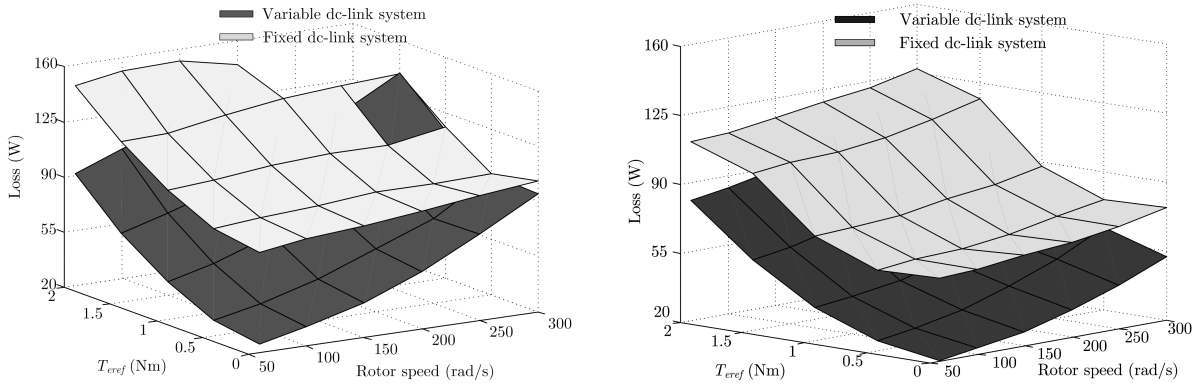

(a) (b)

Figure 5.13: Loss comparison between the fixed and variable dc link schemes: (a) Experiment (b) Simulation.

Table 5.5: Total Loss (in W) Comparison: Experiment

Load torque	0.1 Nm		0.5 Nm		1 Nm		1.5 Nm		2 Nm	
Speed	Fixed	Variable	Fixed	Variable	Fixed	Variable	Fixed	Variable	Fixed	Variable
60 rad/s	84	26	88	30	102	44	122	64	147	91
100 rad/s	88	32	91	36	104	51	123	72	152	102
150 rad/s	91	42	93	47	108	63	129	84	153	115
200 rad/s	95	57	96	60	110	76	134	104	145	127
250 rad/s	99	75	96	74	110	93	137	119		
300 rad/s	103	95	97	96	116	113				

Table 5.6: Total Loss (in W) Comparison: Simulation

Load torque	0.1 Nm		0.5 Nm		1 Nm		1.5 Nm		2 Nm	
Speed	Fixed	Variable	Fixed	Variable	Fixed	Variable	Fixed	Variable	Fixed	Variable
60 rad/s	62	20	61	25	73	37	100	56	111	81
100 rad/s	63	23	63	28	74	39	102	59	112	84
150 rad/s	66	27	64	33	76	45	103	65	115	89
200 rad/s	68	34	67	41	80	51	106	73	119	97
250 rad/s	72	42	72	50	83	61	111	82	122	106
300 rad/s	77	52	76	62	88	71	117	94	127	117

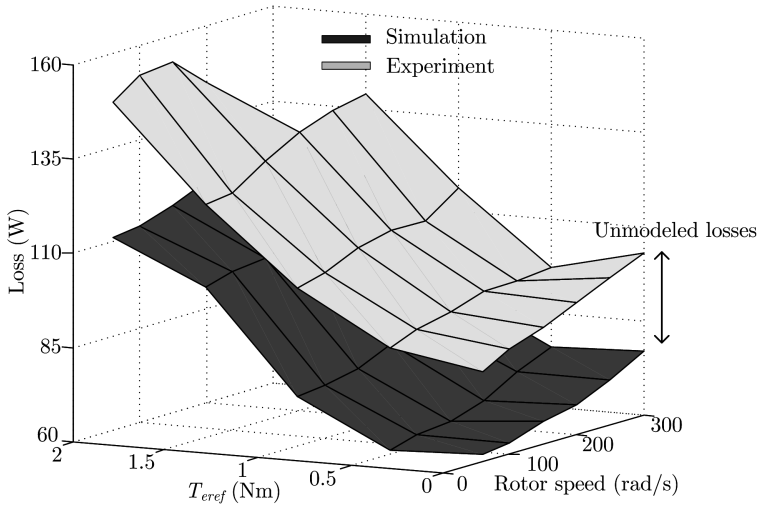

Figure 5.14: Comparison of losses between simulation and experimental results.

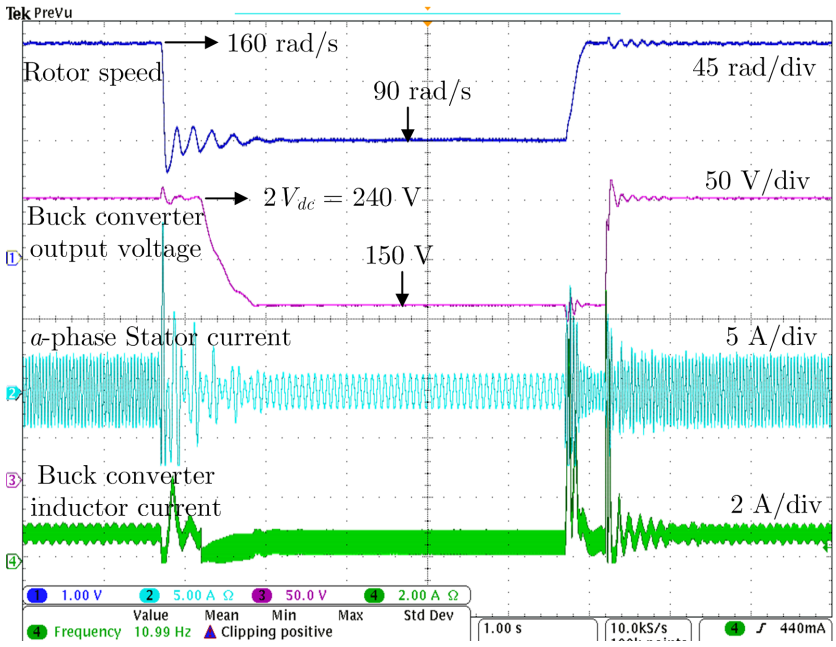

Figure 5.15: Dynamic implementation of variable link voltage scheme for varying speed conditions.

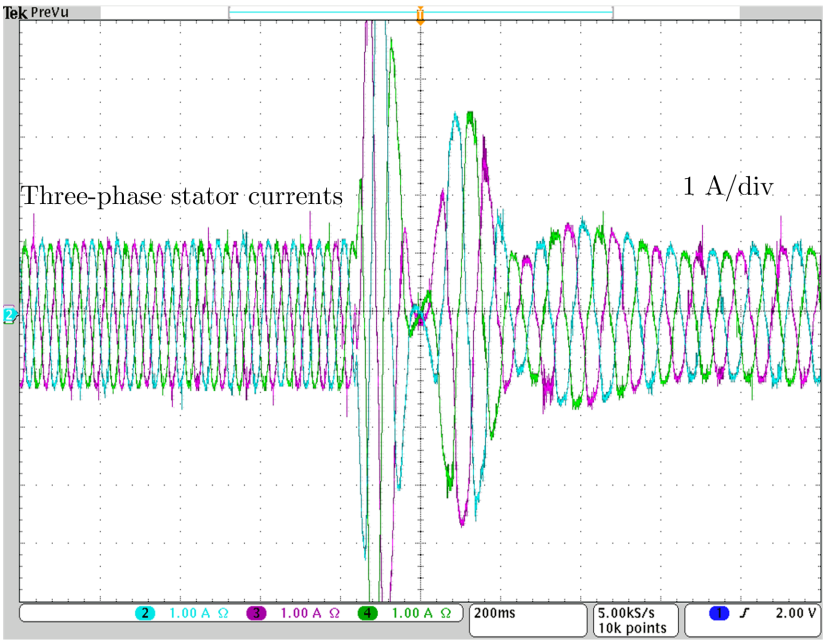

Figure 5.16: Stator currents during a speed change from 100 rad/s to 60 rad/s.

5.5 Concluding Remarks

A variable dc link scheme for a closed-loop induction motor drive is developed. The variable voltage is obtained by using a front-end buck converter between the fixed high-voltage dc bus and the inverter. The dc link voltage is chosen such that power electronics losses are minimized. The proposed method is demonstrated for the rotor FOC-based motor drive. It can be inferred that the variable dc link scheme is more beneficial for loss reduction at the low-speed range; it marginally increases the overall loss around rated speed conditions, where the dc-link utilization of the fixed-voltage dc bus is inherently effective. The fixed and variable link schemes are compared at both the rated and optimum rotor flux conditions. It is found that, when compared to the losses at the rated flux, the losses increase for the fixed voltage and decrease for the variable voltage at optimum flux. Simulation and experimental studies confirm that the loss reduction is significant at low speeds. This implies considerable energy savings in applications subject to wide speed variations.

Chapter 6

CONCLUSIONS AND FUTURE WORK

This dissertation has presented various opportunities and approaches for system-level loss minimization in induction motor drives. The work is motivated by past work on loss minimization carried out at the component level. This research proves that a system-level loss optimization is more beneficial than component-based methods. It is seen from simulation and experimental results that energy savings in a system-level optimization is more than the machine-based optimization by about 7% for operation under rated conditions. It is found that as the nonidealities become more pronounced in various components, system-level optimization offers increased potential for energy savings.

Several potential research topics and extensions emerge from this work. Though the constrained optimization approach has been shown for the rotor-flux oriented induction machine drive, it is possible to extend the optimization to methods, such as direct torque control (DTC), stator-flux oriented control, etc. It would be interesting to compare optimization results for FOC and DTC techniques under parametric variations, since the former method is more sensitive to machine parameters than the latter. Different drive cycles can be considered to estimate energy savings for practical road conditions. This will contribute to a better understanding of which cycles benefit from system minimization.

Performance of an induction machine drive is directly related to the quality of the machine stator voltage and current waveforms. Detailed discussion was carried out on induction machine-filter resonance which results in large oscillations and a subsequent increase in harmonic distortion. This work adopted a lossless active damping technique

to damp these oscillations. Results have shown that effective damping can be achieved by appropriate choice of resistance values. By introducing a differential damping approach using different values of damping resistance in the d-and q-axes, it has been demonstrated that the decoupled characteristics due to FOC are preserved in both axes. Desired dynamic behavior can be obtained by choosing resistance values determined using time- and frequency-domain analysis on the transfer functions of interest. Harmonic distortion in both current and voltage waveforms has been reduced to less than 5%. It is found that switching frequency limitations can negatively impact damping quality. Dynamic tuning of resistance values has been demonstrated for varying drive operating conditions.

Variation of link voltage for the inverter dc bus was shown to reduce losses in the inverter and increase the overall drive efficiency. Though this scheme would require a front-end converter to dynamically vary the voltage based on operating conditions, losses were reduced in most of the operating range, except around rated conditions, where the dc bus is already well utilized. Maximum energy savings are seen in the low-speed, low-torque range. Addition of the front-end converter can inhibit the machine's response to fast changing transients such as those observed in city driving cycles. Instantaneous variation of link voltage for such conditions may not be feasible. Averaging methods can be explored to find the optimum voltage that can be used for the drive cycle's entire duration.

6.1 Future Work

Several possible research topics in the areas of system-loss minimization, resonance suppression and variable link scheme are explored next. In the constrained optimization approach proposed in Chapter 3, thermal aspects associated with loss minimization have not been considered. Thermal ratings of the drive components can be incorporated into

the loss function by appropriately scaling the loss components. It is possible to include corresponding thermal constraints. This will help to redistribute heat in the system according to the thermal capacities of the components. Machine parameters have been assumed to be constant over time. However, parameters such as the rotor and stator resistances are known to vary with operating temperatures. It will be useful to investigate the drive loss sensitivity to parameter variations and generate a family of optimum control variable curves for different temperatures.

The active damping controller in Chapter 4 typically uses a low-pass or moving-average filter type, to isolate the resonant voltage components from the stator voltage waveform. Although necessary, such filters can inhibit the dynamic characteristics of the damping controller. Virtual resistance can be coupled with virtual inductance and/or capacitance to improve controller dynamics. Essentially, such a controller would be functionally equivalent to compensator (lead or lag) studied in the control literature. Another aspect to investigate would be the location of the damping resistance. In the current-controlled VSI drive demonstrated, the virtual resistance is placed across the shunt filter capacitor, which enables easier generation of damping current references. Series and parallel configurations of the virtual resistance can be studied. Series resistance is expected to provide effective damping in a voltage-controlled VSI.

The variable dc link scheme has been implemented with a buck-type dc-dc converter. Different topologies of bidirectional dc-dc and ac-dc converters can be studied to ascertain efficiency improvements. The algorithm developed to determine the optimal link voltage in this dissertation is specific to FOC, which is a vector control method. It would be interesting to compare the optimal voltage command for scalar control methods, such as the volts-per-hertz control. Since no inherent decoupling is achieved in the scalar control, the optimal voltage command is expected to be higher than that for vector control. Possible future work outlined above has the potential to provide a more comprehensive and realistic approach to induction machine drive loss minimization.

Appendix A

HARDWARE PROTOTYPES

This appendix provides the photographs, printed circuit board layouts and schematics of various circuits developed in the laboratory.

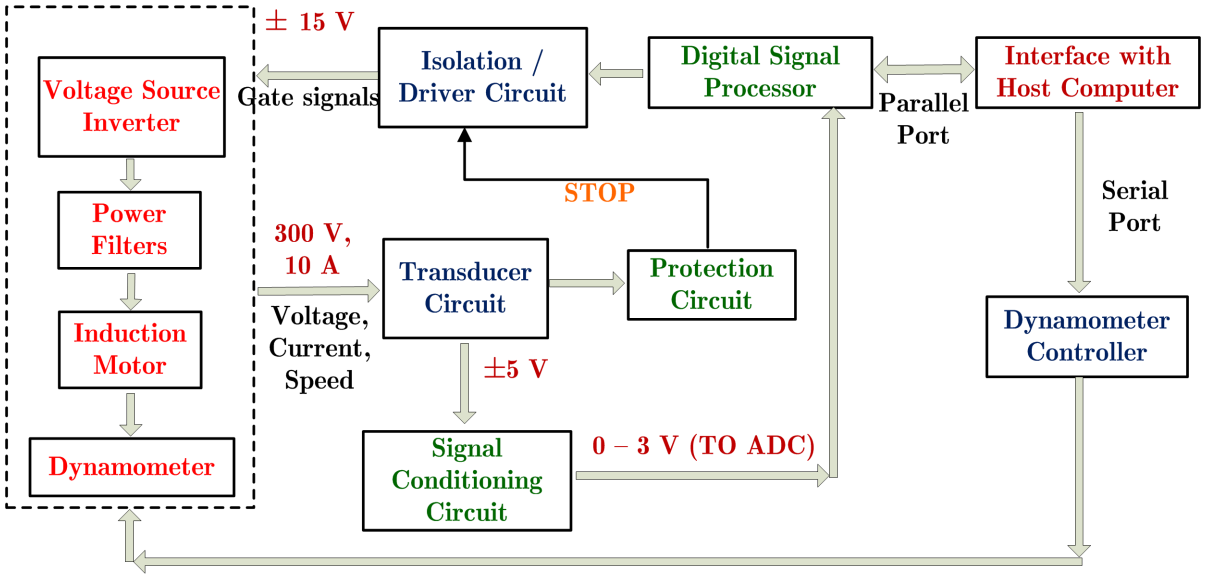

Figure A.1: Schematic block diagram of the setup.

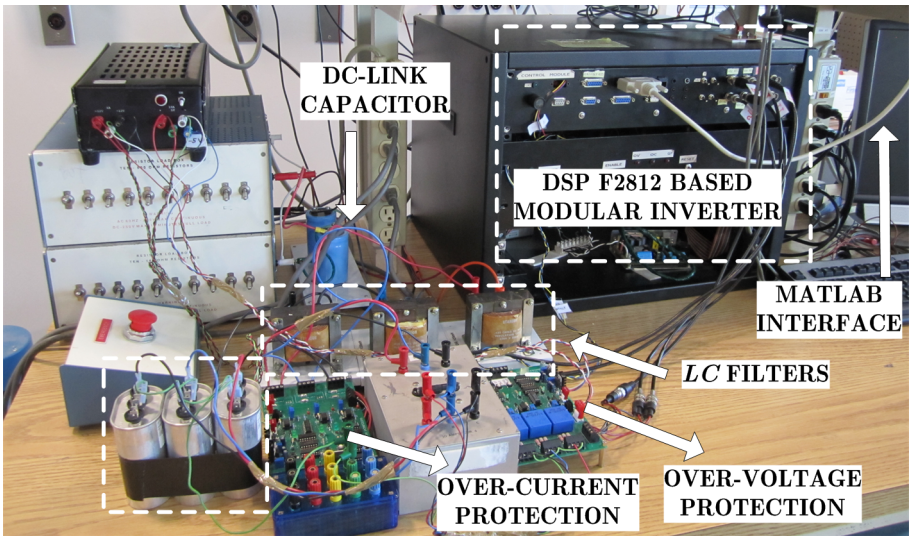

Figure A.2: Photograph of the experimental setup.

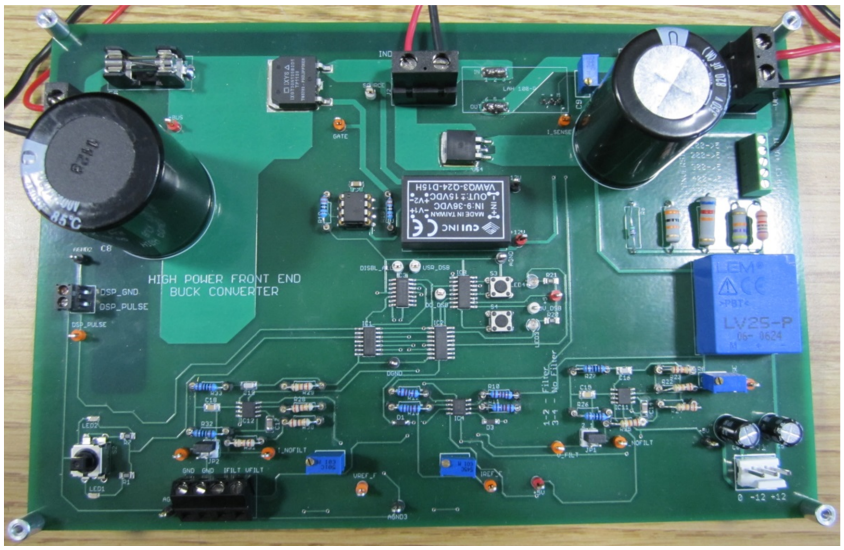

Figure A.3: Photograph of the front-end converter.

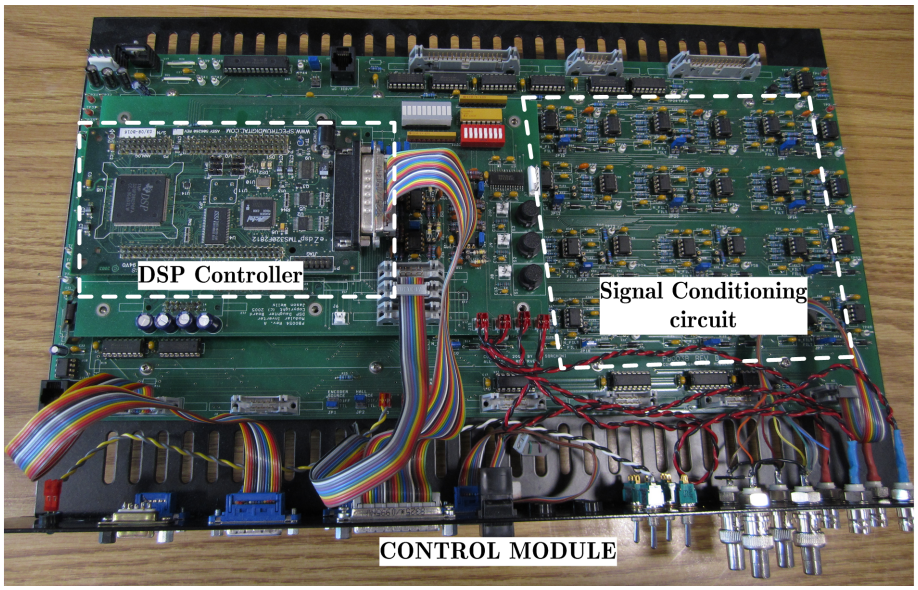

Figure A.4: Photograph of the control module.

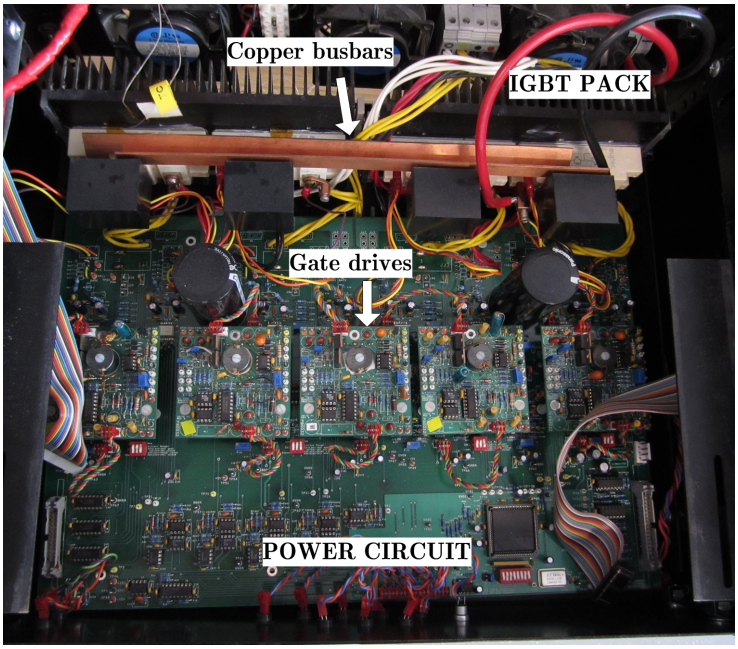

Figure A.5: Photograph of the power module.

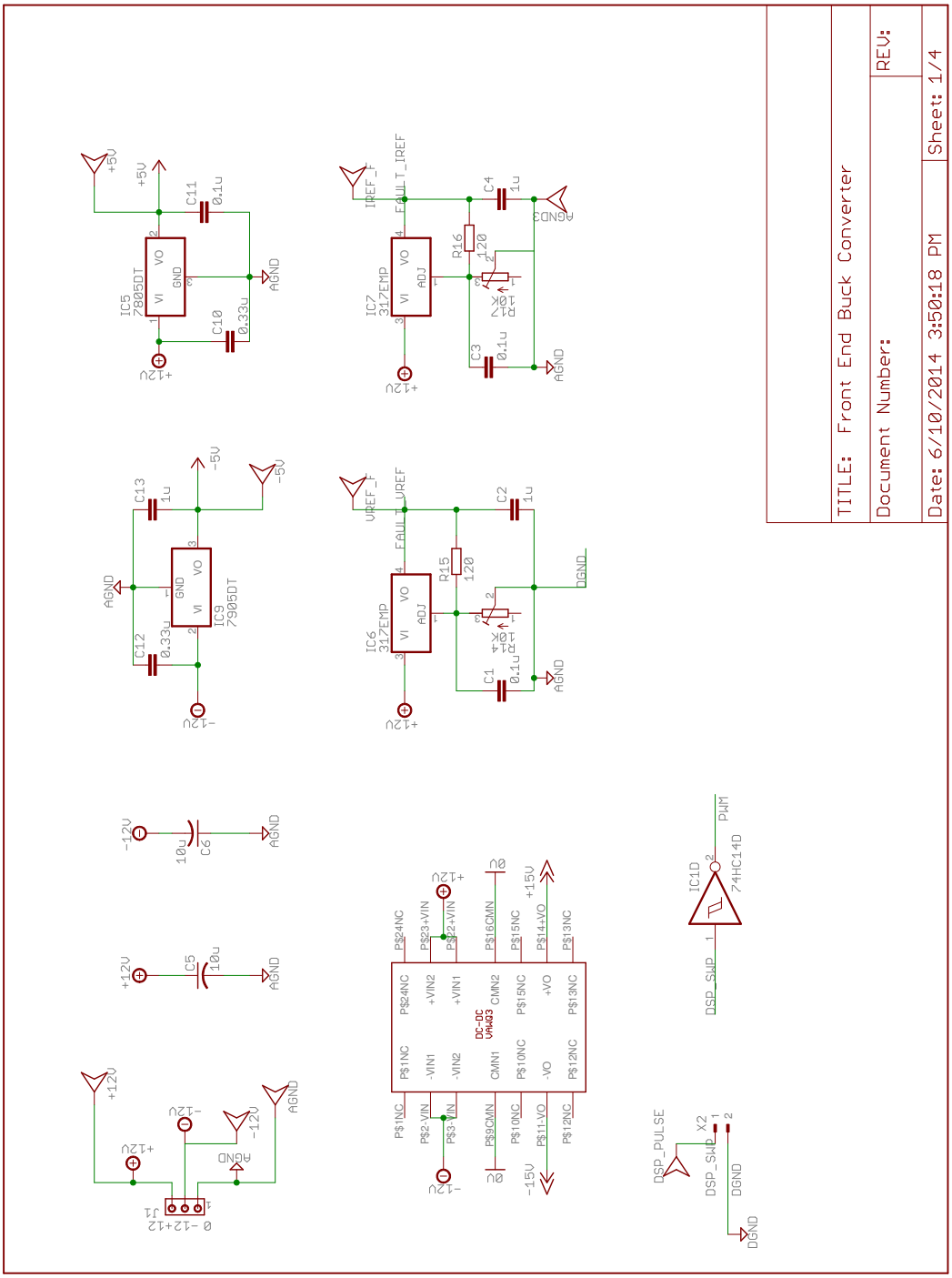

Figure A.6: Schematic of front-end buck converter.

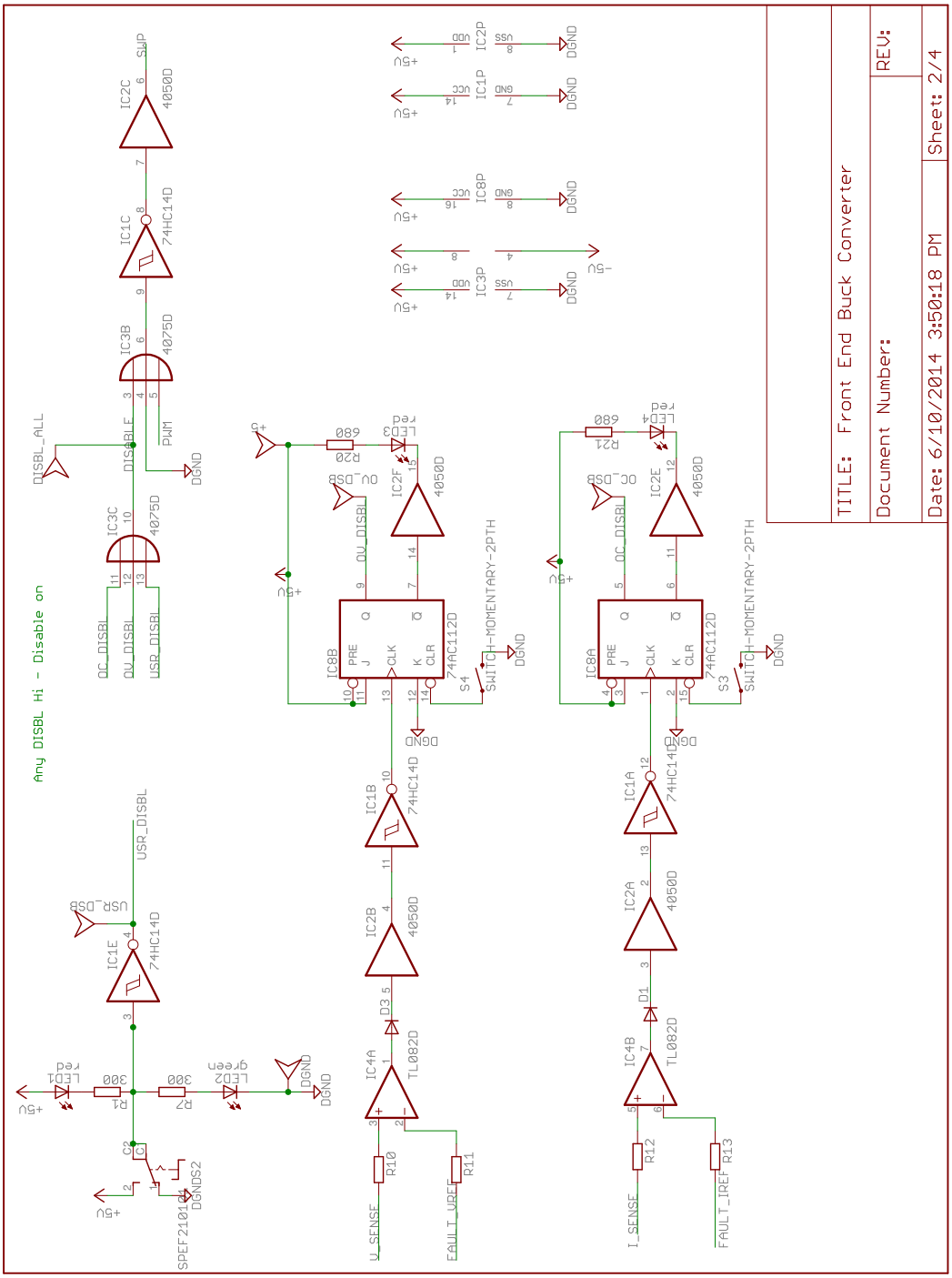

Figure A.7: Schematic of front-end buck converter.

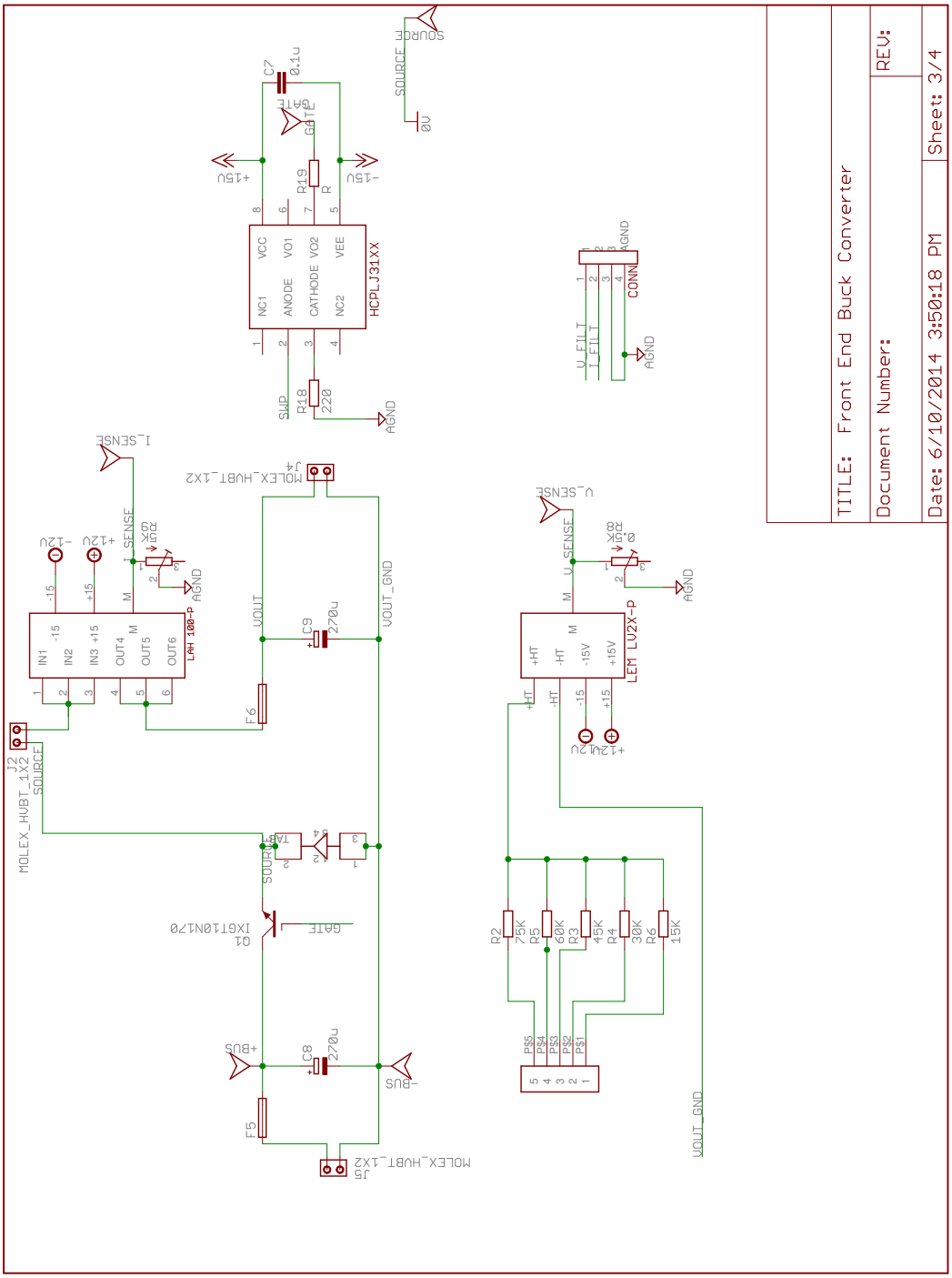

Figure A.8: Schematic of front-end buck converter.

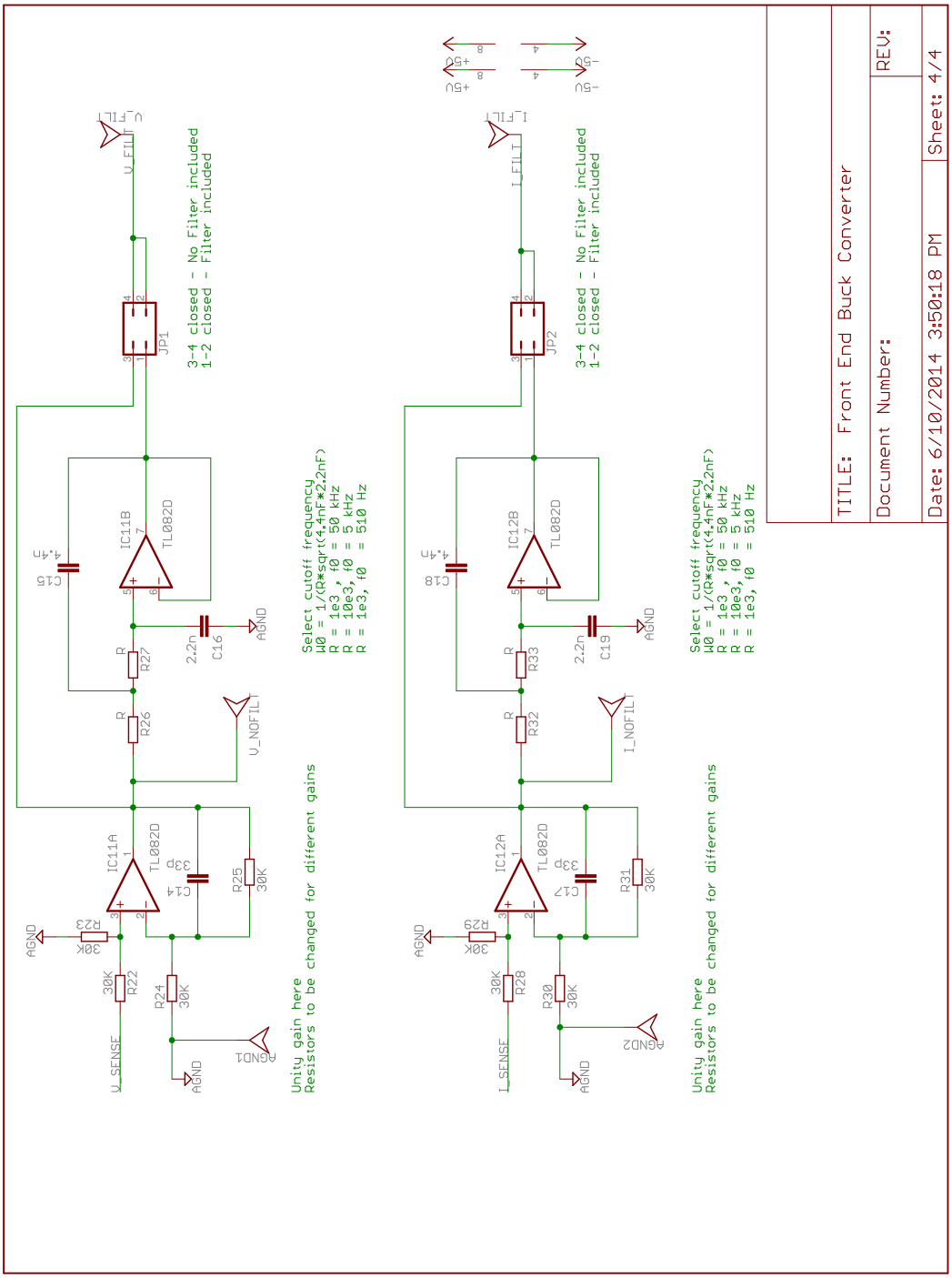

Figure A.9: Schematic of front-end buck converter.

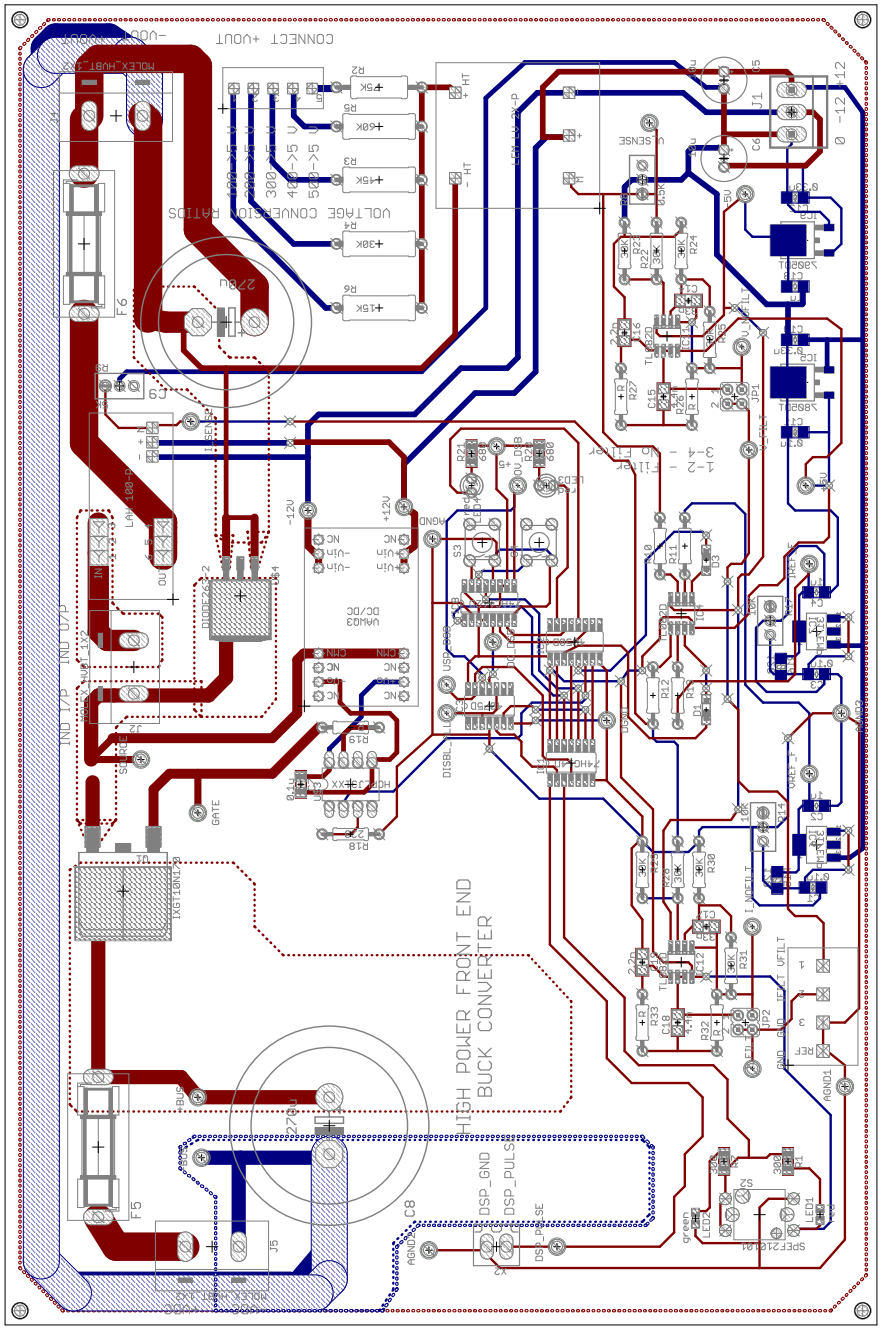

Figure A.10: Printed circuit board layout of front-end buck converter.

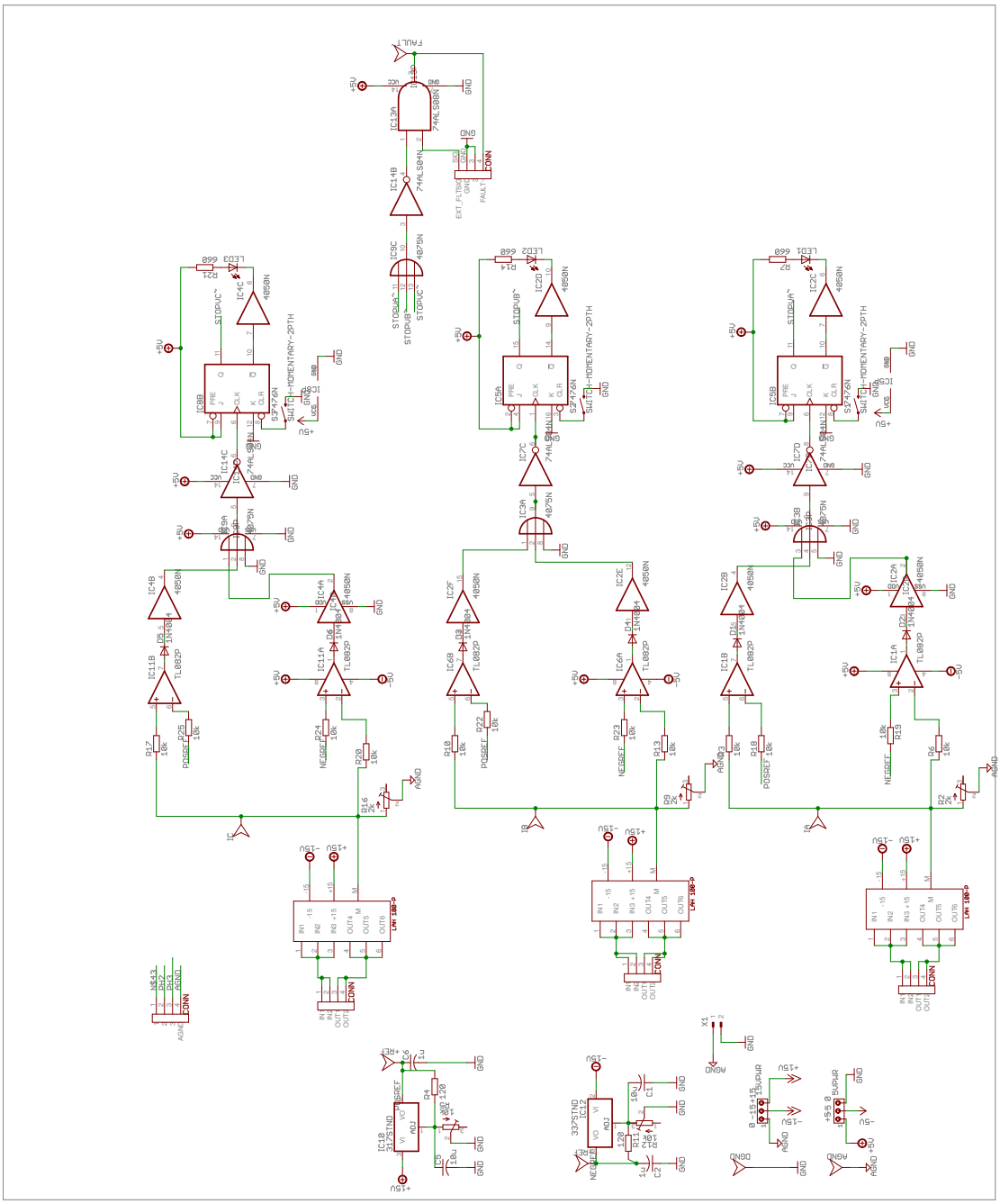

Figure A.11: Schematic of current transducer module for filter.

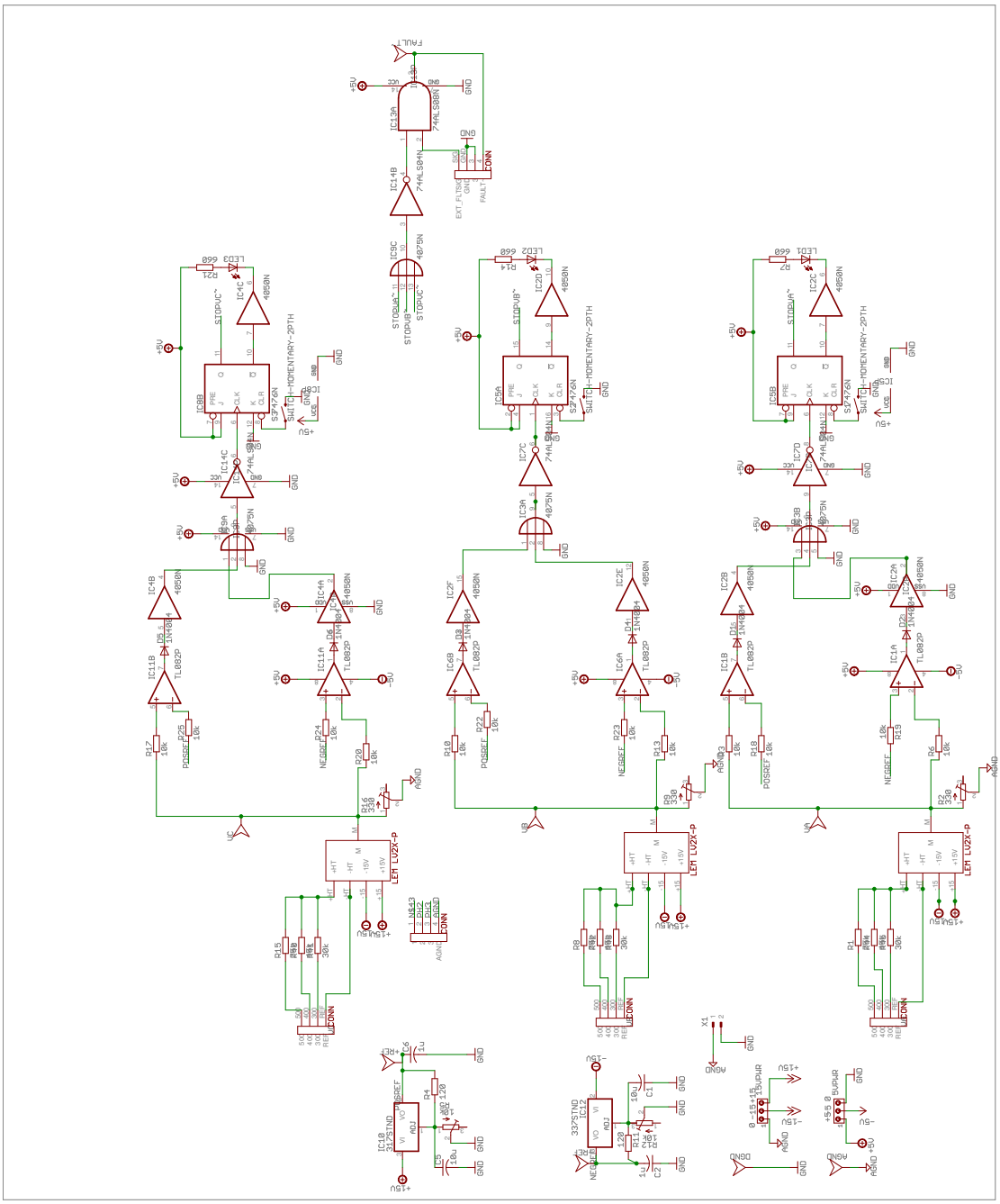

Figure A.12: Schematic of voltage transducer module for filter.

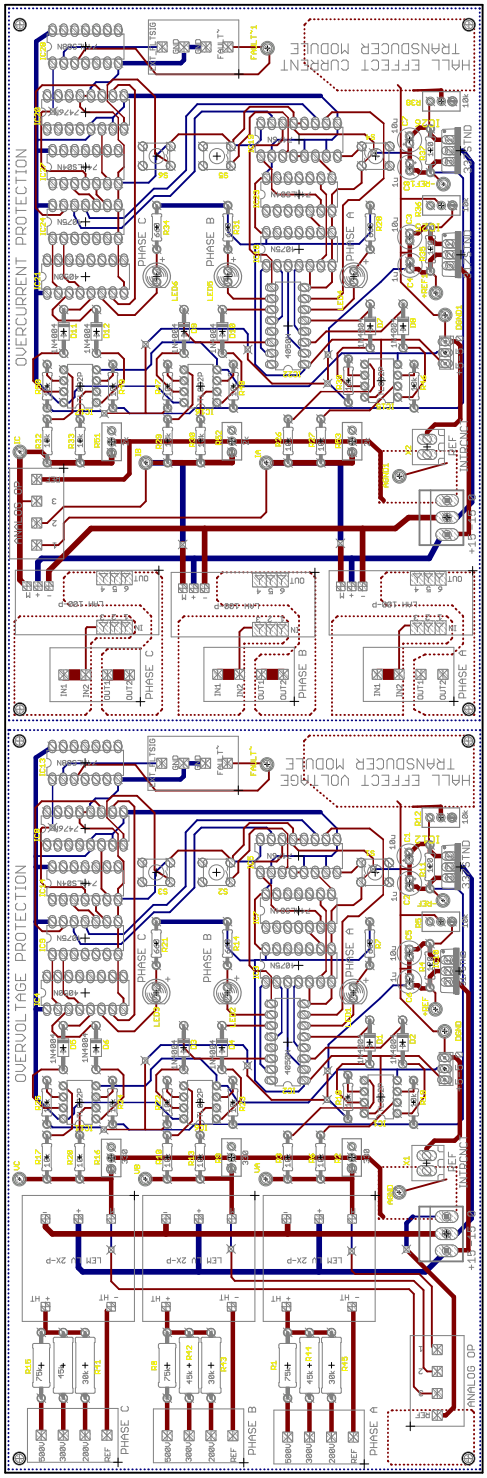

Figure A.13: Printed circuit board layout of voltage and current transducer modules.

BIBLIOGRAPHY

[1] Toyota. (2014) 2014 Toyota North American Environmental Report. [Online]. Available: http://www.toyota.com/usa/environmentreport2014/

[2] P. WaIde and C. U. Brunner. (2011) Energy-efficiency policy opportunities for electric motor-driven systems. International Energy Agency. [Online]. Available: https://www.iea.org/publications/freepublications/publication/EE-or-ElectricSystems.pdf

[3] A. Bazzi and P. T. Krein, "Review of methods for real-time loss minimization in induction machines," *IEEE Trans. Industry Applications*, vol. 46, no. 6, pp. 2319–2328, 2010.

[4] A. M. Bazzi and P. T. Krein, "A survey of real-time power-loss minimizers for induction motors," in *Proc. IEEE Electric Ship Technologies Symposium (ESTS)*, 2009, pp. 98–106.

[5] J. Malinowski, J. McCormick, and K. Dunn, "Advances in construction techniques of AC induction motors: Preparation for super-premium efficiency levels," *IEEE Trans. Industry Applications*, vol. 40, no. 6, pp. 1665–1670, 2004.

[6] J. L. Kirtley, Jr., J. G. Cowie, E. F. Brush, D. T. Peters, and R. Kimmich, "Improving induction motor efficiency with die-cast copper rotor cages," in *Proc. IEEE Power Engineering Society (PES) General Meeting*, 2007.

[7] M. N. Uddin and S. W. Nam, "New online loss-minimization-based control of an induction motor drive," *IEEE Trans. Power Electronics*, vol. 23, no. 2, pp. 926–933, 2008.

[8] A. Emadi, A. Khaligh, C. H. Rivetta, and G. A. Williamson, "Constant power loads and negative impedance instability in automotive systems: Definition, modeling, stability, and control of power electronic converters and motor drives," *IEEE Trans. Vehicular Technology*, vol. 55, no. 4, pp. 1112–1125, 2006.

[9] United States Environmental Protection Agency. (2014) Dynamometer drive schedules. [Online]. Available: http://www.epa.gov/nvfel/testing/dynamometer.htm

[10] Oak Ridge National Laboratory. (2014) Comparison of U.S., European, and Japanese Driving Cycles Attributes. [Online]. Available: cta.ornl.gov/data/

[11] International Council on Clean Transportation. (2009) Passenger Vehicle Greenhouse Gas and Fuel Economy Standards: A Global Update. [Online]. Available: www.theicct.org/passenger-vehicles

[12] A. Emadi, Ed., *Handbook of Automotive Power Electronics and Motor Drives.* CRC Taylor and Francis, 2006.

[13] S. Wall, "Vector control: A practical approach to electric vehicles," in *Proc. IEE Colloquium on Vector Control and Direct Torque Control of Induction Motors*, 1995.

[14] M. Schroedl, D. Hennerbichler, and T. Wolbank, "Induction motor drive for electric vehicles without speed and position sensors," in *Proc. 5th European Conference on Power Electronics and Applications*, 1993, pp. 271–275.

[15] Texas Instruments. (2015) Hybrid and Electric Vehicle Solutions Guide. [Online]. Available: http://www.ti.com/lit/ml/szza058c/szza058c.pdf

[16] K. Mueller and R. Heinrich, "Modern high voltage drive train architecture to accommodate the needs for a variety of components for future automotive applications," in *Proc. Conference on Future Automotive Technology: Focus Electromobility*, March 2013.

[17] D. Bellur and M. Kazimierczuk, "DC-DC converters for electric vehicle applications," in *Proc. Electrical Insulation Conference and Electrical Manufacturing Expo*, 2007, pp. 286–293.

[18] Toyota. (2015) Toyota Innovations Technology file. Toyota Corporation. [Online]. Available: http://www.toyota-global.com/innovation/

[19] C. Whaling. (2012) Electric drive power electronics: An overview. [Online]. Available: http://electricvehicle.ieee.org/2013/12/02/electric-drive-power-electronics-an-overview/

[20] D. Kirschen, D. W. Novotny, and W. Suwanwisoot, "Minimizing induction motor losses by excitation control in variable frequency drives," *IEEE Trans. Industry Applications*, vol. IA-20, no. 5, pp. 1244–1250, 1984.

[21] L. Kioskeridis and N. Margaris, "Loss minimization in induction motor adjustable-speed drives," *IEEE Trans. Industrial Electronics*, vol. 43, no. 1, pp. 226–231, 1996.

[22] E. Poirier, M. Ghribi, and A. Kaddouri, "Loss minimization control of induction motor drives based on genetic algorithms," in *Proc. IEEE International Electric Machines and Drives Conference (IEMDC)*, 2001, pp. 475–478.

[23] P. Nangsue, P. Pillay, and S. Conry, "Evolutionary algorithms for induction motor parameter determination," *IEEE Trans. Energy Conversion*, vol. 14, no. 3, pp. 447–453, 1999.

[24] D. Kirschen, D. W. Novotny, and T. A. Lipo, "On-line efficiency optimization of a variable frequency induction motor drive," *IEEE Trans. Industry Applications*, vol. IA-21, no. 3, pp. 610–616, 1985.

[25] H. G. Kim, S. K. Sul, and M. H. Park, "Optimal efficiency drive of a current source inverter fed induction motor by flux control," *IEEE Trans. Industry Applications*, vol. IA-20, no. 6, pp. 1453–1459, 1984.

[26] G. O. Garcia, J. C. Mendes Luis, R. M. Stephan, and E. H. Watanabe, "An efficient controller for an adjustable speed induction motor drive," *IEEE Trans. Industrial Electronics*, vol. 41, no. 5, pp. 533–539, 1994.

[27] P. Famouri and J. J. Cathey, "Loss minimization control of an induction motor drive," *IEEE Trans. Industry Applications*, vol. 27, no. 1, pp. 32–37, 1991.

[28] M. Malinowski and S. Bernet, "A simple voltage sensorless active damping scheme for three-phase PWM converters with a filter," *IEEE Trans. Industrial Electronics*, vol. 55, no. 4, pp. 1876–1880, 2008.

[29] D. T. Peters, J. Cowie, E. Brush Jr, and S. Midson, "Use of high temperature die materials and hot dies for high pressure die casting pure copper and copper alloys," in *Trans. of the North Amer. Die Casting Assoc. Congress*, 2002.

[30] S. Williamson and C. McClay, "Optimization of the geometry of closed rotor slots for cage induction motors," *IEEE Trans. Industry Applications*, vol. 32, no. 3, pp. 560–568, 1996.

[31] V. Fireteanu, T. Tudorache, and O. Turcanu, "Optimal design of rotor slot geometry of squirrel-cage type induction motors," in *Proc. IEEE International Electric Machines and Drives Conference (IEMDC)*, vol. 1, 2007, pp. 537–542.

[32] C. Chakraborty and Y. Hori, "Fast efficiency optimization techniques for the indirect vector-controlled induction motor drives," *IEEE Trans. Industry Applications*, vol. 39, no. 4, pp. 1070–1076, 2003.

[33] O. Wasynczuk, S. D. Sudhoff, K. A. Corzine, J. L. Tichenor, P. C. Krause, I. G. Hansen, and L. M. Taylor, "A maximum torque per ampere control strategy for induction motor drives," *IEEE Trans. Energy Conversion*, vol. 13, no. 2, pp. 163–169, 1998.

[34] F. Fernandez-Bernal, A. Garcia-Cerrada, and R. Faure, "Model-based loss minimization for DC and AC vector-controlled motors including core saturation," *IEEE Trans. Industry Applications*, vol. 36, no. 3, pp. 755–763, 2000.

[35] S. H. Kim and S. K. Sul, "Maximum torque control of an induction machine in the field weakening region," *IEEE Trans. Industry Applications*, vol. 31, no. 4, pp. 787–794, 1995.

[36] G. Zhang and P. T. Krein, "Torque-angle-oriented control of induction machines," in *Proc. IEEE International Electric Machines and Drives Conference (IEMDC)*, vol. 1, 2007, pp. 407–412.

[37] Y. W. Li, M. Pande, N. R. Zargari, and B. Wu, "DC-link current minimization for high-power current-source motor drives," *IEEE Trans. Power Electronics*, vol. 24, no. 1, pp. 232–240, 2009.

[38] B. Wu, S. B. Dewan, and G. R. Slemon, "PWM-CSI inverter for induction motor drives," *IEEE Trans. Industry Applications*, vol. 28, no. 1, pp. 64–71, 1992.

[39] A. Qiu, Y. W. Li, B. Wu, N. Zargari, and Y. Liu, "High performance current source inverter fed induction motor drive with minimal harmonic distortion," in *Proc. IEEE Power Electronics Specialists Conference (PESC)*, 2007, pp. 79–85.

[40] D. C. Lee, D. H. Kim, and D. W. Chung, "Control of PWM current source converter and inverter system for high performance induction motor drives," in *Proc. IEEE International Conference on Industrial Electronics, Control, and Instrumentation (IECON)*, vol. 2, 1996, pp. 1100–1105.

[41] Y. Suh, J. Steinke, and P. Steimer, "Efficiency comparison of voltage-source and current-source drive systems for medium-voltage applications," *IEEE Trans. Industrial Electronics*, vol. 54, no. 5, pp. 2521–2531, 2007.

[42] N. R. Zargari, G. Joos, and P. D. Ziogas, "Input filter design for PWM current-source rectifiers," *IEEE Trans. Industry Applications*, vol. 30, no. 6, 1994.

[43] T. A. Lipo, *Vector Control and Dynamics of AC Drives*. Oxford University Press, 1996, vol. 41.

[44] S. A. S. Grogan, D. G. Holmes, and B. P. McGrath, "High-performance voltage regulation of current source inverters," *IEEE Trans. Power Electronics*, vol. 26, no. 9, pp. 2439–2448, 2011.

[45] J. R. Espinoza and G. Joós, "A current-source-inverter-fed induction motor drive system with reduced losses," *IEEE Trans. on Industry Applications*, vol. 34, no. 4, pp. 796–805, 1998.

[46] D. Lee, "Design and implementation of three-phase inverters using a TMS320F2812 digital signal processor," 2009. [Online]. Available: http://repositories.lib.utexas.edu/bitstream/handle/2152/ETD-UT-2009-12-498/LEE-THESIS.pdf

[47] J. D. Ma, B. Wu, N. R. Zargari, and S. C. Rizzo, "A space vector modulated CSI-based AC drive for multimotor applications," *IEEE Trans. Power Electronics*, vol. 16, no. 4, pp. 535–544, 2001.

[48] A. Kwasinski, P. T. Krein, and P. L. Chapman, "Time domain comparison of pulse-width modulation schemes," *IEEE Power Electronics Letters*, vol. 1, no. 3, pp. 64–68, 2003.

[49] D. Busse, J. Erdman, R. Kerkman, D. Schlegel, and G. Skibinski, "The effects of PWM voltage source inverters on the mechanical performance of rolling bearings," *IEEE Trans. Industry Applications*, vol. 33, no. 2, pp. 567–576, 1997.

[50] A. Bonnett, "Analysis of the impact of pulse-width modulated inverter voltage waveforms on AC induction motors," *IEEE Trans. Industry Applications*, vol. 32, no. 2, pp. 386–392, 1996.

[51] B. Wu, *High-Power Converters and AC Drives*. Wiley-IEEE Press, 2006.

[52] J. H. Song, K. B. Kim, and M. J. Youn, "Electrical instability of induction motor driven by CSI with output capacitors," in *Proc. Power Conversion Conference*, 1993, pp. 538–543.

[53] Y. Neba, "A simple method for suppression of resonance oscillation in PWM current source converter," *IEEE Trans. Power Electronics*, vol. 20, no. 1, pp. 132–139, 2005.

[54] S. Nau and H. Mello, "Acoustic noise in induction motors: Causes and solutions," in *Proc. IEEE Industry Applications Society Annual Petroleum and Chemical Industry Conference*, 2000, pp. 253–263.

[55] Y. W. Li, "Control and resonance damping of voltage-source and current-source converters with filters," *IEEE Trans. Industrial Electronics*, vol. 56, no. 5, pp. 1511–1521, 2009.

[56] J. C. Wiseman and B. Wu, "Active damping control of a high-power PWM current-source rectifier for line-current THD reduction," *IEEE Trans. Industrial Electronics*, vol. 52, no. 3, pp. 758–764, 2005.

[57] P. Channegowda and V. John, "Filter optimization for grid interactive voltage source inverters," *IEEE Trans. Industrial Electronics*, vol. 57, no. 12, pp. 4106–4114, 2010.

[58] P. C. Loh and D. G. Holmes, "Analysis of multiloop control strategies for LC/CL/LCL-filtered voltage-source and current-source inverters," *IEEE Trans. Industry Applications*, vol. 41, no. 2, pp. 644–654, 2005.

[59] M. Salo and H. Tuusa, "A vector controlled current-source PWM rectifier with a novel current damping method," *IEEE Trans. Power Electronics*, vol. 15, no. 3, pp. 464–470, 2000.

[60] H. J. Lee, S. Jung, and S. K. Sul, "A current controller design for current source inverter-fed AC machine drive system," *IEEE Trans. Power Electronics*, vol. 28, no. 3, pp. 1366–1381, 2013.

[61] F. Liu, B. Wu, N. R. Zargari, and M. Pande, "An active damping method using inductor-current feedback control for high-power PWM current-source rectifier," *IEEE Trans. Power Electronics*, vol. 26, no. 9, pp. 2580–2587, 2011.

[62] Y. Lei, Z. Zhao, F. He, S. Lu, and L. Yin, "An improved virtual resistance damping method for grid-connected inverters with LCL filters," in *Proc. IEEE Energy Conversion Congress and Exposition (ECCE)*, 2011, pp. 3816–3822.

[63] R. Maheshwari, S. Munk-Nielsen, and K. Lu, "An active damping technique for small DC-link capacitor based drive system," *IEEE Trans. Industrial Informatics*, vol. 9, no. 2, pp. 848–858, 2013.

[64] P. Magne, B. Nahid-Mobarakeh, and S. Pierfederici, "DC-link voltage large signal stabilization and transient control using a virtual capacitor," in *Proc. IEEE Industry Applications Society Annual Meeting (IAS)*, 2010.

[65] V. Blasko and V. Kaura, "A novel control to actively damp resonance in input LC filter of a three-phase voltage source converter," *IEEE Trans. Industry Applications*, vol. 33, no. 2, pp. 542–550, 1997.

[66] S. Mukherjee and G. Poddar, "Fast control of filter for sensorless vector control SQIM drive with sinusoidal motor voltage," *IEEE Trans. Industrial Electronics*, vol. 54, no. 5, pp. 2435–2442, 2007.

[67] J. Salomaki, M. Hinkkanen, and J. Luomi, "Sensorless control of induction motor drives equipped with inverter output filter," *IEEE Trans. Industrial Electronics*, vol. 53, no. 4, pp. 1188–1197, 2006.

[68] A. Sapin, P. Steimer, and J. Simond, "Modeling, simulation, and test of a three-level voltage-source inverter with output LC filter and direct torque control," *IEEE Trans. Industry Applications*, vol. 43, no. 2, pp. 469–475, 2007.

[69] K. Hatua, A. K. Jain, D. Banerjee, and V. T. Ranganathan, "Active damping of output filter resonance for vector-controlled VSI-fed AC motor drives," *IEEE Trans. Industrial Electronics*, vol. 59, no. 1, pp. 334–342, 2012.

[70] D. M. Brod and D. W. Novotny, "Current control of VSI-PWM inverters," *IEEE Trans. Industry Applications*, vol. IA-21, no. 3, pp. 562–570, 1985.

[71] M. P. Kazmierkowski and L. Malesani, "Current control techniques for three-phase voltage-source PWM converters: A survey," *IEEE Trans. Industrial Electronics*, vol. 45, no. 5, pp. 691–703, 1998.

[72] S. Buso, L. Malesani, and P. Mattavelli, "Comparison of current control techniques for active filter applications," *IEEE Trans. Industrial Electronics*, vol. 45, no. 5, pp. 722–729, 1998.

[73] Y. A. Kwon and S. K. Kim, "A high-performance strategy for sensorless induction motor drive using variable link voltage," *IEEE Trans. Power Electronics*, vol. 22, no. 1, pp. 329–332, 2007.

[74] R. Bonert and F. X. Wang, "Self controlled induction motor drive with variable DC link voltage," in *Conference Record IEEE Industry Applications Society Annual Meeting*, 1993, pp. 651–654.

[75] J. R. Wells, P. L. Chapman, and P. T. Krein, "Applications of ripple correlation control of electric machinery," in *Proc. IEEE International Electric Machines and Drives Conference (IEMDC)*, vol. 3, 2003, pp. 1498–1503.

[76] S. Tenner, S. Gunther, and W. Hofmann, "Loss minimization of electric drive systems using a DC/DC converter and an optimized battery voltage in automotive applications," in *Proc. IEEE Vehicle Power and Propulsion Conference (VPPC)*, 2011.

[77] D. Pohlenz and J. Bocker, "Efficiency improvement of an IPMSM using maximum efficiency operating strategy," in *Proc. 14th International Power Electronics and Motion Control Conference (EPE/PEMC)*, 2010.

[78] J. Kolar, H. Ertl, and F. C. Zach, "Influence of the modulation method on the conduction and switching losses of a PWM converter system," *IEEE Trans. Industry Applications*, vol. 27, no. 6, pp. 1063–1075, 1991.

[79] T. M. Undeland and N. Mohan, "Overmodulation and loss considerations in high-frequency modulated transistorized induction motor drives," *IEEE Trans. Power Electronics*, vol. 3, no. 4, pp. 447–452, 1988.

[80] T. Schoenen, A. Krings, D. van Treek, and R. De Doncker, "Maximum DC-link voltage utilization for optimal operation of IPmsm," in *Proc. IEEE International Electric Machines and Drives Conference (IEMDC)*, 2009, pp. 1547–1550.

[81] K. Yamazaki and Y. Seto, "Iron loss analysis of interior permanent-magnet synchronous motors - Variation of main loss factors due to driving condition," *IEEE Trans. Industry Applications*, vol. 42, no. 4, pp. 1045–1052, 2006.

[82] T. Schoenen, M. Kunter, M. Hennen, and R. De Doncker, "Advantages of a variable DC-link voltage by using a DC-DC converter in hybrid-electric vehicles," in *Proc. IEEE Vehicle Power and Propulsion Conference (VPPC)*, 2010, pp. 1–5.

[83] P. Krause, O. Wasynczuk, and S. Sudhoff, *Analysis of Electric Machinery and Drive Systems*. Wiley-IEEE Press, 2002.

[84] S. Sridharan and Krein, "A transfer function approach to active damping of an induction motor drive with LC filters," in *Proc. IEEE International Electric Machines and Drives Conference (IEMDC)*, 2015.

[85] P. T. Krein, *Elements of Power Electronics*. Oxford University Press, 2010.

[86] S. Sridharan and P. T. Krein, "Induction motor drive design for traction application based on drive-cycle energy minimization," in *Proc. Annual IEEE Applied Power Electronics Conference and Exposition (APEC)*, 2014, pp. 1517–1521.

[87] F. Blaschke, "The principle of field orientation as applied to the new transvektor closed-loop control system for rotating-field machines," *Siemens Rev.*, vol. 39, pp. 217–220, 1972.

[88] J. W. Choi, D. W. Chung, and S. K. Sul, "Implementation of field oriented induction machine considering iron losses," in *Proc. Annual IEEE Applied Power Electronics Conference and Exposition (APEC)*, vol. 1, 1996, pp. 375–379.

[89] R. W. Erickson and D. Maksimovic, *Fundamentals of Power Electronics*. Kluwer Academic Publishers, 2000.

[90] A. R. Beig and V. T. Ranganathan, "A novel CSI-fed induction motor drive," *IEEE Trans. Power Electronics*, vol. 21, no. 4, pp. 1073–1082, 2006.

[91] A. D. Rajapakse, A. M. Gole, and P. L. Wilson, "Electromagnetic transients simulation models for accurate representation of switching losses and thermal performance in power electronic systems," *IEEE Trans. Power Delivery*, vol. 20, no. 1, pp. 319–327, 2005.

[92] A. M. Bazzi, P. T. Krein, J. W. Kimball, and K. Kepley, "IGBT and diode loss estimation under hysteresis switching," *IEEE Trans. Power Electronics*, vol. 27, no. 3, pp. 1044–1048, 2012.

[93] B. K. Bose, "An adaptive hysteresis-band current control technique of a voltage-fed PWM inverter for machine drive system," *IEEE Trans. Industrial Electronics*, vol. 37, no. 5, pp. 402–408, 1990.

[94] D. Graovac and M. Purschel, "IGBT power losses calculation using the data-sheet parameters," Infineon, Tech. Rep., January 2009.